COMPUTATIONAL AND THEORETICAL STUDY OF WATER AND LIPID DYNAMICS IN BIOMOLECULAR SYSTEMS

A Dissertation

presented to

the Faculty of the Graduate School

at the University of Missouri-Columbia

in Partial Fulfillment

of the Requirements for the Degree

Doctor of Philosophy

by

JHUMA DAS

Dr. Ioan Kosztin, Dissertation Supervisor

DECEMBER 2010

The undersigned, appointed by the dean of the Graduate School, have examined the dissertation entitled

Computational and theoretical study of water and lipid dynamics in biomolecular systems

presented by Jhuma Das,

a candidate for the degree of doctor of philosophy,

and hereby certify that, in their opinion, it is worthy of acceptance.

Professor Ioan Kosztin

Professor Shi Jie Chen

Professor Gabor Forgacs

Professor Paul Miceli

Professor Dong Xu

Acknowledgments

Great mentor makes a difference! I am truly fortunate to have one of the best, Dr. Ioan Kosztin, to be my mentor. I owe my deepest gratitude to him for his guidance, patience and unwavering support. His scientific passion and insights, integrity and intellectual honesty, problem-solving attitude and high performance expectations have helped me to become a better scientist and more importantly, a better person.

I sincerely thank my committee members Dr. Gabor Forgacs, Dr. Paul Miceli, Dr. Shi-Jie Chen and Dr. Dong Xu for their invaluable advice and continuous encouragement.

I am indebted to Dr. Elijah Flenner not only for his significant contributions to this work but also for guiding me in developing an understanding of the subject. My heartfelt thanks to my former colleagues Dr. Lorant Janosi, and Dr. Bogdan Barz for their various contributions to this work.

It is a pleasure to thank Dr. Maikel Rheinstädter for his valuable advice and support. I am grateful to Dr. Dhananjay Bhattacharyya for guiding my first steps in scientific research with enthusiasm and dedication.

I am heartily thankful to Dr. Adrian Neagu, Dr. Francoise Marga, Dr. Melanie Koehler and Jaya Ghosh for their continuous help and support. A special thanks to my professors and fellow graduate students at the Department of Physics and Astronomy at the University of Missouri. Most importantly, my deepest gratitude to my parents, aunt, brothers, sisters, teachers, friends and family for their encouragement and support throughout my career.

Financial support was provided in part by a grant from the National Science Foundation [FIBR-0526854] and Fellowships from the University of Missouri. Computer time was generously provided by the University of Missouri Bioinformatics Consortium.

Table of Contents

List of Tables

List of Figures

List of Abbreviations

APL	area per lipid
DMPC	dimyristoyl-phosphatidyl-choline
DSF	dynamic structure factor
F	forward
GlpF	glycerol uptake facilitator
HGP	harmonic guiding potential
IDSF	incoherent dynamic structure factor
IISF	incoherent intermediate scattering function
INS	inelastic neutron scattering
JE	Jarzynski equality
MD	molecular dynamics
MF	memory function
MFPT	mean first passage time
MSD	mean squared displacement
PBC	periodic boundary conditions
PDB	protein data bank
PME	particle mesh Ewald
PMF	potential of mean force
QENS	quasi-elastic neutron scattering
R	reverse
RC	reaction coordinate

RMSD	root mean square deviation
SF	selectivity filter
SMD	steered molecular dynamics
SSA	stiff-spring approximation
VMD	visual molecular dynamics
WHAM	weighted histogram analysis method

Abstract

This Ph.D. thesis describes three research projects in theoretical and computational biophysics aimed at studying the dynamics of water and lipid molecules in two distinct biomolecular systems. In the first project the energetics and dynamics of water transport through the aquaglyceroporin (GlpF) channel protein is studied by a combination of all-atom molecular dynamics (MD) simulations (both equilibrium and non-equilibrium MD) and stochastic modeling. The MD results are used to determine the potential of mean force and the diffusion coefficient of water molecules crossing the channel. Then, the latter quantities are used to estimate the intrinsic water flux through GlpF, and the corresponding channel permeability. In the second project, by employing a 0.1 micro second long, all-atom MD simulation, the self and correlated dynamics of lipid atoms and molecules in a fully hydrated DMPC lipid bilayer is investigated. The MD simulation results are used to develop a memory function based approach for accurately calculating the lateral self-diffusion coefficient of lipids. In some cases, the proposed memory function method provides a better approach than the currently used ones for determining the lateral diffusion coefficient of lipids in lipid bilayers from the dynamic structure factor measured in inelastic neutron scattering experiments. The purpose of the third project is to investigate the dynamics of water molecules in a hydrated lipid membrane. Using the same MD simulation as in the second project, the anomalous properties of buried and hydration waters (located at the proximity of the fluctuating surface of the lipid membrane) are revealed and contrasted to the properties of bulk water.

1 Introduction

This Ph.D. thesis describes three research projects in theoretical and computational biophysics aimed at studying the dynamics of water and lipid molecules in two distinct biomolecular systems. The scope of the first project (Chp. 2) is to investigate the energetics and dynamics of the transport of water molecules through the aquaglyceroporin (GlpF) channel protein by employing all-atom equilibrium and non-equilibrium molecular dynamics (MD) simulations. In particular, both the potential of mean force (PMF) and the corresponding (position dependent) diffusion coefficient of single file water molecules moving along the axis of the GlpF channel are determined by using a novel PMF calculation method (known as the FR method) [2]. The obtained PMF and diffusion coefficient are used as inputs in an overdamped Brownian particle model for determining: (i) the mean first passage time of a water molecule through the channel, and (ii) the permeability of GlpF for water.

In the second project (Chp. 3), long-time all-atom MD simulations, combined with theoretical modeling, are used to investigate the local and collective dynamics of lipid atoms and molecules in a model lipid bilayer. First, the lateral diffusion of selected lipid atoms and individual lipid molecules is studied in a hydrated dimyristoyl phosphatidylcholine (DMPC) lipid bilayer. From the analysis of a 0.1μs MD trajectory it is shown that the time evolution of the mean square displacement, $\langle \delta r^2(t) \rangle$, of lipid atoms and molecules exhibits three well separated dynamical regions: (i) ballistic, (ii) subdiffusive, and (iii) linear (Fickian) diffusion. Based on this finding, a simple memory function approach is proposed that is capable of determining with good accuracy $\langle \delta r^2(t) \rangle$ over a time range extending all the way from the ballistic ($t \lesssim 10$ fs) to the Fickian diffusion ($t \gtrsim 10$ ns) regimes. Next, a detailed analysis of the effect of the subdiffusive dynamics of lipids on the self-intermediate scattering function and the corresponding incoherent dynamic structure factor measured in neutron scattering experiments is presented. Finally, the correlated dynamics of the lipid tails in the fluid phase of phospholipid bilayer is also studied. It is shown that correlated molecular motion exists between the DMPC lipid tails around their nearest neighbor dis-

tance ($q = 1.42$ Å^{-1}). The displacements of the lipid tails are correlated up to four to six lipid diameters for times ranging from $\sim$1 ps to $\sim$10 ns. The results of this study have been published in two recent papers [3, 4].

The goal of the third project (Chp. 4) is to study the dynamics of water molecules in a hydrated lipid bilayer. The structure and dynamics of hydration water at the surface of biomolecules (e.g., proteins and lipids in biological membranes) are fundamental for their stability and functioning. Due to the interactions at the surface of a solvated biological membrane, the dynamics of the water and membrane molecules are to some degree correlated. In spite of previous efforts reported in the literature, little is known about the time and length scales of these correlations. In this project, we use our 0.1 μs all-atom MD simulation of a fully solvated DMPC lipid bilayer described in Chp.3 to analyze: (i) the dynamics of the water molecules, and (ii) the out of plane motion of the lipid molecules. By using the Voronoi tessellation method we correctly define four dynamically connected water regions, i.e., buried (R-1), hydration (R-2), intermediate (R-3) and bulk (R-4) water regions. Due to their proximity to the polar lipid headgroups, R-1 and R-2 waters have qualitatively different dynamic properties from the R-3 and R-4 waters. We identify and quantify these differences by investigating, through long-time all atom MD simulation, the time evolution of the lateral MSD of waters and the lifetime of the H-bonds between water and lipid molecules. The super-diffusive regime of the buried and hydration water molecules has not been observed before, and appears to be related to the correlated dynamics of the lipid and water molecules in the normal direction to the plane of the membrane. The anomalous super- and sub-diffusive regimes lead to a self intermediate scattering function with compressed- and stretched exponential relaxation, respectively. In principle, these predictions should be testable using neutron scattering experiments.

2 Energetics and dynamics of water transport in the GlpF channel protein

2.1 Introduction

Living cells interact with their extracellular environment through the cell membrane, which acts as a protective layer for preserving the internal integrity of the cell. The cell's metabolism requires highly selective transport of molecules and ions through the membrane, which is accomplished by specific transmembrane proteins. Aquaporins (AQPs) are channel proteins that play a crucial role in maintaining water balance in both uni- and multi-cellular organisms by passively transporting water and certain small molecules across the cell membrane [5]. Hence, understanding the biophysical mechanisms by which AQPs transport water and other small molecules is of physiological importance.

The glycerol uptake facilitator GlpF (or aquaglyceroporin) is a specialized AQP found, e.g., in the plasma membrane of *Escherichia Coli* [5]. The GlpF exists in a tetrameric form in the cell membrane (see Fig. 2.2). Each monomer (see Fig. 2.1.a) is about 25 Å long with six transmembrane α helices and two half membrane-spanning α helices meeting at the center of the channel [5, 6]. These α helices form a right-handed bundle around each channel and diverge outward from the central region to create periplasmic and cytoplasmic vestibules.

Channel proteins form narrow pores across the cell membrane. Only molecules whose size is smaller than the narrowest region (the so-called "selectivity filter") of the pore can cross the channel. However, due to the specific effective electrostatic field inside the channel, even sufficiently small ions or other charged particles may be blocked from crossing the pore. In such cases, the potential of mean force of the charged (or highly polar) particle inside the pore exhibits at least one sufficiently large potential barrier that prevents the particle from permeating the channel. GlpF has two conserved motifs: (i) a selectivity filter at the entrance of the channel, and (ii) an Asn-Pro-Ala (NPA) motif near the center of the channel (see Fig. 2.1.b). The narrow selectivity filter region is ~ 3.5 Å in diameter. Thus, water, glycerol and some long linear polyalcohols can pass through GlpF [7–9]. The NPA

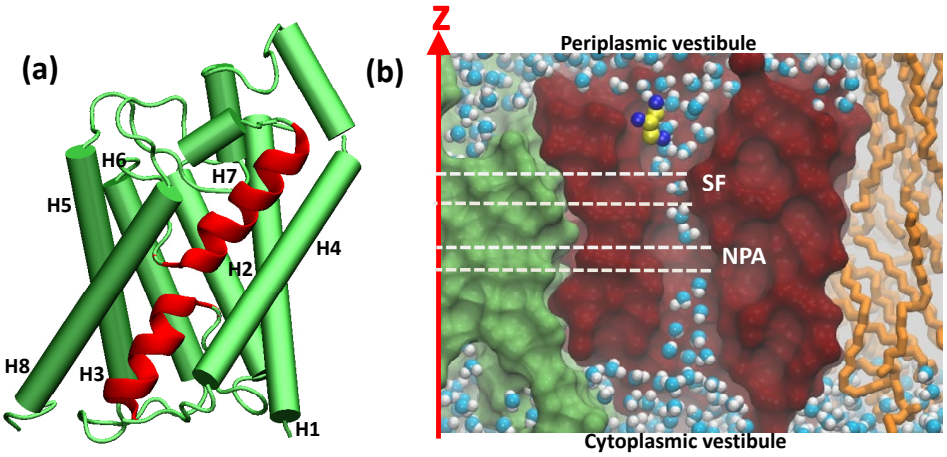

Figure 2.1: (a) GlpF monomer with six transmembrane α helices (H1, H2, H4, H5, H6 and H8, shown in green cartoon representation) and two half membrane-spanning α helices (H3 and H7, shown in red new cartoon representation). (b) Transverse cross-section of a GlpF channel (surface representation of VMD) along with the POPE lipid bilayer and a portion of the adjacent GlpF channel. The water O and H atoms are shown as blue and white spheres, respectively. The selectivity filter (SF) and Asn-Pro-Ala (NPA) motif regions are also shown. All pictures were rendered with the molecular visualization program VMD [1].

motif interrupts the hydrogen bonding network formed by the single file water chain inside the GlpF, thus effectively blocking proton transport [10] through the channel (via the well known Grotthuss mechanism) [11, 12], without affecting the fast water conduction.

The transport properties of water molecules within GlpF is determined by the inner structure of the channel. In general, to study molecular transport through a channel protein one needs to follow the dynamics of the system on a macroscopic time scale while retaining the atomic scale spatial resolution of the system. For example, the GlpF channel is $\sim$ 25 Å long (atomic length scale) but it takes milliseconds (macroscopic timescale) for a glycerol molecule to cross the channel under normal physiological conditions. Currently, even the longest state-of-the-art all-atom MD simulations of systems like GlpF inserted in a completely hydrated lipid bilayer ($\sim 10^5$ atoms) are well below 1 μs. Thus, the study of molecular transport through channel proteins by straightforward MD simulations continues to remain unfeasible.

An alternative approach to this inherently multiscale problem is to model the trans-

ported molecule in the channel as an overdamped Brownian particle that diffuses along the channel in the presence of an effective potential of mean force (PMF) created by the rest of the system [13]. This model requires as inputs the PMF and the diffusion coefficient of the permeated molecule. Having these two quantities, by solving this stochastic model one can determine physical observables, e.g., mean first passage time, osmotic permeability etc., which are important for describing the dynamics of the molecular/ion transport across a channel protein on a macroscopic timescale.

In principle, both the PMF and the diffusion coefficient of the transported molecule can be determined from MD simulations. For a classical mechanical system, the PMF along a chosen reaction coordinate (RC) [13] can be determined from the equilibrium distribution function of the system by integrating out all the degrees of freedom except the RC [14, 15]. However, even for the longest equilibrium MD simulations, this method can only provide the PMF about its local minima [2]. Umbrella sampling, combined with the weighted histogram analysis method (WHAM), is the standard approach used for calculating PMFs from equilibrium MD simulation [14, 16, 17]. However, this approach may become computationally demanding for a feature rich PMF.

An effective alternative for calculating PMFs is to employ fast, non-equilibrium MD simulations. The RC can be sampled efficiently through non-equilibrium *steered molecular dynamics* (SMD) simulations [18], in which the system is guided along the RC by applying an external elastic pulling force. One can determine both the PMF and the corresponding (position dependent) diffusion coefficient by using the FR method [2], which only requires the mean forward (F) and reverse (R) work done by the external pulling force. The mean F and R work of a permeated molecule within the pore can be calculated from a small number of SMD pullings in both the F and R directions along the axis of the channel. This method has been used successfully in several previous cases for studying passive molecule/ion transport through channel proteins and artificial nanopores [2, 19].

In this chapter, first, by employing the FR method, we determine the PMF and the

diffusion coefficient of water molecules moving through a GlpF channel protein. Next, by inserting the determined PMF and diffusion coefficient in the corresponding Langevin equation of motion, we evaluate two physical observables: (i) the mean first passage time and (ii) the osmotic permeability of the water through GlpF.

2.2 PMF and diffusion coefficient of water moelcules in GlpF: Theory

2.2.1 PMF from equilibrium MD simulations

The GlpF channel protein in a fully solvated lipid bilayer can be modeled as a many particle classical mechanical system and can be described by a Hamiltonian $H_0(\Gamma)$. Here, $\Gamma \equiv \{r, p\}$ represents the coordinates and the momenta of all the atoms in the system. For a classical system described by $H_0(\Gamma)$, the PMF (Landau free energy) $U_0(z)$ along a chosen RC (z) is determined from the free equilibrium distribution function of the system by integrating out all the degrees of freedom except z, i.e., [14]

$$e^{-\beta U_0(z)} = w_0(z) = \int d\Gamma \frac{e^{-\beta H_0(\Gamma)}}{Z_0} \delta[z - \tilde{z}(\Gamma)] \tag{2.1a}$$

and

$$U_0(z) = -\log[w_0(z)]. \tag{2.1b}$$

Here, $w_0(z)$ is the equilibrium distribution function of the RC, Z_0 is the partition function, $\beta = 1/k_B T$ is the Boltzmann thermal factor and $\delta(z)$ is the Dirac-delta function, which guarantees that the integrand in Eq. (2.1a) is nonzero only when $\tilde{z}(\Gamma) = z$. Here, z [*or* $z(t)$] is the target value, and $\tilde{z} \equiv \tilde{z}(\Gamma)$ is the actual value of the RC. Throughout this chapter we express the energies in units of $k_B T$, thus, $\beta = 1/k_B T = 1$.

The distribution function $w_0(z)$ of the water molecules in GlpF can be determined from

the equilibrium MD trajectory by binning the z coordinates of the water molecules along the axis of the channel. Then, the PMF can be determined from Eq. (2.1b). While this approach for calculating $U_0(z)$ from a relatively short ($\sim$ 10 ns long) MD trajectory is suitable for water, in general, it provides unreliable PMFs for solute molecules (e.g., glycerol) that pass the channel one at a time. Clearly, this is due to the fact that during the MD simulation at any single time inside the channel one has a significant number ($N_w \approx 10$) of water molecules compared to a single solute (e.g., glycerol) molecule. Thus, determining the PMF corresponding to single molecule transport through a channel protein by using this approach would require prohibitively long MD simulations.

2.2.2 PMF and diffusion coefficient from non-equilibrium SMD simulations using the FR method

The sampling of the RC (i.e., z coordinate) of a transported molecule (e.g., water in our case) through a channel protein can be significantly enhanced by using non-equilibrium SMD simulations [18]. In SMD, a water molecule is guided along the axis of the channel using a harmonic guiding potential (HGP) defined by

$$V_z(\tilde{z}) = \frac{k}{2}[\tilde{z}(\Gamma) - z]^2, \tag{2.2}$$

where k is an elastic constant (spring stiffness). Equation (2.2) defines an elastic force exerted by a fictitious harmonic spring, with zero rest length and stiffness k, on a selected water molecule with z coordinate $\tilde{z}(\Gamma)$. One end of the spring is attached to the pulled water molecule, while the other end with $z = z(t)$ is 'pulled' according to a predefined protocol. In a constant velocity SMD simulation (cv-SMD), $z = z(t) = z_0 + vt$, where v is the constant pulling velocity along the RC, and z_0 is the initial target value of the RC. For a sufficiently large k (referred to as the *stiff-spring approximation* (SSA) [7, 20]), the distance between the target value $z(t)$ and the actual value $\tilde{z}(\Gamma)$ of the RC at a given time can always be kept

below a desired value e.g., ≤ 2 Å [2].

During the SMD simulations, due to the HGP, a given water molecule j experiences an external force equal to F_j

$$\mathbf{F}_j = -\frac{\partial V_z}{\partial \mathbf{r}_j} = -k[\tilde{z}(\Gamma) - z]\frac{\partial \tilde{z}(\Gamma)}{\partial \mathbf{r}_j} \,. \tag{2.3}$$

The total (external) work done on the system to pull the selected water molecule from z_0 to z_1 is given by

$$W_z = \int_{z_0}^{z_1} dz \left[\frac{\partial V_z(\tilde{z})}{\partial z}\right] = k\int_{z_0}^{z_1} dz\,[z - \tilde{z}] \,. \tag{2.4}$$

Note that to every forward (F) path ($0 \rightarrow 1$) it corresponds a time reversed (R) path ($1 \rightarrow 0$). The work for the reverse pulling (i.e., from z_1 to z_0) is given by Eq. (2.4), in which the limits of integration are inverted. Next, the mean value of the forward work $\langle W_F \rangle$ is determined by averaging over the works done during all the pullings in the F direction (i.e., from z_0 to z_1). Similarly, the mean reverse work $\langle W_R \rangle$ is determined by considering all SMD pullings in the R direction (i.e., from z_1 to z_0). Finally, according to the FR method, the change $\Delta U_{01} = U(z_1) - U(z_0)$ in the PMF can be expressed in terms of the mean F and R works, i.e., [2]

$$\Delta U_{01} \equiv U(z_1) - U(z_0) = \frac{\langle W_F \rangle - \langle W_R \rangle}{2}. \tag{2.5}$$

Furthermore, according to the FR method [2], the mean (irreversible) dissipative work during the F and R pullings are equal, i.e., $\langle W_d \rangle = \langle W_d^F \rangle = \langle W_d^R \rangle$, and can be expressed in terms of $\langle W_F \rangle$ and $\langle W_R \rangle$ [2]

$$\langle W_d \rangle = \frac{\langle W_F \rangle + \langle W_R \rangle}{2} \,. \tag{2.6}$$

While strictly speaking the FR method can provide only the PMF difference ΔU_{01}, in practice, by applying Eq.(2.5) to $\langle W_F(z) \rangle$ and $\langle W_R(z) \rangle$ for any $z \in (z_0, z_1)$, the obtained $U(z) - U_0$ can be used to estimate the intermediate $U(z)$ as well.

To reconstruct the full PMF in a feature-rich channel, one needs to divide the channel

into a sufficiently large number of sections N using $N+1$ division points $\{z_0, z_1, .., z_m, ..., z_N\}$. Using Eq. (2.5), one can determine $U(z) - U_{i-1}$, with i = 1,...,N, for all intermediate $z \in (z_{i-1}, z_i)$ recorded in the SMD pullings. Then, by stitching together $U(z)$ for all N segments on can easily reconstruct the PMF for the entire channel up to the additive constant $U_0 = U(z_0)$. Similarly, using Eq. (2.6), one can also determine $\langle W_d(z) \rangle$ for each individual segment, and for the entire channel as well.

Since $\langle W_d(z) \rangle$ is proportional to the pulling speed v [2], the position-dependent friction coefficient, $\gamma(z)$, can be found readily from the slope of the mean dissipative work, i.e., $\gamma(z) = (d\langle W_d(z) \rangle / dz) / v$. Finally, the position-dependent diffusion coefficient, $D(z)$ is given by the Einstein relation (in $k_B T$ energy units) [2]

$$D(z) = \gamma(z)^{-1} = v\,(d\langle W_d(z) \rangle / dz)^{-1} \ . \tag{2.7}$$

2.3 Computer modeling of water transport through the GlpF channel protein

2.3.1 Building the system

A GlpF tetramer (Fig. 2.2) was built from the high resolution ($\sim$2.2 Å) X-Ray crystal structure of glycerol-bound GlpF monomer (PDBID 1FX8 [5]). First, the glycerol molecules were removed from the crystal structure of GlpF monomer. Then the missing hydrogens were added to the system using the VMD plugin *psfgen* [1]. The GlpF tetramer was created from the monomer by applying three consecutive 90° rotations around a properly chosen axis parallel to the axis of the channel (z-axis). The magnesium (Mg) atom located at the center of the central pore (determined by the four monomeric units) was kept fixed during all MD simulations. The system was energy minimized for 30,000 steps. Then, the tetramer was inserted into a pre-equilibrated patch of fully hydrated POPE (16:0/18:1c9-

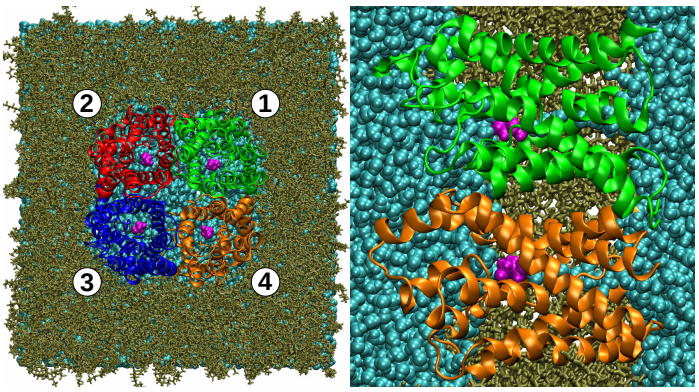

Figure 2.2: Left panel: top view of the fully hydrated GlpF-POPE system. The four GlpF monomers are shown in cartoon representation and are colored in green (1), red (2), blue (3) and orange (4); the glycerol molecules inside the channels are colored in magenta; the POPE lipids are shown in licorice representation; the water is represented as light blue spheres. Right panel: side view of GlpF monomers 1 and 4.

paliotoyloleyl-phosphatidylethanolamine) lipid bilayer. The dimension of the POPE membrane patch, generated with the VMD plugin *membrane* [1], was $(143 \times 135 \times 53)$ Å^3 with an area per lipid (APL) of 74 Å^2. Lipids within 0.55 Å of protein atoms were removed to prevent steric effects. Then, using the VMD plugin *Solvate* [1], the membrane-protein complex was solvated by adding two 8 Å thick water layers on both sides of the lipid bilayer. To neutralize the total electric charge of the system, six chloride ions were added to the solvent using the VMD plugin *Autoionize* [1]. The final system (Fig.2.2) contained 118,278 atoms including 387 lipids and 18,180 water molecules.

2.3.2 Equilibrium MD simulations

The NAMD2.6 parallel MD program [21] was employed to perform the MD simulations. The CHARMM27 [22, 23] force field was used for both proteins and lipids, and the TIP3 model was used for water [24]. A cutoff distance of 12 Å (switching function starting at 10 Å) was assumed for the Van der Waals interactions. Full long-range electrostatic interactions were computed using the Particle Mesh Ewald (PME) method [25] with a grid spacing of 1 Å. Periodic boundary conditions (PBC) were used in all directions to minimize

finite size effects. The simulations were performed in the NpT ensemble with temperature (T = 310 K) and pressure (p = 1 atm) set for physiological conditions. The temperature of the system was kept constant by coupling the system to a Langevin heat bath with a Langevin damping coefficient $\gamma = 5$ ps^{-1}. Constant pressure was maintained using the Nosé-Hoover Langevin piston method [26] with decay time of 200 fs and damping time of 100 fs. The flexible cell option was enabled to keep the ratio of the unit cell in the *xy* plane constant while allowing fluctuations along all axes. All simulations were carried out on 64 CPUs of a dual core 2.8 GHz Intel Xeon EM64T cluster with a performance of $\sim$ 1 day/ns.

First, the built system (see Sec. 2.3.1) was subjected to 30,000 energy minimization steps to eliminate bad Van der Waals contacts. During this relaxation, the GlpF backbone atoms were harmonically restrained to their initial positions using a spring constant k_{bb} = 20 kcal/mol/Å^2 per atom. All P atoms (200 atoms) within the same lipid layer were also restrained harmonically to their initial mean positions along the normal to the plane of the membrane (z axis) by using an effective spring constant k_P = 20 kcal/mol/Å^2 per leaflet. Next, the system was pre-equilibrated in three stages by using the Velocity-Verlet integration method [15] with a time step of 2 fs. The SHAKE algorithm [27] was used for rigid bonds involving all hydrogen atoms. Initially, the system was subjected to gradual heating with a rate of 1 K/ps up to 310 K. In this process, the backbone atoms were restrained with the above k_{bb} and the P atoms of each lipid leaflet were constrained with k_P = 2000 kcal/mol/Å^2. Then the system was equilibrated for another 0.5 ns by releasing the constraints on the P atoms. Finally, a 5 ns free equilibration (simulation E1) was performed with only the Mg atom fixed. Following E1, a 10 ns production run (simulation E2) was performed using multiple time step integration: 1 fs for bonding interaction, 2 fs for non-bonding interactions and 4 fs for electrostatic interactions.

2.3.3 Non-equilibrium SMD simulations

To calculate the PMF $U(z)$ and the corresponding mean dissipative work $\langle W_d(z)\rangle$ for the transported water molecules along the axis of the GlpF channel using the FR method, we employed constant velocity SMD (cv-SMD) pullings in both forward and reverse directions. To this end, we selected four water molecules at the entrance of each GlpF channel (periplasmic end) and restrained them with a stiff spring characterized by an elastic constant $k_z = 25$ kcal/mol/Å^2. We divided the entire channel into ten segments as follows: (1) the narrow pore region, $z \in (-5, 14)$ Å, has been divided into four uneven segments: $(-5,-2)$, $(-2,1)$, $(1,8)$ and $(8,14)$ Å; (2) the periplasmic region was divided into three segments: $(-25,-19)$, $(-19,-10)$ and $(-10,-5)$ Å; (3) the cytoplasmic vestibule was split into three segments: $(14,20)$, $(20,26)$ and $(26,32)$ Å. System configurations with the selected water molecules located in the division points z_i, i = 0, 1, ..., 10 (i.e., z_0 = -25, z_1 = -19, ..., z_{10} = 32, measured in Å) were generated by using a single cv-SMD pulling from the periplasmic end (z_0) to the cytoplasmic end (z_{10}) with a pulling velocity v = 30 Å/ns. The 11 replicas of the system corresponding to these configurations were equilibrated for a period of $\Delta t_{eq} = 1.5$ ns. Next, ten snapshots, evenly separated by 150 ps, from these MD trajectories were used as starting equilibrium configurations for the F and R cv-SMD pullings along the segments $(z_{i-1},\ z_i)$, i = 1, ..., 10.

Since through the confined narrow pore region (z_3, z_7) water transport is single file, the pulled water molecules were not subjected to any restraints in this region. However, outside the pore, on the periplasmic (z_0, z_3) and cytoplasmic (z_7, z_{10}) sides, the pulled water molecules were forced to remain on the z-axis of the channel by applying a harmonic restraint in the perpendicular xy-plane. Furthermore, to minimize the dragging of the whole GlpF channels during the fast cv-SMD pullings, the center of mass of the GlpF backbone atoms (a total of 1071 atoms) was harmonically restrained with $k_{COM} = 500$ kcal/mol/Å^2. The elastic restraining forces on the backbone atoms were applied only along the z-axis

(pulling direction), without altering the flexibility of the pores in the transverse *xy*-plane. In general, the latter may play an important role in the molecular transport properties (also reflected in the profile of the corresponding PMF) of the channel protein.

One expects that for a sufficiently long observation time all four channels in the GlpF tetramer have very similar transport properties. However, their water conduction properties may show noticeable differences during short cv-SMD simulations. Indeed, although the channels are structurally identical, the fluctuations of their atoms' positions are different. Also, because on this time scale lipid molecules are practically frozen as a whole, the conformation of the lipid environment surrounding the individual channels are quite different. Thus, one can increase the reliability of the calculated PMF of water in GlpF by averaging over as many individual GlpF channels as possible. However, before including any of the channels into the averaging process one has to make sure first that these do not present any anomalies of water transport through them (see Sec.2.4.3).

A total of 40 F and R cv-SMD pullings were carried out with a pulling velocity $v =$ 30 Å/ns. Then, the average external works $\langle W_F \rangle$ and $\langle W_R \rangle$ done by the stiff spring were determined. These two quantities were used to calculate the PMF (see Eq. (2.5)) and the mean dissipative work, $\langle W_d \rangle$ (see Eq. (2.6)) along all the segments in each channel.

2.4 PMF and diffusion coefficient of water molecules in GlpF: Results

2.4.1 PMF from equilibrium MD simulations

The equilibrium distribution function, $w_0(z)$, of waters permeated through the GlpF channel was determined from the 10 ns long equilibrium MD simulation (Sec.2.3.2). The water distribution function $w_0(z)$ was calculated by averaging the corresponding distributions for all four GlpF channels. The PMF, $U_0(z)$, was then evaluated using Eq. (2.1b). The results

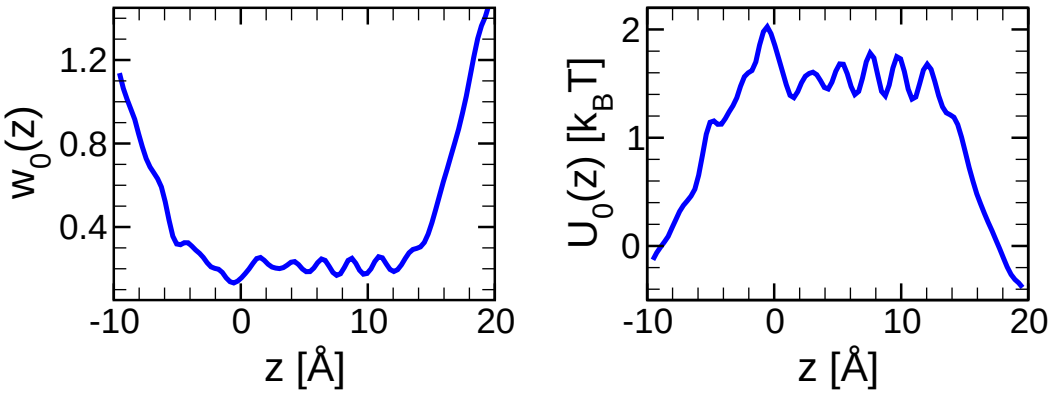

Figure 2.3: The equilibrium distribution function $w_0(z)$ (left panel) and the PMF $U_0(z)$ (right panel) of water inside the GlpF channel (calculated using $w_0(z)$) as a function of z.

for $w_0(z)$ and $U_0(z)$ are shown in the left and right panels of Fig. 2.3, respectively. The PMF $U_0(z)$ has a series of local maxima and minima with the highest barrier ($\sim$ 1.9 k_BT) at the selectivity filter (z = 0). The PMF minima correspond to water binding sites. The small free energy difference $\delta U \lesssim 0.3\, k_BT$ between the cytoplasmic and periplasmic ends is within the error margin with which the PMF can be calculated.

2.4.2 PMF and diffusion coefficient from non-equilibrium SMD simulations using the FR method

By employing the FR method described in Sec. 2.3.3, the PMF $U(z)$ was reconstructed from $4 \times 10 = 40$ F and R constant velocity ($v = 30$ Å^2/ns) SMD pullings of water molecules across the GlpF channels. The top panel of Fig. 2.4, shows 10 F works, $W_F(z)$ through the pore region. Similarly the bottom panel of Fig.2.4 shows the R works (with minus sign) $-W_R(z)$ for the 10 time reversed paths corresponding to the same pore region.

The PMF, $U(z)$, for the water molecules inside the pore region of GlpF channel has been calculated using Eq. (2.5) by averaging over ten F and R works in three of the pores (1, 2 and 4). The resulting PMF is shown as the black curve in Fig. 2.5. The data from channel 3 was not used in our analyses due to the anomalous movement of water through it.

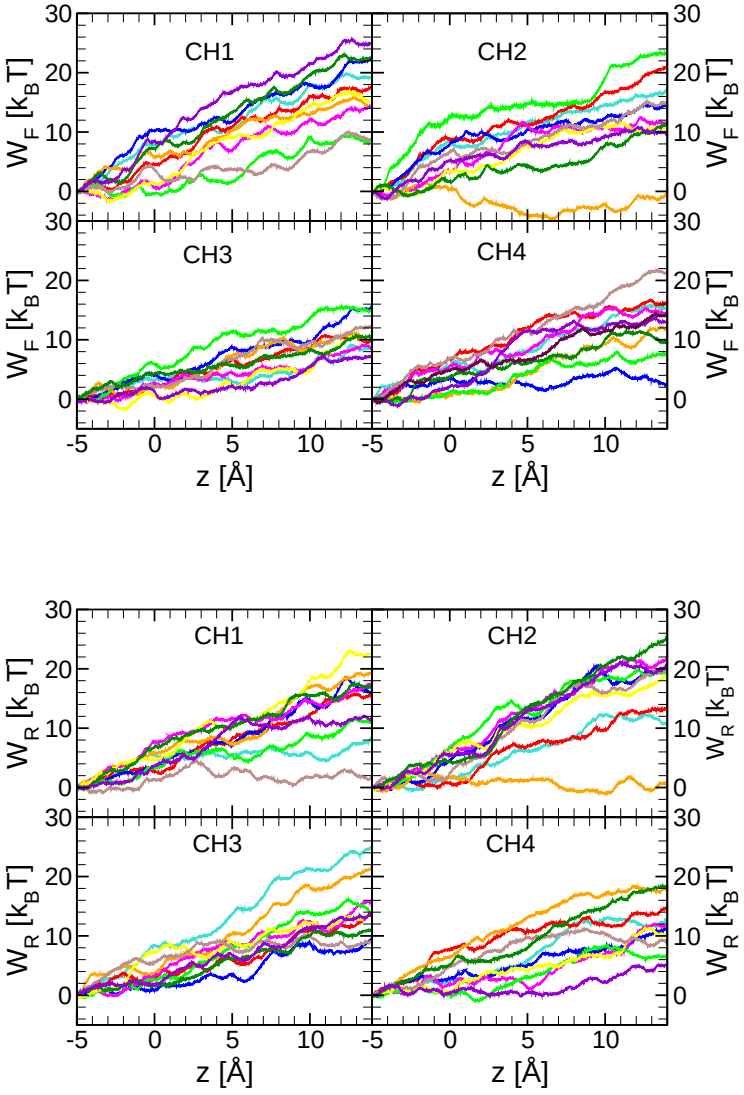

Figure 2.4: (a) Work along forward (top panel) and reverse (bottom panel) SMD pullings for the four GlpF channels (CH1, CH2, CH3 and CH4).

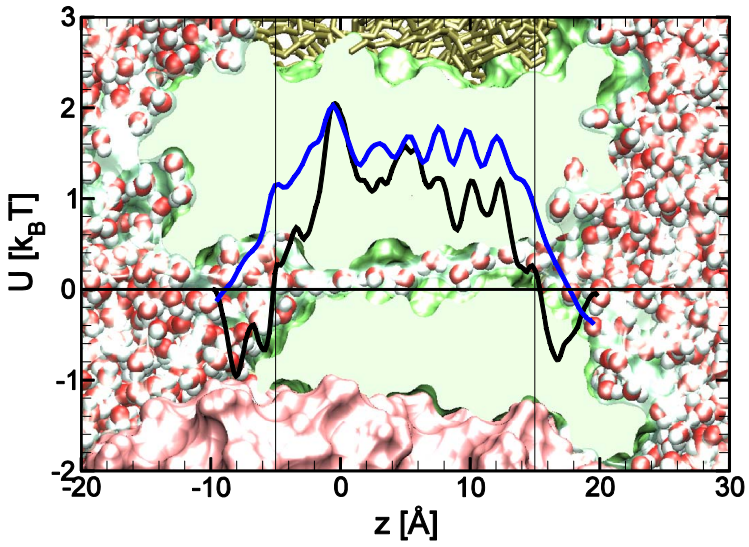

Figure 2.5: PMFs for water in the GlpF channel calculated using: the FR method (black curve), and equilibrium MD simulation (blue curve), respectively. The PMFs are superimposed on the cross section of a GlpF channel.

In particular, unlike for the other three pores (1,2 and 4), water molecules passing the NPA motif in channel 3 did not flip their orientation. Since such a flip is a hallmark of a properly functioning GlpF channel, we concluded that for some reason channel 3 does not conduct water properly when the process is accelerated through cv-SMD simulation. Thus, using the data from this channel would have compromised the form of the PMF of a properly functioning GlpF channel. A detailed analysis of the dynamics of water orientation within the four GlpF channels is presented in Sec. 2.4.3.

In Fig. 2.5 the PMF from the FR method (black curve), $U(z)$, and the one from the equilibrium MD simulation (blue curve), $U_0(z)$, are superimposed on the cross section of the GlpF channel. The PMF barrier at the selectivity filter is of similar size for both PMF. Also, $U(z)$ exhibits most of the binding sites (local minima) in $U_0(z)$ albeit at slightly different locations. In addition, $U(z)$ shows two potential wells corresponding to the periplasmic and cytoplasmic vestibules that are not present in $U_0(z)$. This discrepancy, however, should not come as a surprise. Indeed, the two PMFs are calculated in a rather different way out-

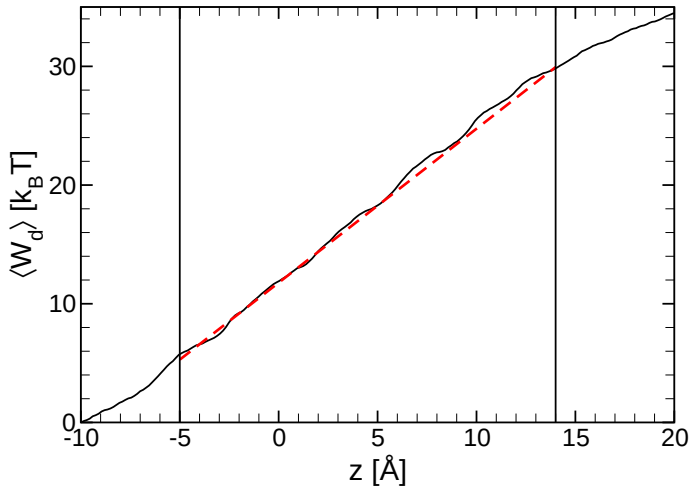

Figure 2.6: Mean dissipative work $\langle W_d \rangle$ of the pulled water molecules.

side the pore region and, therefore, they have different physical meanings. While, $U_0(z)$ is determined from the distribution of all water molecules populating the relatively wide periplasmic and cytoplasmic vestibules, $U(z)$ represents the free energy profile of a water molecule confined to a line parallel to the z-axis of the channel. Since water transport through the pore region is confined to single file, the two PMFs in this region have the same meaning and, therefore, can be compared directly.

Similarly to $U(z)$, we have determined the mean dissipative work $\langle W_d(z) \rangle$ by using Eq. (2.6) and the result is shown in Fig. 2.6. One can see that $\langle W_d \rangle$ increases linearly with z in the pore region, i.e., for $z \in (-5, +14)$ Å. Thus, the corresponding underlying diffusion coefficient of water molecules inside GlpF should be a constant. From Eq. (2.7) one obtains the value of the diffusion coefficient $D \approx 23$ Å^2/ns. This is about an order of magnitude smaller than the bulk diffusion coefficient of water ($D_{bulk} \approx 250$ Å^2/ns). At first sight, contrary to experimental findings, this result would suggest that GlpF is a poor water conductor. Nevertheless, we should remember that water transport in GlpF occurs in a single-file and is highly correlated. At all times, inside each of the four GlpF channels,

there are at least N_w = 9 water molecules present. Hence, it follows that, in fact, the corresponding effective diffusion coefficient of water molecules $D_{\text{eff}} \approx N_w D \sim 9D$ is much larger than the underlying diffusion coefficient D. High D_{eff} implies that GlpF acts as a fast water conducting channel. In Sec. 2.5, we show that D_{eff} is related to the mean first passage time of a water molecule through GlpF and that the calculated value of D_{eff} is indeed rather high, being comparable with D_{bulk}.

2.4.3 Dynamics of water orientation in GlpF

As mentioned in Sec. 2.4.2, the transport of water through one of the four GlpF channels (i.e., channel 3) showed uncharacteristic orientational dynamics during the non-equilibrum SMD pullings. Unlike point particles, water molecules possess dipole moment due to the uneven charge distribution of the constituent atoms: electronegative oxygen and electropositive hydrogen atoms. Due to their dipolar property, water molecules experience electrostatic forces in the presence of a polar environment. Also, under certain conditions, water molecules form hydrogen bonds with other polar molecules, including other water molecules. Dipole interactions and hydrogen bond formations play an important role in regulating the orientational dynamics of water molecules during their passage through GlpF and other channel proteins.

To determine the equilibrium orientation of the water molecules along the narrow pore region of the GlpF channels we have calculated $P_1(z) = \langle \cos(\theta)_z \rangle$, a quantity sometimes referred as order parameter (OP). Here $\langle ... \rangle$ denotes statistical ensemble average, that in case of equilibrium MD simulations can be approximated by time average. The angle θ is defined as the angle formed by the dipole moment of a water molecule with the z-axis of the channel.

The mean orientation $P_1(z)$ of the water molecules inside the four GlpF channels (CH1, CH2, CH3 and CH4) during the 10 ns equilibrium MD simulation is shown in Fig. 2.7.a. The error bars on the plots represent the standard deviation of the OP. On each of the plots

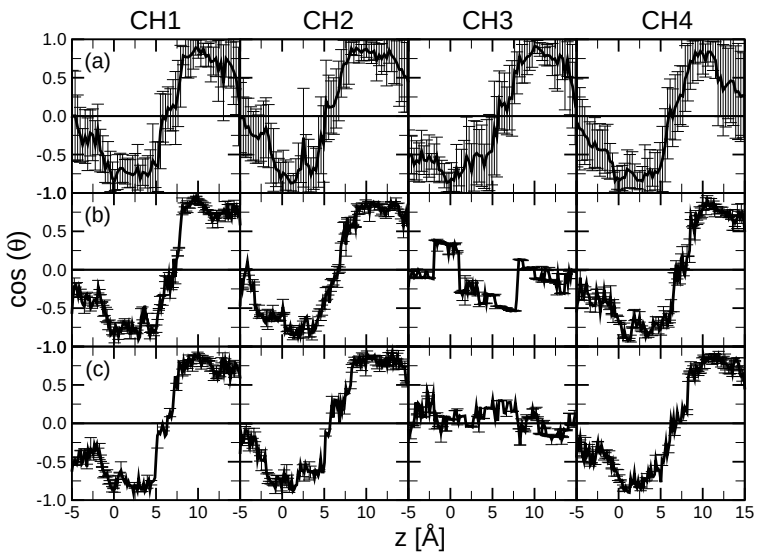

Figure 2.7: Order parameter $P_1(z) = \langle cos\theta(z) \rangle$ calculated for the four channels CH1, CH2, CH3 and CH4 in the case of (a) equilibrium MD simumation E2, (b) F cv-SMD pulls and (c) R cv-SMD pulls. In the equilibrium simulation all channels showed very similar profiles. In case of the SMD pulls (F and R pulls) the water orientation in channel 3 was unusual.

one can distinguish three distinct regions: (i) water molecules enter from the periplasmic side of GlpF with the oxygen atom ahead ($\langle \cos(\theta) \rangle \cong -1.0$), then (ii) at the NPA region the dipole moment of the water molecules flip by an angle $\theta \sim 180^\circ$, and (iii) water molecules exit on the cytoplasmic side with the hydrogen atoms in front ($\langle \cos(\theta) \rangle \cong +1.0$). The waters aligned inside each channel form a water wire by means of hydrogen bonds. Because the water molecules orientation flip at the NPA region of GlpF, the corresponding linear hydrogen bond network is locally disrupted. This mechanism prevents protons and other small ions from crossing through the channel. Thus, the highly conserved NPA motif in all AQPs on one hand allows for rapid water transport in these channels, and on the other hand prevents the membrane potential of being compromised by leaking protons or other small ions. These results are similar to the ones reported in previous equilibrium MD simulations [11, 28].

The OP $P_1(z)$ for the F and R cv-SMD pullings are shown in Fig. 2.7.b and c, respectively. By simple inspection one can see that apart from CH3, the z-dependence of the OP

for all other three GlpF channels has the same characteristic form as in the case of the E2 equilibrium MD simulation (Fig.2.7.a). However, in the case of CH3, $P_1(z)$ appears to be totally different, with none of the hallmark features characteristic to a properly functioning GlpF channel. We do not have an explanation for this discrepancy. In any case, to avoid compromising $U(z)$ and $D(z)$, we have used only the "properly functioning" channels CH1, CH2 and CH4 in our FR method calculations.

2.5 Overdamped Brownian motion of water molecules in GlpF

The calculated $U(z)$ and $D(z)$ can be used as inputs in the Langevin equation describing an overdamped Brownian particle [29]

$$\gamma(z)\dot{z} = -dU(z)/dz + \xi(t) \,, \tag{2.8a}$$

where $\xi(t)$ is the Langevin force (modeled as a Gaussian white noise) and $\gamma(z)$ is the position dependent friction coefficient. The corresponding Fokker-Planck equation (FPE) for the probability distribution function $\rho(z,t)$ of water molecules can be written as

$$\begin{aligned} \partial_t \rho(z,t) &= -\partial_z J(z,t) \\ &= \partial_z[D(z)\partial_z \rho(z,t)] + \partial_z[U'(z)\rho(z,t)] \,, \end{aligned} \tag{2.8b}$$

with $J(z,t)$ the probability current density of a water molecule permeated through the channel. This stochastic model can be used to describe the dynamics of the transported molecule on a macroscopic (or mesoscopic) time scale. Next we apply this model to calculate: (i) the mean first passage time, and (ii) the osmotic permeability of the GlpF channel protein for water molecules.

2.5.1 Mean first passage time

The mean first passage time (MFPT) of a water molecule transported through the GlpF channel can be defined as the average time needed for the diffusing molecule to pass the pore region of the channel from the periplasmic (z_3) to the cytoplasmic (z_7) end. The MFPT of a water molecule diffusing through the GlpF channel can be computed by solving the FPE equation (Eq. (2.8b)). The expression of the MFPT for reflective boundary condition at z_3 and absorbing boundary condition at z_7 is [30]

$$\tau = \int_{z_3}^{z_7} \frac{dz}{D(z)} \int_{z_3}^{z} dz' e^{U(z)-U(z')}. \tag{2.9}$$

The effective diffusion coefficient D_{eff} of the water molecule passing through the GlpF pore of length $L = z_7 - z_3$ = 19 Å can be calculated by using the equation for free diffusion [30]

$$D_{\text{eff}} = \frac{L^2}{2\tau_w}, \tag{2.10}$$

where τ_w is the effective permeation time of a water molecule. With $U(z)$ and $D(z)$ determined in Sec. 2.4.2, one obtains $\tau \approx 9.1$ ns. It is important to note that during this time not only a single water molecule will permeate the channel, but rather a segment of length L of water molecules arranged in a single file, which contains $N_w \approx 9$ water molecules. Thus the effective permeation time for one water molecule is not τ but instead $\tau_w = \tau/N_w \approx 1.01$ ns [31], i.e., on average every ~ 1 ns a water molecule clears (through diffusion) the channel in either direction. A similar value is obtained by directly counting the number of full permeation events of water molecules through GlpF during the 10 ns long equilibrium MD simulation.

Thus, the effective diffusion coefficient of water in GlpF is $D_{\text{eff}} = L^2/2\tau_w \approx 179$ Å^2/ns, which is of the same order of magnitude as $D_{\text{bulk}} \approx 250$ Å^2/ns. This result explains why GlpF (and, in general, AQPs) are so efficient in transporting water across the cell mem-

brane. Our findings are consistent with those reported in previous publications [11, 28, 32–34].

2.5.2 Channel permeability

Using MD simulations, one can determine the PMF, D or MFPT of water molecules transported through AQPs. However, these quantities can not be measured using experiments. The conducting properties of aquaporins (AQPs) are studied experimentally by means of channel permeability p_f, sometimes referred to as osmotic permeability. One can also estimate osmotic permeability by solving the Langevin equation describing an overdamped Brownian particle, once the PMF and the D are obtained from MD simulations. p_f of AQPs has been determined experimentally [35–39] from transmembrane water permeability, P_f, (in the units of cm s^{-1}). To determine the channel permeability p_f reliably from P_f, one needs to measure the number of AQP channels per unit area of the membrane (n/A). But, the precise estimate of n is difficult as it depends on protein to lipid composition of liposomes [37] or other reconstituted systems [35, 36].

For a porous membrane that is permeable for both water and solute, the osmotic permeability of water per pore, p_f, can be expressed in terms of permeability of the membrane, P_f, the membrane area A and the number of pores n as

$$p_f = \frac{P_f A}{n}. \tag{2.11}$$

The channel permeability of water, in the absence of a hydrostatic pressure difference across the membrane, can be expressed as the ratio of the molar flux J_w and the solute concentration difference $\Delta c_s = \Delta n_s / N_A$, i.e.,

$$p_f = -\frac{J_w}{\Delta n_s} \tag{2.12}$$

where Δn_s is the concentration difference expressed in water molecules per unit volume, and N_A is the Avogadro's number. During the steady state transport of molecules across a channel in the absence of hydrostatic pressure difference, the flux J_w across the membrane can be calculated using the PMF, $U(z)$, and the corresponding effective diffusion coefficient D_{eff} [40]

$$J_w = A_0 S_0 (n_1 - n_2), \tag{2.13a}$$

with,

$$A_0 \approx D_{\text{eff}} \cdot e^{U(z_3)} \left[\int_{z_3}^{z_7} e^{U(z)} dz \right]^{-1}. \tag{2.13b}$$

Here, S_0 is the area of the cross-section of the channel at its two ends and n_1, n_2 are the local number concentrations of water molecules at the periplasmic (1) and cytoplasmic (2) sides, respectively.

Comparing Eq. (2.12) and Eq. (2.13a), one can express the channel permeability p_f of GlpF for water transport as

$$p_f = A_0 S_0 \approx D_{\text{eff}} S_0 / \int_{z_3}^{z_7} \exp[U(z) - U(z_3)] dz. \tag{2.14}$$

Using $S_0 \approx 100\text{Å}^2$ along with $U(z)$ and D_{eff} determined with the FR method, one obtains $p_f \approx 10^{-14}\text{cm}^3/\text{s}$. This result is comparable with both the experimentally measured $p_f^{\text{exp}} \approx 5.43 \times 10^{-14}$ cm^3/s in AQP1 [38, 39] (p_f for the water transport through GlpF has not been measured yet experimentally), and the previously reported theoretical values for GlpF, AQPz and AQP1 [12, 31, 41].

2.6 Conclusions

In this chapter we have shown that the FR method can be used successfully to reconstruct the PMF, $U(z)$, of water molecules in the GlpF channel protein, by employing a small number of fast forward and reverse non-equilibrium SMD pullings at constant velocity. The obtained PMF is comparable with the PMF $U_0(z)$ determined from the equilibrium distribution function of water molecules inside the GlpF channel (calculated from equilibrium MD simulations). In the narrowest pore region of GlpF (in which water transport is single file) the PMF shows a series of maxima and minima. The highest barrier is at the selectivity filter, which is also the narrowest region in the GlpF channel. The PMF minima correspond to water binding sites within the pore. At any time, these binding sites accommodate on average 9 water molecules. The PMF determined by the FR method also has two broad potential wells which correspond to the periplasmic and cytoplasmic vestibules.

The underlying water diffusion coefficient, $D(z)$, has also been determined by using the mean dissipative work obtained from the FR method. Within the pore region of GlpF $D(z) \sim 23$ Å^2/ns is constant and is about 10 times smaller than the diffusion coefficient of bulk water.

By using the computed $U(z)$ and $D(z)$ in an overdamped Brownian particle model, we could estimate experimentally measurable properties of water transport in the GlpF channel protein. For example, we obtain $\tau = 9.1$ ns for the mean first passage time of a single-file water molecule (channel occupancy $N_w \approx 9$), $\mathrm{D_{eff}} \approx 179$ Å^2/ns for the effective diffusion coefficient of water in GlpF, and $p_f = 10^{-14}$ cm^3/s for the osmotic permeability. These results are in good agreement with previously published experimental and theoretical results [12, 31, 38, 39, 41], and with the fact that GlpF, like other aquaporins are fast water transporters.

3 Anomalous diffusion of lipid atoms and molecules in phospholipid bilayers

3.1 Introduction

The cell membrane consists of three classes of amphipathic lipids: phospholipids, glycolipids, and cholesterols [42]. It also hosts various kinds of proteins and carbohydrates. Due to their multifaceted biological functions and structural complexity, cellular membranes, have been extensively studied in the literature. Phospholipid bilayers being the fundamental structural elements of biological membranes, are often used as model systems in an attempt to unfold the complex dynamics of cellular membranes.

Phospholipid molecules have a hydrophilic headgroup attached to two hydrophobic hydrocarbon acyl chains (the so-called lipid tails). In the presence of a polar solvent (e.g., water), lipid molecules spontaneously self-assemble into a few nanometer thick phospholipid bilayer with the hydrophilic headgroups facing the polar solvent. The dynamics of lipid atoms and molecules in a phospholipid bilayer span a wide range of time and length scales [43–51]. For instance, the long wavelength undulation and bending modes of the bilayer extend over several hundred lipid molecules in the plane of the membrane with typical relaxation times in the nanosecond range. On the other hand, the short wavelength density fluctuations occur in the picosecond range on nearest neighbor distances of lipid molecules. The motion of the lipids in the lipid bilayer can be classified into two major classes: (i) local motion exhibited by single lipid molecule, and (ii) correlated dynamics due to the concerted motion of several lipid molecules. The atoms within a lipid molecule show vibrational and rotational motion, which occur at femtosecond to nanosecond time scale (fast processes) [47], whereas the lateral diffusion of individual lipids is slower (10 ns to μs).

At room and physiological temperatures most lipid bilayers behave as two dimensional (2D) fluids. The lateral diffusion of lipid molecules in the L_α fluid phase of a lipid bilayer has been extensively studied both experimentally [45–47, 52–57] and by computer simulations [58–66]. Experimental results suggest that the lateral diffusion of lipid molecules

is characterized by at least two distinct diffusion coefficients D_1 and D_2, corresponding to two different time scales, i.e., picosecond and nanosecond, respectively. Researchers have developed several models to explain the difference between D_1 and D_2 [58, 59, 67]. For example, Wohlert and Edholm [59] proposed a model to explain their MD simulation results for a DMPC bilayer. According to this model, D_1, the larger of the two diffusion coefficients, is related to the diffusive motion of lipid atoms caged by the polymeric nature of the lipid they belong to. Because on a sub ns time scale the root mean square displacement (RMSD) of the lipids is less than the mean lipid separation, lipid atoms are forced to move within the confined region (cage) occupied by the host lipid molecule. On the other hand, the smaller diffusion coefficient, D_2 is related to the actual lateral self-diffusion of individual lipids in a given leaflet of the lipid bilayer. Both D_1 and D_2 can be determined from the time dependence of the mean square displacement (MSD) of the lipid atoms or of the CM of individual lipids, provided that the observation time is sufficiently long. The two diffusion coefficients obtained in [59] were in reasonable agreement with existing experimental results.

However, none of these diffusion models provide a satisfactory description of the lateral diffusion of phospholipid molecules as these models ignore the microscopic polymeric structure (characterized by flexibility and connectivity) of lipids. In a simple liquid, atoms move ballistically at short times with the MSD, $\langle[\delta r(t)]^2\rangle \sim t^2$, which is followed by a crossover to linear diffusion with $\langle[\delta r(t)]^2\rangle \sim t^1$. In dense liquids, a caging region is observed between the ballistic and linear regimes, which is characterized by a plateau in $\langle[\delta r(t)]^2\rangle$. However, in a lipid bilayer the dynamics of lipid atoms and molecules are far more complex because of its polymeric structure which is not present in ordinary liquids. So, we expect that the MSD of lipid atoms and molecules should exhibit a pronounced subdiffusive regime in between the ballistic and linear diffusion regimes, where $\langle[\delta r(t)]^2\rangle \sim t^\beta$ with $\beta < 1.0$ [68–70].

In addition to self dynamics, lipids in phospholipid bilayers (in the fluid phase) ex-

hibit in-pane collective molecular motion as they interact locally with their neighboring molecules. The concerted dynamics of lipid molecules is characterized by both spatial and temporal correlations. Estimating the sizes of these correlations is a challenging endeavor. The collective motions in phospholipid model membranes have been studied by employing experimental and computational methods [49, 71–73]. These studies were motivated by the possible impact of the collective dynamics of lipids on the physiological and biological functions of the bilayers, such as transport processes [74], and the functioning of membrane-embedded proteins.

This chapter presents a detailed computational study of the complex dynamics of lipid atoms and molecules in the fluid phase of a model DMPC lipid bilayer. The self diffusion coefficient of individual lipid atoms and molecules are determined by means of long-time (0.1μs), all-atom MD simulation and theoretical modeling. We have also examined the correlated dynamics of lipid molecules and estimate the corresponding correlation length and correlation time. The content of this chapter is based on two recent publications [3, 4].

3.2 Computer modeling and MD simulation of DMPC bilayer

To investigate the dynamics of lipid atoms and molecules of a phospholipid membrane, we performed a 0.1 μs long all atom MD simulation of a fully solvated DMPC lipid bilayer (Fig. 3.1). The pre-equilibrated structure of the bilayer was obtained from Mikko Karttunen's web site (www.apmaths.uwo.ca/$\sim$mkarttu/downloads.shtml) [75] and contained 128 lipid molecules. The system was solvated by adding two 12 Å thick layers of water to each side of the membrane using the *Solvate* plugin in VMD [1]. The final system contained a total of 2577 TIP3 water molecules [24].

The MD simulation was performed with NAMD-2.6 [21] using the CHARMM27 [23] force field for DMPC lipids. The equations of motion were integrated with a multiple time

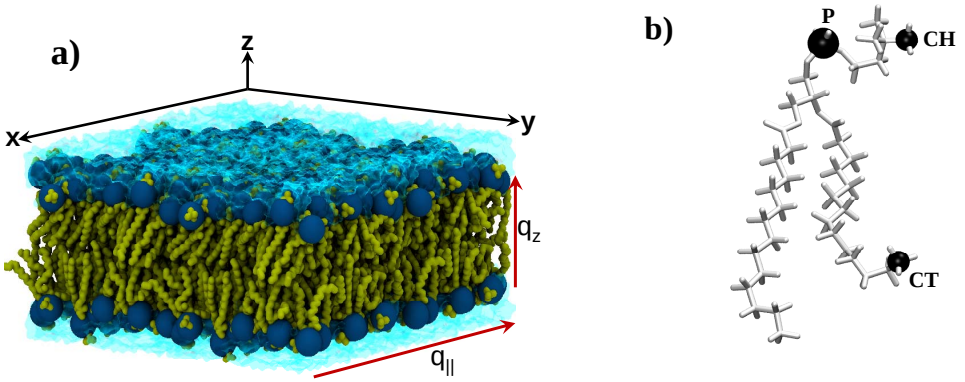

Figure 3.1: a) The simulated DMPC lipid bilayer system. b) a DMPC lipid molecule. The atoms whose dynamics is investigated in this work (P, CH and CT) are highlighted as black spheres. Figures created using VMD [1].

step algorithm with time steps of 1 fs for bonding interactions, 2 fs for non-bonding interactions, and 4 fs for long-range electrostatic interactions. The non-bonded interactions were cut-off at 12 Å with a smooth switching function starting at 10 Å. Long-range electrostatic interactions were computed by employing the smooth Particle Mesh Ewald (PME) method [76] with a grid spacing of 1 Å. To reduce finite size effects the MD simulation was carried out with periodic boundary conditions (PBC).

In order to study the fluid phase of a DMPC lipid bilayer [77], the system was brought to $T = 303$ K and normal pressure ($p = 1$ atm) through several stages of equilibration. First, the system was subjected to 6×10^4 energy minimization steps by harmonically restraining the phosphorous (P) atoms of the lipid headgroups along the normal to the surface of the membrane. Then, by coupling it to a heat bath, the system was gradually heated to the desired temperature $T = 303$ K at a rate of 1 K/ps. After removing all the restraints, the system was equilibrated through a 75 ns long NpT simulation. At the end of this process the area per lipid (APL) was 56.2 Å^2. Then, the APL was increased to the desired value of ~ 60 Å^2 by gradually increasing the size of the system in the *xy*-plane of the membrane. The final system size was $62 \times 62 \times 58.5$ Å^3, with an APL of 60.06 Å^2. The equilibration process was concluded with an additional 10 ns MD simulation keeping both temperature

and volume constant (NVT ensemble). Finally, a production run of 0.1μs was performed in the NVT ensemble. The temperature was kept constant by coupling the system to a Langevin thermostat with a coupling constant of 0.05 ps^{-1}. The coordinates of all the atoms were saved every 2 fs for the first 100 ps, every 20 fs for the next 10 ns, and every 100 fs for the next 90 ns. The recorded data was used to study the short, intermediate, and long time dynamics of the lipid atoms and molecules.

The MD simulations were carried out on 40 CPUs of a dual core 2.8GHz Intel Xeon EM64T cluster with a performance of around 0.2 days/ns.

3.3 Mean square displacement of lipid atoms and molecules

In this section, we examine the time dependence of the lateral mean square displacement (MSD) of selected atoms within the lipid and of the entire lipid molecules in the lipid bilayer. The lateral MSD of any atom a can be written as

$$\langle [\delta r^a(t)]^2 \rangle = \langle [\vec{r}^a(t) - \vec{r}^a(0)]^2 \rangle, \tag{3.1}$$

where $\vec{r}^a(t)$ is the projection on the plane of the membrane of the actual position vector of atom a at a given time t. To better characterize the time dependence of the MSD, we also calculate the logarithmic derivative of the MSD, $\alpha(t)$, defined as

$$\alpha(t) = \frac{\partial \ln[\langle [\delta r(t)]^2 \rangle]}{\partial \ln(t)}, \tag{3.2}$$

Clearly, in the ballistic regime $\alpha(t) = 2$, in the linear diffusion regime $\alpha(t) = 1$, and in the sub-diffusive regime, characterized by $\langle \delta r(t)^2 \rangle \sim t^\beta$, $\alpha(t) = \beta \approx$ const.

First, we calculate the lateral MSD of the lipid atoms and of the center of mass (CM)

of a lipid molecule by using the MD simulation trajectory. Next, we show that the calculated MSDs can also be reproduced by employing a theoretical model based on the Mori-Zwanzig projection operator method with a properly chosen *memory function* (MF).

3.3.1 Mean square displacement from MD simulation

Here, we focus on the motion of three representative atoms, phosphorus (P), carbon in the headgroup C15 (CH), and carbon in the lipid tail C214 (CT) atoms in the lipids. The positions of these atoms (P, CH and CT) within the lipid molecule are shown in Fig. 3.1, right panel. The time evolution (on a log-log scale) of the lateral MSD of the P (squares), the CH (triangles) and the CT (circles) atoms are shown in Fig. 3.2, top panel. The time evolution of MSD for all three atoms shows an initial ballistic region followed by a small caging region that displays a gradual crossover to a linear diffusion regime via an extended sub-diffusive regime characterized by $\langle[\delta r^a(t)]^2\rangle \sim t^\beta$ with $\beta < 1.0$. The ballistic regime for CH and CT atoms are the same, but starting from the caging region their MSD differ. The MSD of CT is larger compared to CH, indicating that the cage is bigger for CT (and, also, for all the atoms in the tail) than for the atoms in the lipid headgroup. This variation in MSD has been identified before and is a direct consequence of the structure of a lipid bilayer [59, 60].

The MSD is also calculated for: (i) the center of mass (CM) of the lipid (blue curve in Fig. 3.2), and (ii) all the hydrogen (H) atoms in a lipid molecule (Fig. 3.2, red curve). Thus, we have found that for both individual lipid atoms and the entire lipid molecule (described through its CM) the MSD shows three clearly separated dynamical regimes, i.e., ballistic, sub-diffusive and linear diffusive. The crossover to linear diffusion begins around 10 ns and $\langle[\delta r^a(t)]^2\rangle \approx 100$ Å^2, which corresponds to the nearest neighbor distance of lipids ($\sim$10Å).

To better visualize the time dependence of the MSD, we have also evaluated $\alpha(t)$, for the considered representative atoms and the CM of phospholipid molecules (Fig.3.2,

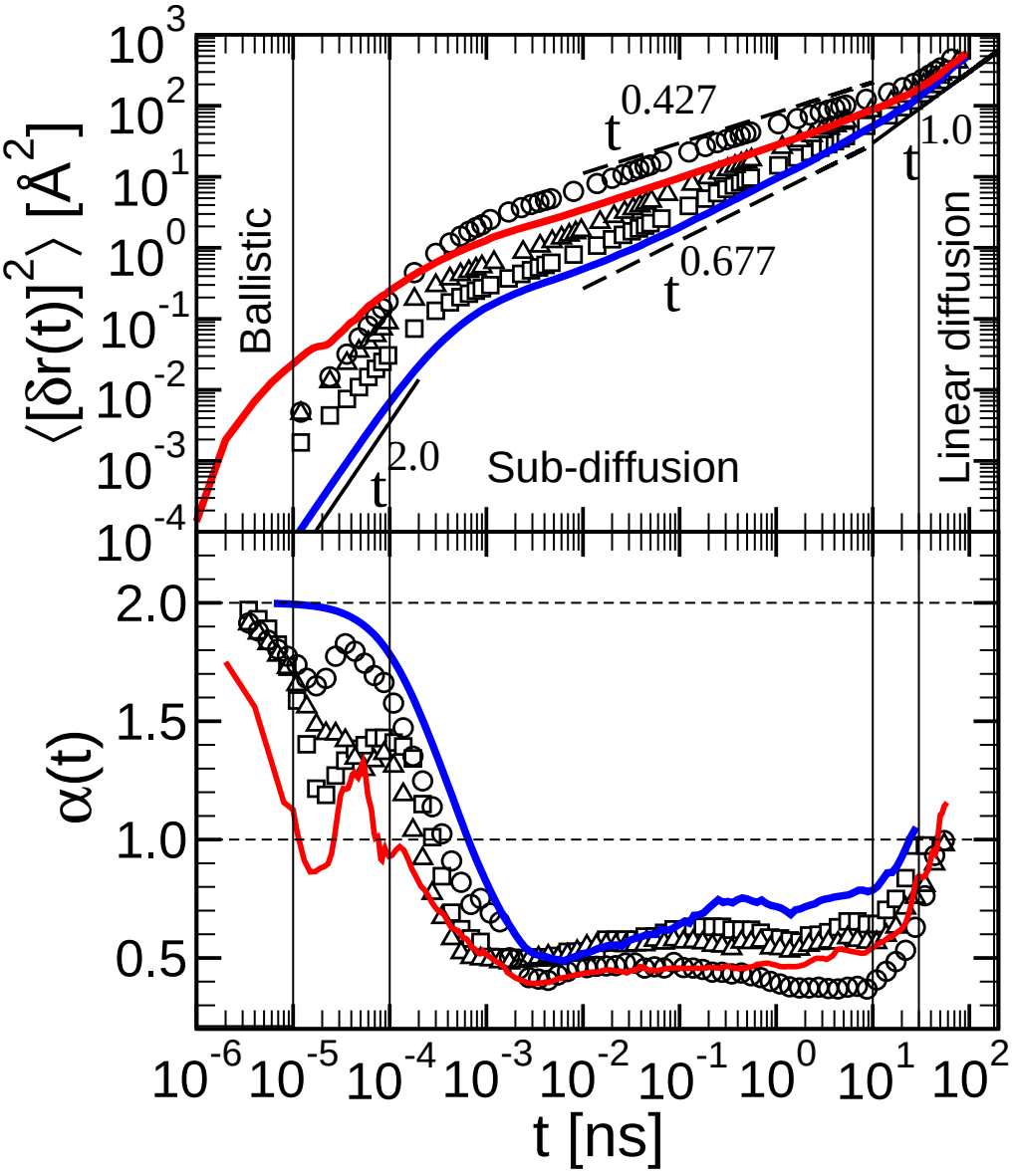

Figure 3.2: Top panel: Lateral mean square displacement of the P (squares), CH (triangles) and CT (circles) atoms, and the CM of the lipids (blue curve) and the hydrogen atoms in the lipid tails (red curve). Bottom panel: $\alpha(t)$ for the P (squares), CH (triangles) and CT (open circles) atoms, and the CM of the lipids (blue curve) and the hydrogen atoms in the lipid tails (red curve). The selected atoms (P, CH and CT) are highlighted in Fig. 3.1.

bottom panel). $\alpha(t)$ in the sub-diffusive domain gives the power law exponent β of the corresponding MSD. Note that the value of β is specific for each atom in the lipid molecule. Also, the sub-diffusive region, where $\beta \approx$ const. extends over almost four decades, i.e., from 10 ps to 10 ns. The value of β in the sub-diffusive domain, for the cases studied by us, ranges from 0.677 ± 0.005 for the CM of the lipid to 0.427 ± 0.004 for CT, the carbon atoms in the lipid tail (Fig.3.2, bottom panel). The β value for P and CH is ~ 0.49 and for the lipid hydrogen atoms $\beta \sim 0.45$ (Fig.3.2, bottom panel). For all the atoms and the center of mass of the lipids the cross over to the sub-diffusive regime terminates rather abruptly at $\sim$ 10 fs. The linear diffusion regime starts at around 30 ns. These observations indicate that the picosecond dynamics of the constituent atoms of a lipid is location-dependent. However, the long-time linear diffusion of the constituent atoms and lipid molecules seems to be governed by the lipid headgroup atoms.

3.3.2 Memory function approach

The Zwanzig-Mori projection operator method [78] can be used to derive an equation of motion for the MSD, $\langle[\delta r^a(t)]^2\rangle$, for a lipid atom a. The equation of motion for the density ($\rho_a(q,t)$) autocorrelation function $\phi_s^a(q,t) = \langle\rho_a(-q,0)\rho_a(q,t)\rangle$ of a tagged atom a at wave vector q [78]

$$\partial_t^2\phi_s^a(q,t) + q^2v_a^2\phi_s^a(q,t) + \int_0^t M^a(q,t-s)\partial_s\phi_s^a(q,s)\mathrm{d}s = 0. \tag{3.3}$$

Here $v_a = \sqrt{k_BT/m_a}$, k_B is the Boltzmann's constant, T is the temperature, m_a is the mass of atom a, and $M^a(q,t)$ is the memory kernel. The equation of motion for the MSD in 2D can be obtained from $\left\langle[\delta r^a(t)]^2\right\rangle = 4\lim_{q\to0}[1-\phi_s^a(q,t)]/q^2$ which gives

$$\partial_t\langle[\delta r^a(t)]^2\rangle + \int_0^t M_0^a(t-s)\langle[\delta r^a(s)]^2\rangle\mathrm{d}s = 4v_a^2t, \tag{3.4}$$

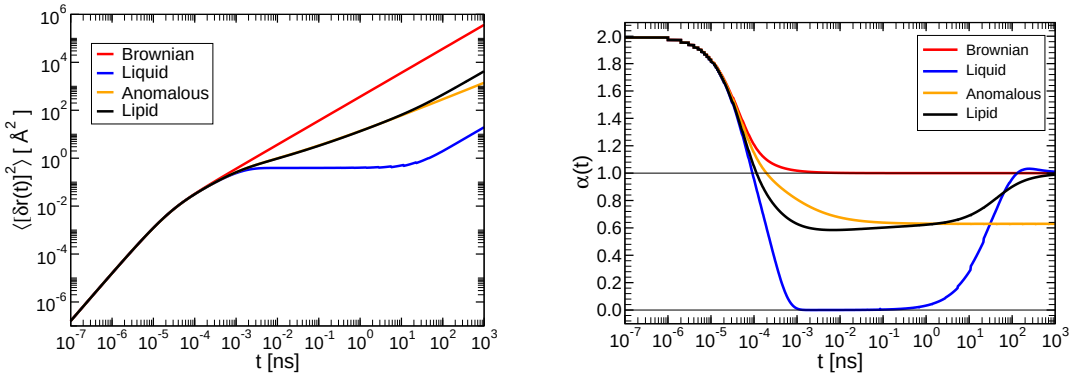

Figure 3.3: Mean square displacement $\langle[\delta r(t)]^2\rangle$ (left) and power-law exponent $\alpha(t)$ (right) corresponding to different memory kernels $M(t)$ as described in the text.

where $M^a(t) = \lim_{q\to 0} M^a(q,t)$. In principle, the MSD can be solved numerically from the above equation once the full memory kernel is known. We propose the following ansatz for the memory function (MF) based on the characteristic features of the MSD profile obtained from the MD simulation

$$M_0^a(t) = \delta(t)/\tau_3^a + \frac{B_a e^{-t/\tau_1^a}}{1+(t/\tau_2^a)^{\beta^a}} \,. \tag{3.5}$$

Here, $\delta(t)$ is the Dirac delta function and the physical meaning of the fitting parameters τ_1^a, τ_2^a, τ_3^a, B_a and β_a is explained below.

At short times the motion of a free Brownian particle is ballistic, with $\langle[\delta r(t)]^2\rangle \sim t^2$ and $\alpha(t) = 2.0$, while at long times the motion becomes diffusive, with $\langle \delta r^2(t)\rangle \sim t$ and $\alpha(t) = 1.0$ (Fig. 3.3, red curve). When $B_a = 0$ Eqs. (3.4)-(3.5) describe the free diffusion of a Brownian particle with a diffusion coefficient $D_3 = k_B T/(\tau_3 m)$. In this case, Eq. (3.4) can be solved analytically to obtain $\langle[\delta r(t)]^2\rangle = 4D_3 t - 4D_3\tau_3(1-e^{-t/\tau_3})$. For $t \ll \tau_3$, $\langle[\delta r(t)]^2\rangle \approx (2k_BT/m)t^2$ corresponding to the ballistic regime, while for $t \gg \tau_3$, $\langle[\delta r(t)]^2\rangle \approx 4D_3 t$ corresponding to the linear diffusion regime. From our MD simulation one infers that $\tau_3 \sim 10$ fs.

For simple liquids, the crossover between the ballistic and linear diffusion regions in the

MSD occurs through a caging region where $\langle[\delta r(t)]^2\rangle$ has a plateau and the corresponding $\alpha(t) = 0$ (Fig. 3.3, blue curve). By neglecting the power-law term in the memory function Eq. (3.5), i.e., by setting $M_a^0(t) = \delta(t)/\tau_3 + B\exp(-t/\tau_1)$, $\langle[\delta r(t)]^2\rangle$ can again be calculated analytically; because the result is rather cumbersome it is not given here. In this case, first the MSD crosses over from the ballistic regime (for $t \ll \tau_3$) to a caging region (for $\tau_3 \ll t \ll \tau_1$) characterized by a plateau in $\langle[\delta r(t)]^2\rangle$ (with $\alpha(t) = 0$) as shown in Fig. 3.3 (blue curve). Then there is a crossover from the caging to the Fickian regimes that takes place around $\tau_1 \sim 10$ ns. The extent of the caging region is determined by the difference between the two time scales τ_3 and τ_1.

The power-law term in the memory kernel, Eq. (3.5), is responsible for the anomalous (sub-)diffusion in the MSD with $\beta \approx \alpha(t) < 1.0$ (Fig. 3.3, orange curve). To illustrate the onset of anomalous diffusion, we have numerically calculated the MSD and the corresponding $\alpha(t)$ for $M_a^0(t) = \delta(t)/\tau_3 + B/[1 + (t/\tau_2)^{-\beta}]$. In this case, as shown in Fig. 3.3 (orange curve), the dynamics gradually crosses over from ballistic to sub-diffusive (with $\beta < 1$) behavior. From our MD simulation follows that the characteristic time scale for the onset on the sub-diffusive regime is $\tau_2 \sim 1$ ps.

By employing the full memory kernel Eq. (3.5), with the three well separated time constants τ_i, i=1,2,3, one obtains for the MSD and α, a time dependence (Fig.3.3, black curves) that matches very well the ones obtained from our MD simulations. To summarize, the three characteristic time constants in the MF, Eq. (3.5), are: $\tau_1 \sim 10$ ns, determining the crossover between the sub- and linear-diffusion regimes; $\tau_2 \sim 1$ ps, determining the onset of the sub-diffusive region; and $\tau_3 \sim 10$ fs, corresponding to the end of the ballistic region.

The fitted MSD for the P atoms and for the center of mass of lipid molecules (CM) are shown in Fig. 3.4. The theoretical MSD matches very well the one obtained from MD simulations (Fig. 3.4) over the entire span of eight decades of time. The insets in Fig. 3.4 show the corresponding $\alpha(t)$. Although the MSD fits are almost perfect, for $t < 1$ps, features in $\alpha(t)$ from the MD simulation are not captured by the MF method. The crossover to Fickian

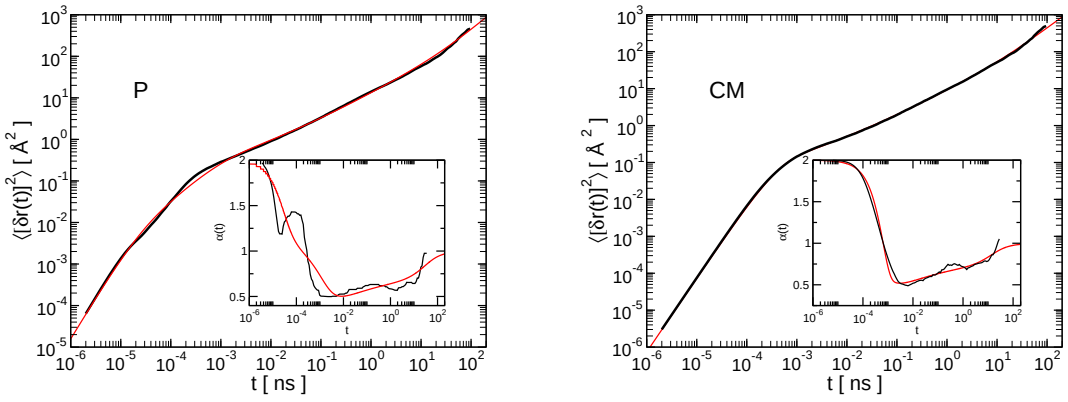

Figure 3.4: Mean square displacement of phosphorus atoms (left) and of the center of mass of lipid molecules (right).The black curves represent $\left\langle \delta r^2(t) \right\rangle$ calculated from MD simulation.The red curves are the fits using the memory function approach, Eqs. (3.4) and Eq. (3.5). The insets show the exponent $\alpha(t) = \partial \ln[\left\langle \delta r_a^2(t) \right\rangle]/\partial \ln(t)$ as a function of time. A running average (1000 time origins) is used to decrease the noise in the simulation data.

diffusion also appears sharper in the MD simulations than in the memory function model.

3.4 Lateral self-diffusion coefficient

While the time dependent MSDs of various atoms (P, CH, CT, H) and the CM of a lipid molecule are well separated in the ballistic and sub-diffusive regions, the crossover to the same Fickian diffusion regime begins around 10 ns corresponding to $\langle [\delta r^a(t)]^2 \rangle \approx 100$ Å^2, i.e., the square of the mean nearest neighbor distance of the lipids (~ 10 Å). MSDs for all atoms and for the CM of lipid molecules converge in the Fickian diffusion regime around $t \sim 30$ ns. This suggests that the system is characterized by a single well defined linear lateral diffusion coefficient that can be calculated from

$$D_{\mathrm{MD}} = \lim_{t\to\infty} \langle [\delta r(t)]^2 \rangle / 4t. \tag{3.6}$$

Indeed, one finds that the diffusion coefficient for all the atoms (P, CH, CT) are close to the diffusion coefficient of the CM, $D_{\mathrm{MD}}^{\mathrm{CM}} = 1.46 \times 10^{-7}$ cm^2 s^{-1} (see Table 3.1). It should

Table 3.1: Diffusion coefficients D_{MD} and D_{MF} for selected lipid atoms and CM calculated from $\langle[\delta r(t)]^2\rangle$ and from our MF method, respectively.

atom	D_{MD} (cm^2 s^{-1})	D_{MF} (cm^2 s^{-1})
CT	1.67×10^{-7}	1.25×10^{-7}
CH	1.27×10^{-7}	1.15×10^{-7}
P	1.30×10^{-7}	1.07×10^{-7}
CM	1.46×10^{-7}	1.06×10^{-7}

be noted that the diffusion coefficient of CM of lipids inferred from the MD simulation is almost twice the value $D_{\mathrm{FRAP}} = 0.69 \times 10^{-7}$ cm^2 s^{-1} obtained from Fluorescence Recovery After Photo-bleaching (FRAP) measurements for DMPC at 34°C [67]. Note that FRAP monitors the motion of lipid molecules on a millisecond (ms) time scale. The discrepancy between the values of D_{MD} and D_{FRAP} may be due to several factors, such as the imperfection of the empirical CHARMM27 force field used in MD simulations, differences between the APL of the experimental and the simulated systems, finite size of the system, and insufficient sampling.

The MF approach provides yet another way of calculating the diffusion coefficient (D_{MF}) of lipid atoms and molecules in a phospholipid bilayer. Inserting $\langle[\delta r(t)]^2\rangle \approx 4Dt$ (valid in the linear diffusion regime where $t \to \infty$) into Eq. (3.4) one obtains

$$D_{\mathrm{MF}} = v_a^2 \left[\int_0^\infty M_0^a(t) dt \right]^{-1}. \tag{3.7}$$

Using the data from our MD simulation one finds that for the CM of the lipid molecules $D_{\mathrm{MF}}^{\mathrm{CM}} \approx 1.06 \times 10^{-7}$ cm^2 s^{-1}. For the P, CH and CT atoms one obtains similar values for the corresponding diffusion coefficients (see Table 3.1). These values are within 30% of the diffusion coefficient $D_{\mathrm{FRAP}} = 0.69 \times 10^{-7}$ cm^2 s^{-1} measured in FRAP experiments.

3.5 Incoherent intermediate scattering functions

Neutron scattering experiments can be used to investigate the dynamical properties of lipid bilayers [44, 45, 47, 71, 79, 80]. Inelastic (INS) and quasi-elastic (QENS) neutron scattering experiments probe the system on sub ns time scales, which correspond to the sub-diffusive region (see Sec 3.6). It appears that quite erroneously INS data on lipid membranes are interpreted assuming linear diffusion dynamics in spite of the fact that most likely the probed system is in a sub-diffusive regime. To understand the implication of the sub-diffusive region in the results of neutron scattering, we examined the incoherent intermediate scattering function of different atoms, and the center of mass of lipid molecules.

The differential cross-section of the quasi-elastic scattering of neutrons in a solid angle $d\Omega$ with an energy transfer $\hbar\omega$ can be expressed as [81]

$$\frac{\mathrm{d}\sigma^2}{\mathrm{d}\Omega \mathrm{d}\omega} \propto \sum_n (b^n_{inc})^2 \, S^n_s(q,\omega) + \sum_{n,m} b^n_{coh} b^m_{coh} S^{nm}_{coh}(q,\omega), \tag{3.8}$$

where n, m are atom-type indices, while b^n_{inc} [b^n_{coh}] and $S^n_s(q,\omega)$ [$S^{nm}_{coh}(q,\omega)$] are, respectively, the incoherent (coherent) scattering length and dynamic structure factor (DSF). $S^n_s(q,\omega)$ contains information about the single particle motion of nuclei of type n, and in principle it can be used to determine the self diffusion coefficient D (see Sec. 3.6). The incoherent intermediate scattering function (IISF), $I^n_s(q,t)$, is the inverse time Fourier transform of the incoherent DSF, $S^n_s(q,\omega)$, that is measured in QENS experiments. For any selection of atoms, the IISF can be easily calculated from all-atom MD simulations by using the formula

$$I^n_s(q,t) = \frac{1}{N_n} \left\langle \sum_{m=1}^{N_n} e^{i\vec{q}\cdot[\vec{r}^n_m(0) - \vec{r}^n_m(t)]} \right\rangle, \tag{3.9}$$

where the summation goes over all N_n atoms of type n. In the case of equilibrium MD simulations, the statistical mechanical average $\langle \ldots \rangle$ in Eq. (3.9) is evaluated as a time

average over a sufficiently long MD trajectory.

Within the lowest order cumulant (i.e., Gaussian) approximation, the IISF can be expressed in terms of the MSD as follows [78]

$$I_s^g(q,t) = \exp\left(-q^2\langle[\delta r^n(t)]^2\rangle/4\right) . \tag{3.10}$$

The corresponding second order cumulant approximation reads [78]

$$I_s^{ng}(q,t) \approx \exp\left(-q^2\langle[\delta r^n(t)]^2\rangle/4\right) \times \left[1 + (\gamma^n(t)/2)\left(q^2\left\langle[\delta r^n(t)]^2\right\rangle/4\right)^2\right], \tag{3.11}$$

where

$$\gamma^n(t) = \left(\left\langle[\delta r^n(t)]^4\right\rangle/2\left\langle[\delta r^n(t)]^2\right\rangle - 1\right) \tag{3.12}$$

is a non-Gaussian parameter.

We have tested the validity of both Gaussian $I_s^g(q,t)$, and non-Gaussian $I_s^{ng}(q,t)$ approximations of $I_s^n(q,t)$ for several lipid atoms (P, CH and CT) and q values ($q \in \{1.42, 0.75, 0.5\}$ Å^{-1}). The results for $I_s^g(q,t)$ are shown in Fig. 3.5 for two q values (1.42 and 0.75 Å^{-1}). For the P atoms (squares), the Gaussian approximation (solid curve) matches quite well $I_s^n(q,t)$ for all q values. The same approximation for the CH (triangles) and the CT (circles) atoms show noticeable deviations from $I_s^n(q,t)$ in the sub-diffusion regime, especially for larger q values.

To estimate the size of the non-Gaussian correction to $I_s^g(q,t)$, we have calculated the parameter $\gamma^n(t)$ for the (P, CH and CT) atoms, for the CM and the hydrogen atoms of the lipids (shown in Fig.3.6). $\gamma^n(t)$ is noticeably different from zero for the CH (triangle), CT (circle) and hydrogen (red curve) atoms in the extended sub-diffusive region. Thus, at least for CH and CT, the IISF should be calculated using the non-Gaussian expression (3.11). As shown in the left panel of Fig. 3.7, $I_s^{ng}(q,t)$ matches rather well $I_s^n(q,t)$ for the CT atoms for both q values considered. The non-Gaussian approximation also holds true for CH atoms

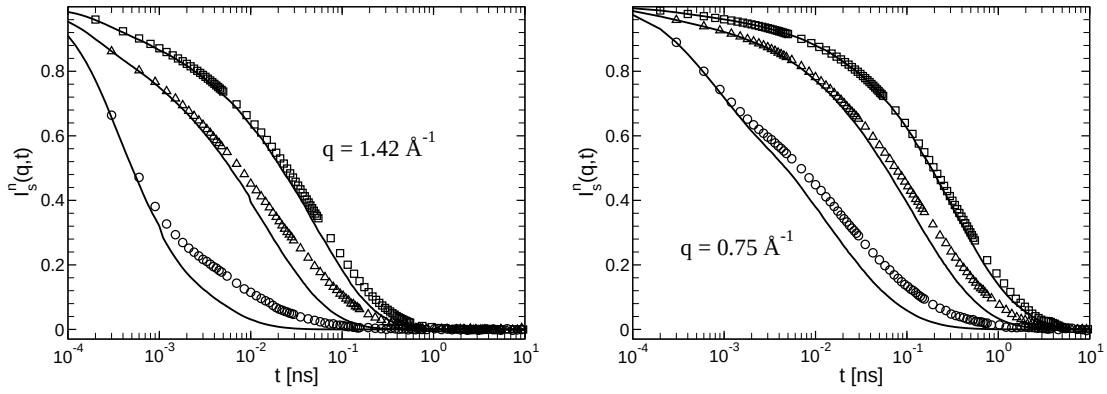

Figure 3.5: Self intermediate scattering function for P (squares), CH (triangles) and CT (circles) atoms for $q = 1.42\text{Å}^{-1}$ (left) and $q = 0.75\text{Å}^{-1}$ (right).The solid curves correspond to the Gaussian approximation, $I_s^g(q,t)$.

(not shown).

We notice that, the non-Gaussian correction to the IISF comes mainly from the sub-diffusive region characterized by a power law t-dependence of the MSD of the lipid atoms. Thus, an alternative to Eq. (3.11) for approximating $I_s^n(q,t)$ is to employ a stretched exponential, i.e., the KohlRaush-William-Watt (KWW) function, $A(q)\exp[-[t/\tau(q)]^{\beta(q)}]$. Here, the $\tau(q)$ and $\beta(q)$ have a non trivial q dependence. Note that smaller q corresponds to bigger spatial distance and thus implicitly implies longer time dynamics. Conversely, larger q means smaller displacements implying shorter time dynamics.

The KWW approximation provides a reasonable fit to $I_s^n(q,t)$, especially for q and t values that lie within the sub-diffusive region. For the P atoms, the q dependence of the fitting parameters $\beta(q)$ (circles) and $D(q) = 1/[\tau(q)q^2]$ (squares) is shown in Fig. 3.8, left panel. As expected, $\beta(q)$ approaches 0.6 at q = 0.75 Å^{-1} and stays constant until q = 0.6 Å^{-1}.

For small q values and long times, the system moves into the 2D linear diffusion regime and $\langle \delta r^2(t) \rangle \approx 4Dt$. Inserting this in Eq. (3.10) one can obtain

$$I_s^n(q,t) \approx e^{q^2 Dt}. \tag{3.13}$$

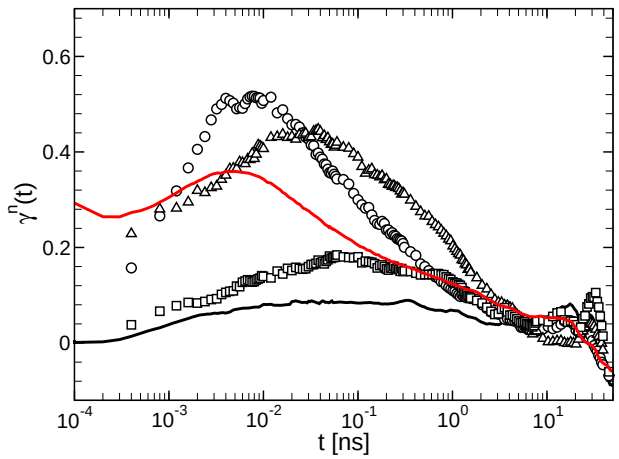

Figure 3.6: Time dependence of the non-Gaussian parameter $\gamma^n(t)$ for the P (squares), CH (triangles), CT (circles), and for the center of mass (black solid curve) and for the average over all the hydrogen atoms (red solid curve).

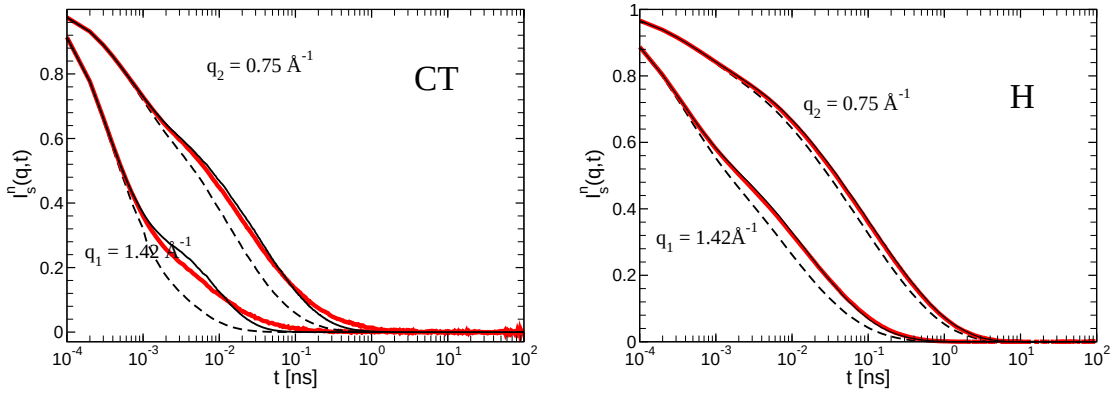

Figure 3.7: IISF for the CT atoms (left panel) and for the H atoms (right panel) for two scattering vectors $q_1 = 1.42$ Å^{-1} and $q_2 = 0.75$ Å^{-1}. The dashed curves represent the Gaussian approximation Eq.(3.10), the thin-solid curves the non-Gaussian approximation Eq.(3.11), and the thick (red) curves the exact IISF calculated using Eq. (3.9).

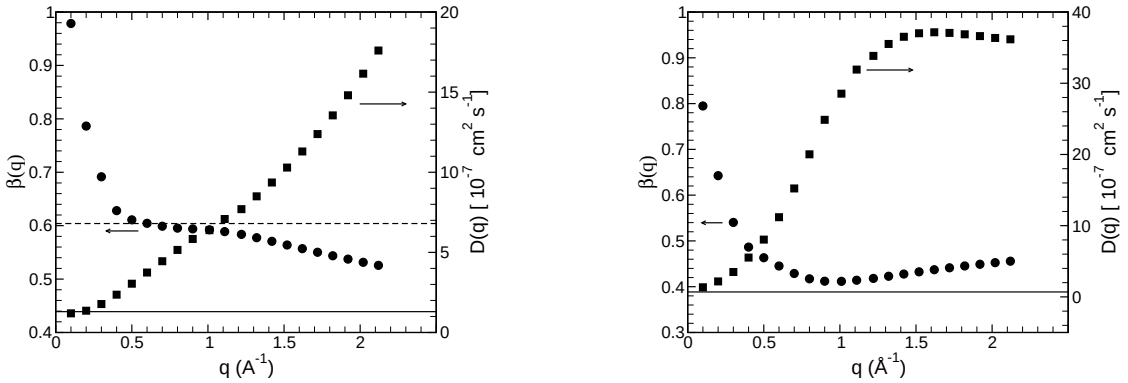

Figure 3.8: q dependence of the fitting parameters $\beta(q)$ (circles and left axis) and $D(q) = 1/[\tau(q)q^2]$ (squares and right axis) used in the KWW approximation to the self intermediate scattering function $I_s^n(q,t)$ for the P atoms (left panel) and for the H atoms (right panel).

This implies that for small enough q the KWW approximation should cross over to the linear diffusion results $I(q,t) \approx \exp(-q^2Dt)$. Thus in the $q \to 0$ limit, one expects that $\beta(q) \to 1$ and $D(q) = 1/[\tau(q)q^2] \to D$. These trends are manifest in Fig. 3.8 and one may infer that the linear diffusion coefficient D for the P atoms (and for the lipid molecules as well) should be smaller than $1.30 \times 10^{-7}\text{cm}^2\text{s}^{-1}$.

KWW (stretched exponential) fit was also applied to analyze the IISF $I_s^H(q,t)$ of hydrogen atoms of lipid molecules. The fitting parameters $\beta(q)$ and $D(q) = 1/[q^2\tau(q)]$ are depicted in the right panel of Fig. 3.8. For q = 1.42 Å^{-1} (the peak for the static structure factor in the lipid tails), $\beta(q)$ = 0.43 which is similar to the sub-diffusive exponent obtained from the corresponding MSD of H atoms. At q = 0.5 Å^{-1}, the value of $\beta(q)$ increases sharply to 1.0 and the value of $D(q)$ starts leveling off asymptotically to $D_H = 1.62 \times 10^{-7}$ cm^2 s^{-1} which is close to $D_{\text{MD}}^{\text{CM}}$ = 1.46 $\times$ 10^{-7} cm^2 s^{-1} obtained from the linear fit to the MSD of lipid CM. But our simulation is too short to be used in the $q \to 0$ limit, which is necessary for determining the precise asymptotic value of $D(q)$.

For the other lipid atoms and for the CM of lipid molecules we obtained similar results (data not shown). Therefore, it appears that, indeed, $D(q)$ is independent of the selected atom type once in the linear diffusion regime that corresponds to small q values.

3.6 Lateral self-diffusion coefficient from neutron scattering experiments

Several experimental studies have been employed to investigate the dynamics of the phospholipid molecules in lipid bilayers and to calculate the lateral self-diffusion coefficient of lipid molecules [45–47]. Interestingly, the obtained values for the diffusion coefficient from these experiments are rather different. For example, in quasi-elastic neutron scattering (QENS) experiments the diffusion coefficient of lipids is determined from the incoherent dynamic structure factor (IDSF), $S_s^n(q,\omega)$. The published D_{NS} values for 1,2-Dipalmitoyl-sn-Glycero-3-Phosphocholine (DPPC) from various QENS experiments are shown in Table 3.2 [45–47]. We found that $D(q)$ increases with q and with the energy of the probing neutron beam (see Table 3.2).

Table 3.2: Diffusion coefficients for DPPC in the fluid phase determined by neutron scattering for different time and length scales.

Expt.	Technique	T	length scale	time scale	D_{NS}
1 [47]	QENS (IN10)	41 °C	0.07-2 Å^{-1}	5 ns (0.8 μeV)	1.8×10^{-7} cm^2/s
2 [45]	QENS (IN10)	41 °C	1-2 Å^{-1}	5 ns (0.8 μeV)	1.6×10^{-6} cm^2/s
3 [46]	QENS (IN5)	45-55 °C	0.2-1.6 Å^{-1}	66 ps (63 μeV)	3.5×10^{-6} cm^2/s

The analysis of our MD simulation data in Sec. 3.5 led to a similar behavior for $D(q)$, as shown in Fig. 3.8. Because the structural difference between the DPPC (used in experiments) and DMPC (used in our MD simulations) lipid molecules is minimal (e.g., DMPC has a slightly shorter acyl chain than DPPC, i.e., 14 vs 16 carbon atoms) one expects very similar lateral diffusion coefficient for both type of lipids for the same APL.

In general, the linear diffusion coefficient is a constant that does not depend, e.g., on q and ω of the probing neutron beam used in the NS experiment. Nevertheless, the diffusion coefficients D extracted from the QENS experiments have a clear q and ω dependence. The origin of this inconsistency in the experimental D values is due to the erroneous as-

sumption that the system is in the linear diffusion regime (characterized by $\langle[\delta r(t)]^2\rangle \sim$ t) instead of the sub-diffusive one (characterized by $\langle[\delta r(t)]^2\rangle \sim t^{\beta}$, with β <1). Indeed, to determine the lateral diffusion coefficient D_{NS} from NS experiments, in general, the measured dynamics structure factor ($S_s^n(q,\omega)$) is fitted with a Lorentzian [78]

$$S_s^n(q,\omega) = \frac{1}{\pi}\frac{q^2D + 1/\tau_R}{(q^2D + 1/\tau_R)^2 + \omega^2}. \tag{3.14}$$

Here τ_R is inversely proportional to the energy resolution window of the instrument and the altered $I_s^n(q,t) = e^{(-q^2D - 1/\tau_R)t}$. The diffusion coefficient D is evaluated in terms of the half width at half maximum (HWHM) ω_0 of the Lorentzian (Eq. (3.14)), i.e.,

$$D = \frac{\omega_0\tau_R - 1}{q^2\tau_R}. \tag{3.15}$$

Note that only if $\tau_R \gg 1/(q^2D)$, can the instrument probe the linear diffusion regime of the system. However, in the mentioned QENS experiments [45–47] (see also Table 3.2, column 5), the used energy resolution window were rather short, ranging from $\tau_R \sim 60$ ps to $\tau_R \sim 5$ ns. We have already established from our MD simulation of a DMPC bilayer that the lipid atoms and molecules execute sub-diffusive motion in this time range. Therefore, one should conclude that it is not correct to calculate D from the HWHM of a Lorentzian fit of the experimentally measured dynamics structure factor $S_s^n(q,\omega)$. This procedure not only grossly overestimates D, but also leads us to an erroneous q and ω dependence of D.

To demonstrate this point, we have determined D by fitting $S_s^n(q,\omega)$ with a Lorentzian. $S_s^n(q,\omega)$ is obtained as the Fourier Transform (FT) of $I_{\mathrm{MD}}(q,t)$, which is calculated directly from MD simulation data by using Eq. (3.9). D_{MD} is then calculated from Eq. (3.15), where ω_0 is the HWHM of the corresponding Lorentzian fit. The obtained D_{MD} values are listed in column 4 of Table 3.3 for both the P and H atoms for $q \in \{0.2, 0.75\}$ Å^{-1} and for four τ_R values, $\tau_R \in \{\infty, 10, 1, 0.1\}$ ns. For small q and large τ_R, the value of D_{MD}, for both

Table 3.3: Diffusion coefficients calculated from HWHM of $S(q,\omega)$ for phosphorus (P) and hydrogen (H) atoms.

Atom	q (Å^{-1})	τ_R (ns)	$D_{\rm MD}$ ($\times 10^{-7}$ cm^2/s)	D_s^g ($\times 10^{-7}$ cm^2/s)	D_s^{ng} ($\times 10^{-7}$ cm^2/s)
P	0.2	∞	1.129	0.989	-
		10	1.125	1.065	-
		1	2.120	2.037	-
		0.1	5.067	5.009	-
	0.75	∞	1.903	2.093	-
		10	1.948	2.222	-
		1	2.619	3.020	-
		0.1	5.148	5.462	-
H	0.2	∞	1.422	1.119	0.739
		10	1.489	1.375	1.286
		1	3.355	3.216	3.488
		0.1	10.784	10.571	10.753
	0.75	∞	1.698	2.814	5.814
		10	2.041	2.998	6.015
		1	3.107	4.253	7.412
		0.1	8.166	10.348	14.297

P and H atoms, are close to the diffusion coefficients obtained from FRAP experiments, $D_{\rm FRAP} = 0.69 \times 10^{-7}$ cm^2/s, and from MD simulation, $D_{\rm CM}$ = 1.46 $\times$ 10^{-7} cm ^{2}/s. As τ_R decreases, the value of $D_{\rm MD}$ increases monotonically for fixed q values for both P and H atoms. Also, for both types of atoms, for the same τ_R, $D_{\rm MD}$ increases with q. Thus, these results for $D_{\rm MD}$ are in total agreement with the previously mentioned experimental findings for $D_{\rm NS}$.

An alternative way of calculating $S_s^n(q,\omega)$, is to take the FT of the incoherent intermediate scattering functions that are obtained by using the first order (Gaussian) or the second order (non-Gaussian) cumulant approximation. The diffusion coefficient is then calculated using the HWHM obtained from the corresponding Lorentzian fit. We denote by D_s^g and D_s^{ng} the diffusion coefficient calculated by using the Gaussian approximation (I_s^g in Eq. (3.10)) and the non-Gaussian approximation (I_s^{ng} in Eq. (3.11)), respectively.

For the P atoms, at small q (0.2 Å^{-1}), the FT of IISF obtained from the Gaussian

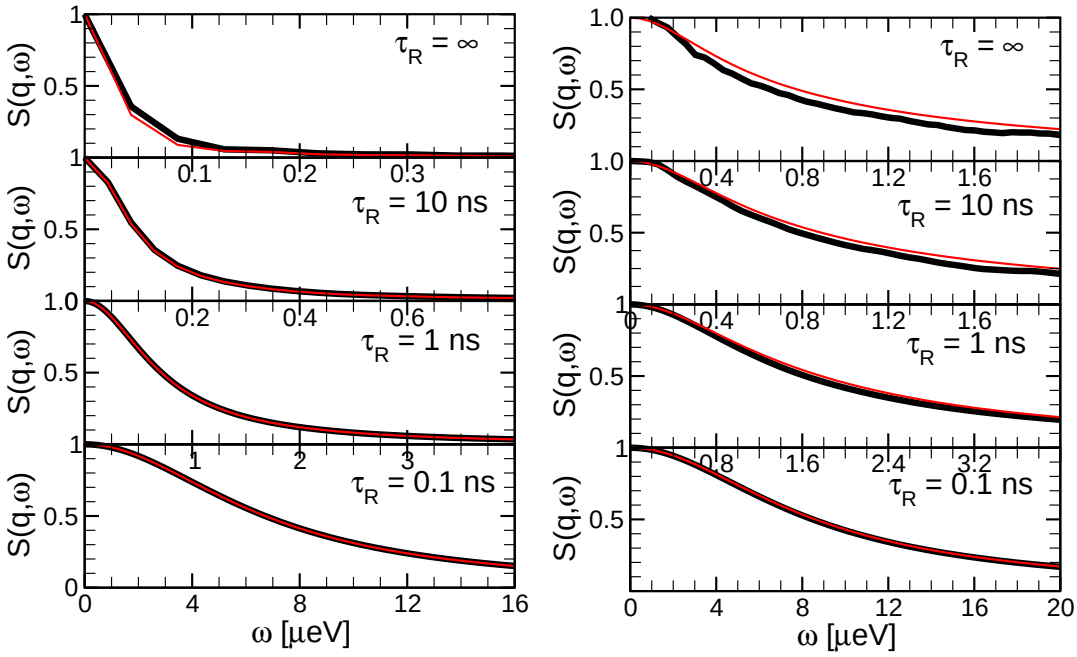

Figure 3.9: Dynamic structure factor of P atoms in DMPC lipid molecules for $q = 0.2$ Å^{-1} (left panel) and $q = 0.75$ Å^{-1} (right panel). The Gaussian approximation, $I_s^g(q,t) = \exp(-q^2\langle[\delta r(t)]^2\rangle/4))$ is shown as red curve. $I_{\rm MD}(q,t)$ is shown as thick black curve.

approximation reproduces $S_s^n(q,\omega)$ very well (Fig. 3.9, left panel). However, for large q (0.75 Å^{-1}), the Gaussian approximation slightly overestimates $S_s^n(q,\omega)$ (Fig. 3.9, right panel) especially for large τ_R values. Similarly to $D_{\rm MD}$, the values of D_s^g are dependent upon the q and τ_R values (Table 3.3, column 5).

In the case of the H atoms, we consider both the Gaussian and the non-Gaussian approximations for calculating the IISF. This is motivated by the fact that the non-Gaussian parameter is large for H atoms in the sub-diffusive regime. For small q (= 0.2 Å^{-1}), the FT of the IISF obtained by using both the Gaussian and the non-Gaussian approximations are indistinguishable from the corresponding $S_s^n(q,\omega)$ (Fig. 3.10, left panel). For q = 0.75 Å^{-1}, the Gaussian approximation exhibits noticeable deviation from $S_s^n(q,\omega)$ but the non-Gaussian approximation matches closely $S_s^n(q,\omega)$ (Fig. 3.10, right panel). For H atoms, both D_s^g and D_s^{ng} increase with increasing q and decreasing τ_R, similarly to the corresponding $D_{\rm MD}$. This analysis confirms again that one obtains incorrect $D_{\rm NS}$ from the experimen-

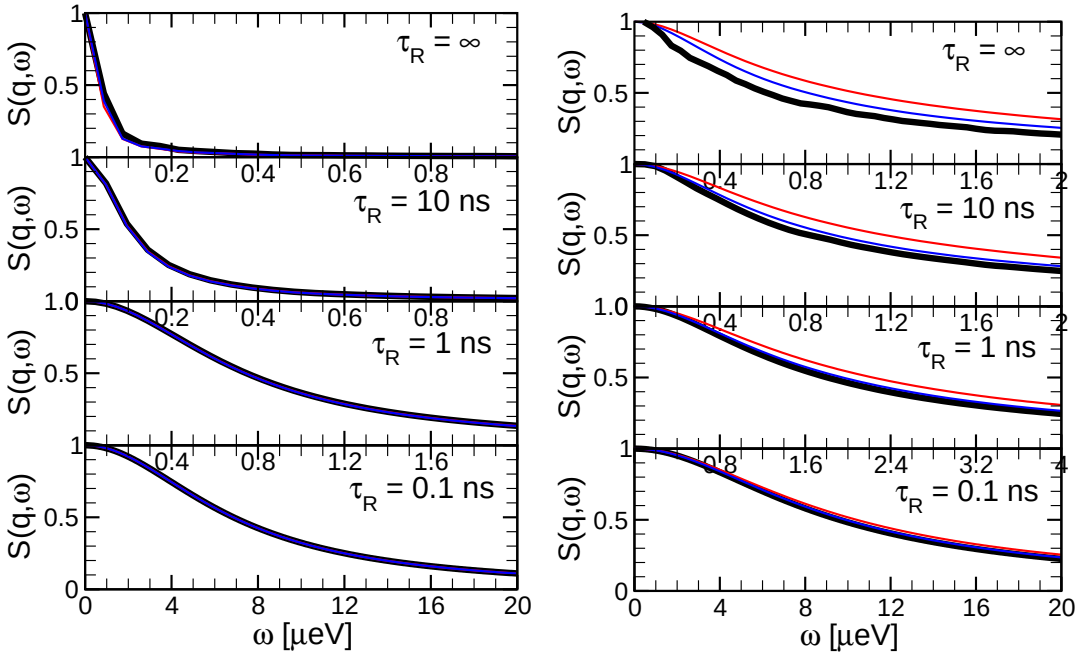

Figure 3.10: Dynamic structure factor of H atoms in DMPC lipid molecules for q = 0.2 Å^{-1} (left panel) and q = 0.75 Å^{-1} (right panel). The Gaussian approximation, $I_s^g(q,t)$ is shown as a red curve. $I_{\mathrm{MD}}(q,t)$ is shown as a thick black curve. The non-Gaussian approximation, I_s^{ng}(q,t) is shown as a blue curve.

tally measured DSF if one assumes that the system is in the linear diffusion regime. The correct determination of D_{NS} requires to take into account that NS experiments probe the sub-diffusive regime of the hydrated lipid bilayer and not the linear diffusive one.

The phenomenological memory function model proposed by us can provide both the t-dependence of the MSD (Sec. 3.3.2) and the value of D (Sec. 3.4) provided that one knows the three time constants characterizing the onset of the ballistic, sub-diffusive and linear diffusive regimes. Thus, our MF based method provides an alternative approach to find D from $S_s^n(q,\omega)$ measured in QENS experiments. The key to success in our approach is to find the correct set of fitting parameters in the MF, defined by Eq. (3.5). In the absence of experimental $S_s^n(q,\omega)$, to demonstrate our MF method, we identify $S_s^n(q,\omega)$ with the one calculated from our MD simulation. As before, the DSF is determined through numerical Fourier transform on $I_{\mathrm{MD}}(q,t) \times e^{-t/\tau_R}$. We denote the result as $S_{\mathrm{MD}}(q,\omega)$. The factor e^{-t/τ_R} accounts for the energy resolution window of the instrument. The essence of our

MF method is to determine the fitting parameters in the MF, Eq. (3.5), that leads to a DSF that "best" fits the experimental $S_{\mathrm{MD}}(q,\omega)$. The procedure is illustrated in Fig. 3.11 and is explained next.

We begin by using a properly chosen initial set of values for the parameters, $P_i = \{\tau_1, \tau_2, \tau_3, B, \beta\}_i$ to calculate $M(t)$. For example, one can set the initial values of τ_i, i=1,2,3, to the already identified characteristic time scales τ_1 ($\sim$10 ns), τ_2 ($\sim$1 ps) and τ_3 ($\sim$ 10 fs). Once the $M(t)$ is constructed, the MSD is calculated numerically by solving Eq. (3.4). Then, the $I_{\mathrm{MF}}(q,t)$ is calculated in terms of the MSD by using the Gaussian approximation, Eq. (3.10). Next, by applying numerical FT on $I_{\mathrm{MF}}(q,t) \times e^{-t/\tau_R}$, we obtain the corresponding $S_{\mathrm{MF}}(q,\omega)$. The new values of the fitting parameters P_n are determined by minimizing $\chi^2 = \sum_{m=1}^{N} [S_{\mathrm{MD}}(q,\omega) - S_{\mathrm{MF}}(q,\omega)]^2$ through a least-squares fit approach involving the Nelder-Mead algorithm [82, 83]. If χ^2 is smaller than a predefined small value ε (or if the maximum number of iteration steps has been reached) the final, hopefully converged, MF is calculated with the final values of the fitting parameters. Otherwise, the above procedure is repeated by replacing the values of the fitting parameters from the previous iteration with the current ones.

Finally $M(t)$ is used to calculate the diffusion coefficient D according to Eq. (3.16)

$$D = v^2 \left[\int_0^{\tau^*} M(t) dt \right]^{-1}, \tag{3.16}$$

where $v = \sqrt{k_B T/m}$ is the thermal velocity and τ^* is a characteristic time defined below. It should also be emphasized that, when $\tau_R \leq 10$ ns, the phospholipid bilayer is in the sub-diffusive regime and the experimental $S_s^n(q,\omega)$ contains no information about the linear diffusive regime. In such cases, the appropriate form for the memory function is, $M_{\mathrm{sub}}(t) = \delta(t)/\tau_3 + B/(1+(t/\tau_2)^{\beta})$, which excludes the linear diffusion region and, therefore, is valid only for $t < \tau_1$. Thus, in order to calculate D using $M(t) \approx M_{\mathrm{sub}}(t)$ in Eq. (3.16) one needs to set the upper limit of the integral to $\tau^* \sim \tau_1$. On one hand, D is underestimated by

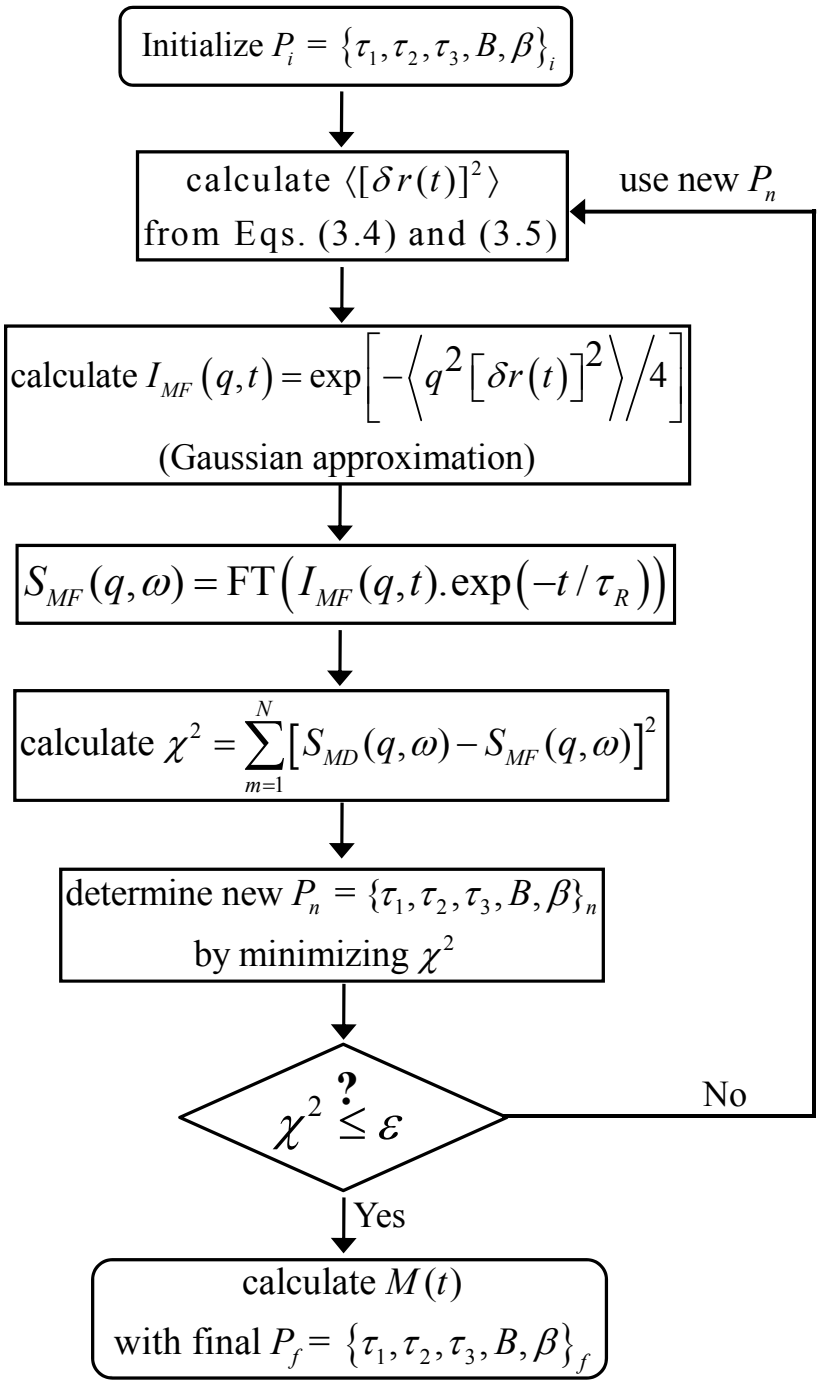

Figure 3.11: Flowchart based on MF model for obtaining the fitting parameters $P_f = \{\tau_1, \tau_2, \tau_3, \mathrm{B}, \beta\}_f$ for final, converged $M(t)$ that "best" fits experimental DSF.

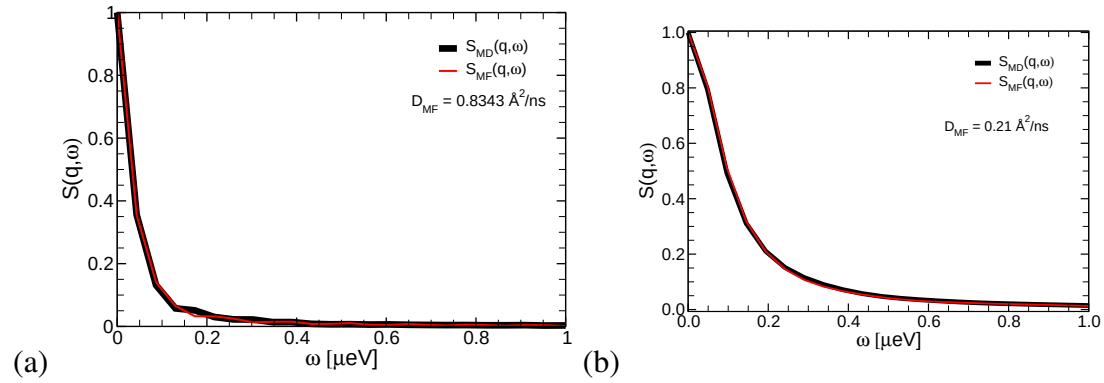

Figure 3.12: $S(q,\omega)$ vs ω for P atoms for q = 0.2 Å^{-1} and (a) $\tau_R = \infty$ ns, and (b) τ_R = 10 ns. $S_{\rm MD}(q,\omega)$ is represented by solid thick black curves. Red curves represent $S_{\rm MF}(q,\omega)$. $S_{\rm MF}(q,\omega)$ calculated from the final, converged M(t) matches well $S_{\rm MD}(q,\omega)$.

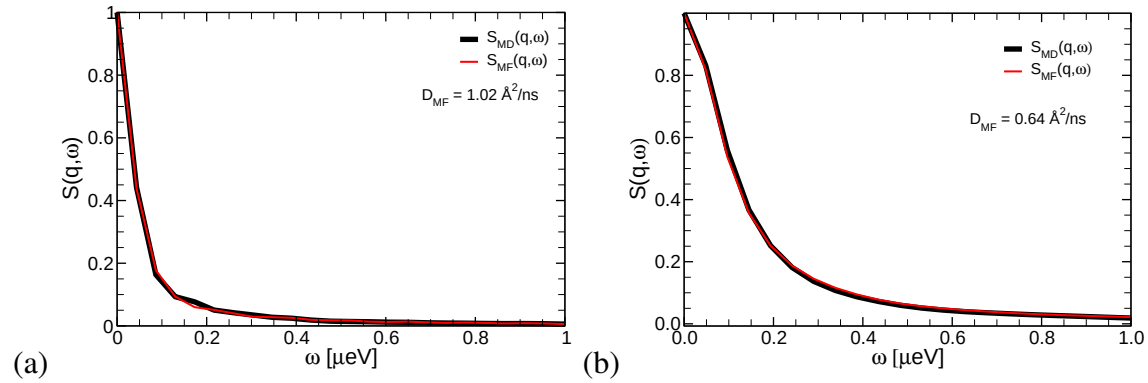

Figure 3.13: $S(q,\omega)$ vs ω for H atoms for q = 0.2 Å^{-1} and (a) $\tau_R = \infty$ ns, and (b) τ_R = 10 ns. $S_{\rm MD}(q,\omega)$ is represented by solid thick black curves. Red curves represent $S_{\rm MF}(q,\omega)$. $S_{\rm MF}(q,\omega)$calculated from the final, converged M(t) matches well $S_{\rm MD}(q,\omega)$.

setting e^{-t/τ_1}=1 in $M(t)$ to obtain $M_{\rm sub}(t)$. On the other hand, however, D is overestimated by cutting the time integral off at τ^* in Eq. (3.16). How well these two effects cancel each other depends on the proper choice of τ^*. It is quite remarkable that through this approach one can calculate the diffusion coefficient D without any information about the linear diffusion regime.

$S_{\rm MF}(q,\omega)$ calculated by using the MF approach (red curves) are in good agreement with $S_{\rm MD}(q,\omega)$ (black curves) for both the P and H atoms. For P atoms and q = 0.2 Å^{-1}, the fits are shown in Fig. 3.12. The fits corresponding to the H atoms are shown in Fig. 3.13 (q = 0.2 Å^{-1}) and Fig. 3.14 (q = 0.75 Å^{-1}). The fitting parameters for P and H atoms are

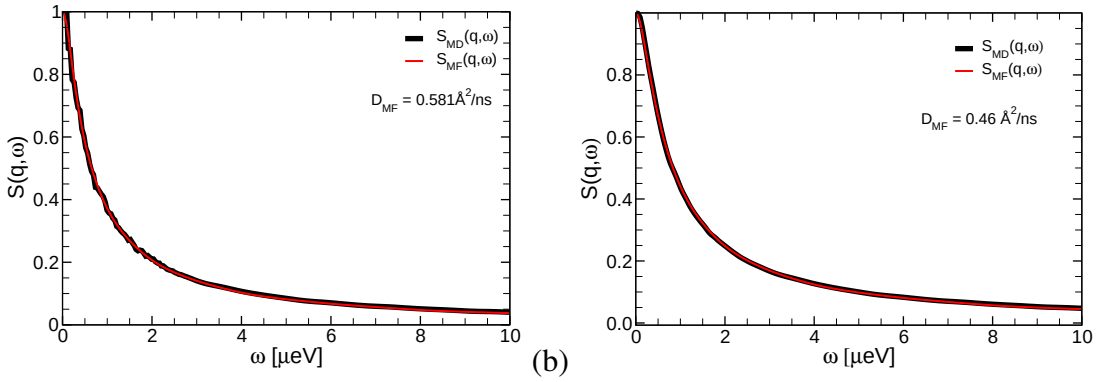

Figure 3.14: $S(q,\omega)$ vs ω for H atoms for $q = 0.75$ Å^{-1} and (a) $\tau_R = \infty$ ns, and (b) $\tau_R = 10$ ns. $S_{\rm MD}(q,\omega)$ is represented by solid thick black curves. Red curves represent $S_{\rm MF}(q,\omega)$. $S_{\rm MF}(q,\omega)$calculated from the final, converged $M(t)$ matches well $S_{\rm MD}(q,\omega)$.

given in Table 3.4. The corresponding D values for P and H atoms are listed in Table 3.4 (column 9). The estimated D for P and H atoms are of the same order of magnitude as the experimental diffusion coefficient $D_{\rm FRAP}$.

Table 3.4: Fitting parameters for $S_{\rm MF}(q,\omega)$ the P and the H atoms.

Atom	q (Å^{-1})	τ_R (ns)	B (ps^{-2})	τ_1 (ns)	τ_2 (ps)	τ_3 (fs)	β	D ($\times 10^{-7}$ cm^2/s)
P	0.2	∞	88.65	18.8	1.0	11.5	0.60	0.84
		10	5.5	-	0.1	6.2	0.11	0.2
H	0.2	∞	639.51	31.0	0.40	1.04	0.43	1.0
		10	146.63	-	0.64	1.98	0.24	0.64
	0.75	∞	1329.02	24.3	0.54	2.75	0.44	0.58
		10	1479.48	-	0.42	2.74	0.44	0.46

The discrepancy for H atoms may come from the the fact that we use the Gaussian approximation for IISF, which in this case is a rather poor approximation. For H atoms one may improve the results for D by employing the non-Gaussian approximation for calculating IISF. However, incorporating the non-Gaussian approximation in our MF approach is more complicated, as it involves $\left\langle [\delta r(t)]^4 \right\rangle$ besides the MSD. Such an extension of the proposed MF method is beyond the scope of this thesis.

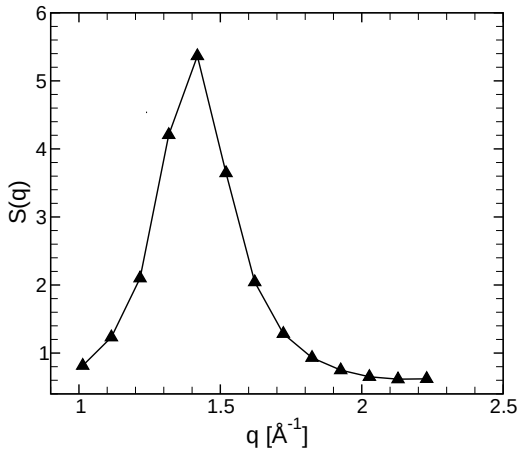

Figure 3.15: The static structure factor $S(q)$ as a function in-plane scattering wave vector q from MD simulation.

3.7 Correlated dynamics in fluid phospholipid membranes

In this section, we investigate the in-plane correlated dynamics of phospholipid molecules by using our 0.1 μs all-atom MD simulation of a hydrated DMPC bilayer described in Sec. 3.2. Our goal is to estimate the correlation length and correlation time of the concerted motion of lipid atoms and molecules in the model DMPC lipid bilayer.

First, we have calculated the static structure factor $S(q)$ for the carbon atoms in the tail of the phospholipid molecules. $S(q)$ can be written as

$$S(q) = \frac{1}{N} \sum_{i=1}^{N} \sum_{j=1}^{N} \langle e^{-i\vec{q}\cdot\vec{r}_i} \, e^{i\vec{q}\cdot\vec{r}_j} \rangle, \tag{3.17}$$

where $\vec{q}$ is the in-plane scattering wave vector, parallel to the xy plane of the lipid bilayer (Fig. 3.1, left panel) and $\vec{r}_i$ is the position vector for i^{th} atom at $t = 0$. The $S(q)$ for carbon atoms in the DMPC tails depicted in Fig. 3.15 shows that there is a peak at q = 1.42 Å^{-1}. This q in momentum space corresponds to the nearest neighbor distance between two DMPC lipid tails in real space.

To analyze the structural relaxation of the lipid tails, the in-plane incoherent $I_s(q,t)$ (Eq. (3.18a)) and the coherent $I_c(q,t)$ (Eq. (3.18b)) intermediate scattering functions are computed.

$$I_s(q,t) = \frac{1}{N}\sum_n \langle e^{-i\vec{q}\cdot[\vec{r}_n(0)-\vec{r}_n(t)]}\rangle; \tag{3.18a}$$

$$I_c(q,t) = \frac{1}{N}\sum_n \sum_m \langle e^{-i\vec{q}\cdot[\vec{r}_n(0)-\vec{r}_m(t)]}\rangle. \tag{3.18b}$$

Here the sums are taken over the N carbon atoms in the lipid tails and $\vec{r}_n(t)$ is the position of the n^{th} atom at time t. To study the purely coherent and incoherent contributions to the scattering due to the carbons within the lipid tails we have examined $I_c(q,t)$ and $I_s(q,t)$ for nine different $q \in \{1.01, 1.22, 1.32, 1.42, 1.52, 1.62, 1.82, 2.02, 2.13\}$ Å^{-1} values. Figure 3.16 shows $I_s(q,t)$ (black curve) and $I_c(q,t)$ (red curve) for three representative q values, $q \in \{1.01, 1.42, 2.13\}$ Å^{-1}. From Fig. 3.16, it can be observed that $I_c(q,t)$ decays slower than $I_s(q,t)$ for q = 1.42 Å^{-1}, whereas, for the other two q values, it is $I_s(q,t)$ that decays slower than the corresponding $I_c(q,t)$.

To determine quantitatively the decay rates of the coherent and incoherent intermediate scattering functions, a decay time $\tau(q)$ is defined through the equation $I_{s/c}(q,\tau)/I_{s/c}(q,0) = e^{-1}$. Figure 3.17 shows $\tau_s(q)$ (squares) and $\tau_c(q)$ (circles) as a function of the momentum vector q. According to these plots, $\tau_s(q)$ decreases monotonically with increasing q, while $\tau_c(q)$ has a distinct non-monotonic behavior with a maximum around q = 1.42 Å^{-1}. Indeed, the difference $\Delta\tau = \tau_c(q) - \tau_s(q)$ has a maximum at q = 1.42 Å^{-1} (Fig. 3.17, red curve) and clearly indicates that the relaxation rate of the structure of the DMPC tails is the slowest at their nearest neighbor distance, q = 1.42 Å^{-1}. The significance of this slowing down of the coherent relaxation rate i.e. longer relaxation time around the maximum of $S(q)$ is known as *de Gennes narrowing* [84]. This phenomenon indicates that a strong correlation exists between the DMPC tails around q = 1.42 Å^{-1} along the plane of the membrane. In principle, neutron scattering experiments can detect such correlations. Applying neutron backscattering technique on DMPC bilayer system at 303 K, it has been observed that

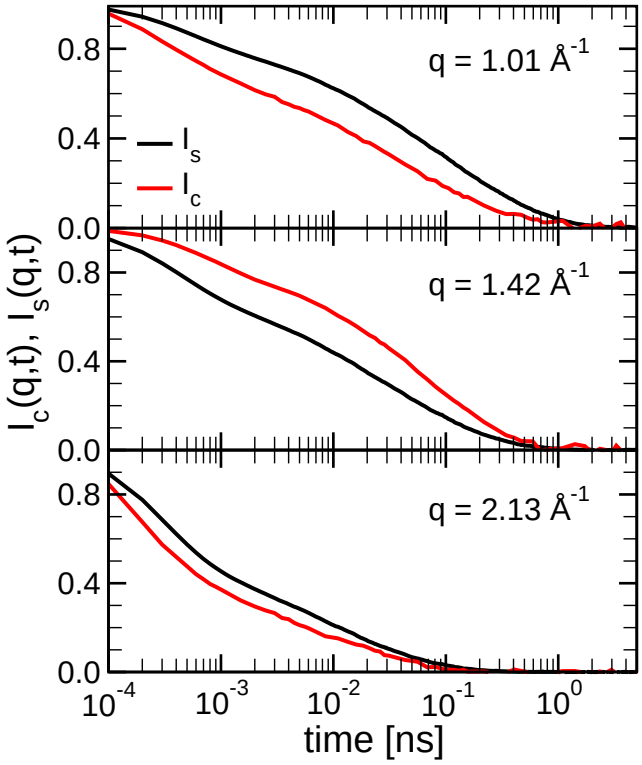

Figure 3.16: Time evolution of $I_s(q,t)$ (black curve) and $I_c(q,t)$ (red curve) for three q values. Top panel: $q = 1.01$ Å^{-1}, mid panel: $q = 1.42$ Å^{-1}, and bottom panel $q = 2.13$ Å^{-1}.

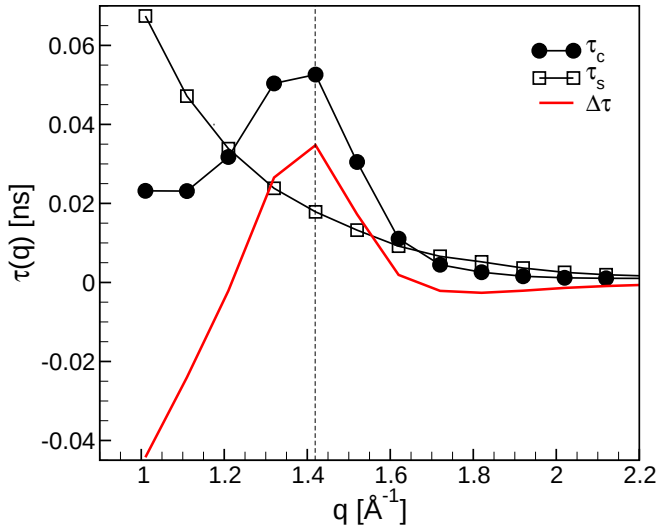

Figure 3.17: The relaxation or decay times τ_c (closed circles) and τ_s (open squares) as a function of wave-vector q. $\Delta\tau = \tau_c(q) - \tau_s(q)$ is depicted with red colored solid curve.

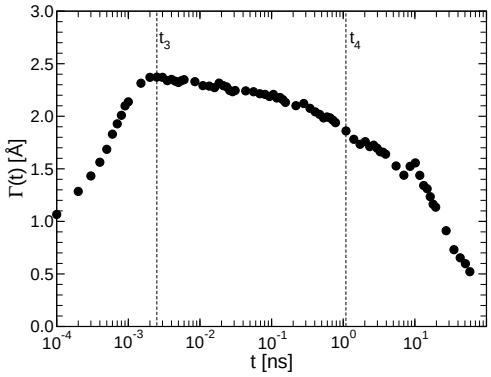

Figure 3.18: $\Gamma(t) = \int G(r,t)\mathrm{d}r$ as a function of time t. $\Gamma(t)$ measures the size of the correlated displacement at a time t.

there is indeed coherent dynamics between phospholipid tails along the lipid bilayer plane around the nearest neighbor distance corresponding to the DMPC lipid tails [4].

If the dynamics of the tails of DMPC molecules are indeed correlated then a perturbation affecting one of the lipid molecules should be transmitted coherently to its neighbors within a certain distance (i.e., the coherence length), and felt for a certain amount of time (i.e., the coherence time). To estimate the temporal and spatial range of the correlated dynamics exhibited by the lipid acyl chains, we define a spatial correlation function $g_\Delta(r,t)$ analogous to the pair correlation function $g_1(r)$ (commonly used to characterize the structure of any classical fluid). The expression of $g_\Delta(r,t)$ is

$$g_\Delta(r,t) \quad = \quad \frac{V}{\langle \Delta r \rangle^2 N} \times \sum_{n,m}{}' \langle \Delta r_n(t) \Delta r_m(t) \delta(r - |\vec{r}_n(0) - \vec{r}_m(0)|) \rangle,$$

where N indicates the total number of monomers present in a particular configuration (in our case N is the number of carbon atoms within lipid the tail), $\Delta r_n(t) = |\vec{r}_n(t) - \vec{r}_n(0)|$ represents the displacement of carbon atoms in the xy plane of the membrane, and the prime in $\sum_{n,m}$ denotes a restricted double sum in which carbon pairs (labeled with n and m indices) belonging to the same lipid tail are excluded. As customary for equilibrium MD simulations, the ensemble average $\langle .... \rangle$ is evaluated as time average along the MD trajec-

tory. $g_\Delta(r,t)$ measures the correlations of fluctuations of local displacements away from their average value $\langle \Delta r \rangle$. In the absence of displacement correlations, $g_\Delta(r,t) = g_1(r) = (V/N^2)\langle \sum_{n,m}{}' \delta(r + |\vec{r}_n - \vec{r}_m|)\rangle$, becomes the usual static pair correlation function.

In order to measure the total excess correlation of the in-plane displacements of the lipid tail carbon atoms between different lipids, we have computed a parameter, $\Gamma(t)$ [85]

$$\Gamma(t) = \int G(r,t)\mathrm{d}r = \int [g_\Delta(r,t)/g_1(r) - 1]\,\mathrm{d}r. \tag{3.19}$$

The time dependence of $\Gamma(t)$ is shown in Fig. 3.18. We find that $\Gamma(t)$ starts increasing from t = 0.1 ps and attains a maximum ($\sim$ 2.5 Å) at around 1 ps. From 1 ps to 1 ns, $\Gamma(t)$ decays rather slowly, having an average value of $\sim$2 Å. This observation implies that the spatial correlation of displacements of the lipid acyl tails is much stronger during the time intervals between 1 ps and 1 ns. After 1 ns, $\Gamma(t)$ starts decaying, but its value is greater than 1.0 until $\sim$ 10 ns. This result indicates that, the motion of the lipid tails are correlated for times in the range of 1 ps to 10 ns. It should be noted that, these times are much longer than the microscopic collision time but shorter than the time needed for a lipid to diffuse one lipid diameter (t $\geq$ 30 ns).

Finally, the spatial decay of $G(r,t)$ determines the length scale associated with the correlated displacements of lipid tails. The expression of $G(r,t)$ reads

$$G(r,t) = \frac{g_\Delta(r,t)}{g_1(r)} - 1. \tag{3.20}$$

Note that if the displacements of the phospholipid tails are spatially uncorrelated then $g_\Delta(r,t)$ and $g_1(r)$ would be identical for all r and hence $G(r,t) \approx 0$. It is the deviations of $g_\Delta(r,t)$ from $g_1(r)$ that describes the extra spatial displacement correlation beyond those expected from $g_1(r)$ only.

Shown in Fig. 3.19 is $G(r,t)$ versus r for $t_1 = 100$ fs (red solid curve), $t_2 = 10$ ns (red

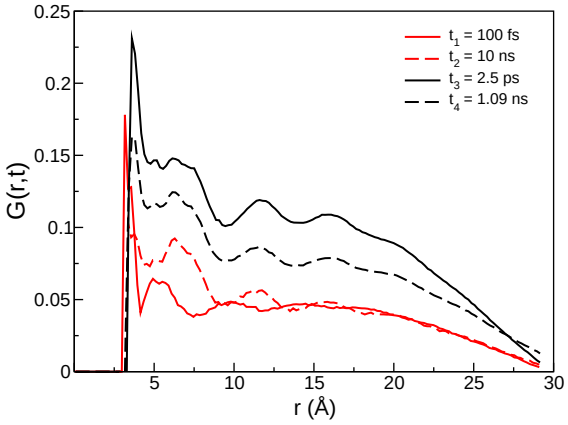

Figure 3.19: $G(r,t)$ vs r at different times, t_1 = 100 fs, t_2 = 2.5 ps, t_3 = 1.09 ns and t_4 = 10 ns. $G(r,t)$ measures the spatial range of the correlations.

dashed curve), $t_3 = 2.5$ ps (black solid curve) and $t_4 = 1.1$ ns (black dashed curve). t_1 and t_2 are taken from the times when $\Gamma(t)$ decreases sharply towards zero (Fig. 3.18, $\Gamma(t)|_{t_1}$ = 1.0 and $\Gamma(t)|_{t_2}$ = 1.5, respectively). One does not expect distinguishable spatial correlations at these times. The values of $G(r,t)$ are rather small ($G(r,t) \approx 0.05$) for $r > 4.4$ Å at both t_1 and t_2 times. Small $G(r,t)$ refers to the fact that, the displacements of the tails are less correlated at these times beyond the lipid tail nearest neighbor distance ($r = 2\pi/q \cong 4.4$Å). t_3 and t_4 are chosen from the time range where $\Gamma(t)$ has a high value ($\gtrsim 2$ Å) and at these times the phospholipid tails should be spatially correlated. Indeed, $G(r,t) \geq 0.1$ for t_3 as well as for t_4 (see Fig. 3.19) and it does not decay to zero until around 30 Å. The finite value of $G(r,t)$ indicates that, the values of $g_\Delta(r,t)$ is appreciably higher than $g_1(r)$ for $r \lesssim 30$ Å for these times. Consequently, the displacements of lipid tails are correlated for at least four to six lipid diameters between 1 ps and 1 ns.

3.8 Conclusions

Despite a vast literature on the experimental and computational studies of the dynamics of lipid bilayers, the determination of lateral self-diffusion coefficient D of lipid molecules is

still a controversial problem. The results for D seem to depend significantly on the time and length scales probed by the employed experiment or computer simulation method. Currently used models for estimating D, e.g., from NS experiments, do not take into account properly the fact that lipid molecules are polymers, characterized by flexibility and connectivity. Hence, their lateral diffusion in the leaflets of lipid bilayers are different from the diffusion of molecules in dense fluids. This difference is observed in the time evolution of the lateral MSD. Unlike dense simple fluids, the MSD of lipid atoms and molecules exhibits a broad sub-diffusive region (from 1 ps to 10 ns), which connects the short time ballistic regime and the long time linear diffusion regimes.

Here we have developed a phenomenological memory function model which can be applied to describe the behavior of the MSD for all the lipid atoms and molecules over the entire time range extending from the ballistic regime to the linear diffusion regime. By fitting the MSD from MD simulation with the MSD from our MF-based theoretical model, we are able to identify three distinct time scales that correspond to three dynamic domains in the lipid bilayer system. Overall, our theoretical model can reproduce the time dependence of the MSD of various lipid atoms and molecules with great accuracy over nine orders of magnitude of time. Using our memory function approach (Eq. 3.7), one can also determine the lateral self diffusion coefficient of lipid atoms and molecules. The calculated D is found to be within 30% of the diffusion coefficient measured in FRAP experiments. Note that, similar D obtained for all the atoms and molecules implies that, while dynamics of all the lipid atoms are significantly different at ps timescale, their motion at $t > 30$ ns is best described by simple diffusion.

We have also studied the consequence of the sub-diffusive behavior of the MSD by calculating the first two terms in the cumulant expansion of IISF. The first term is known as the Gaussian approximation and is exact when the probability distribution $P(r,t)$ of the displacements is Gaussian in space. By calculating the first non-Gaussian correction, we have found that $P(r,t)$ is Gaussian in the ballistic and linear diffusion regions. For the P

atoms and the center of mass of individual lipid molecules, the Gaussian approximation also holds in the sub-diffusive domain. However, the Gaussian approximation fails for carbon and hydrogen atoms in the sub-diffusive regime.

We have pointed out that in typical neutron scattering experiments one probes the dynamics of a lipid bilayer in the sub-diffusive regime instead of the linear diffusion one. Thus the proper analysis of the experimental NS data requires theoretical models that can describe the sub-diffusive dynamics of lipid atoms and molecules, such as the MF approach proposed by us.

We have shown that the analysis of NS data assuming erroneously that the probed lipid bilayer is in the linear diffusive regime results in an overestimated diffusion coefficient that is strongly q and ω dependent. By employing our MF approach we have developed a computational method for determining the correct D from the incoherent dynamic structure factor measured in NS experiments. It is quite remarkable that through this method one can determine D without input from the linear diffusive regime. The key is to treat properly the sub-diffusive regime, which is probed in the NS experiment.

While studying the correlated dynamics of the lipid tails in the fluid phase of phospholipid bilayer, we have established that a correlated structural relaxation exists between the DMPC lipid tails around their nearest neighbor distance ($q = 1.42$ Å^{-1}). Also, the displacements of the lipid tails are correlated up to four to six lipid diameters for times ranging from $\sim$1 ps to $\sim$10 ns.

4 Anomalous diffusion of water molecules in hydrated lipid bilayers

4.1 Introduction

Waters at the surface of lipid membranes are fundamental for their structural stability and functioning [86, 87]. The water molecules residing in the vicinity of biological membrane surfaces, micelles and other biological macromolecules are known as hydration waters. They are translationally restrained due to their attachment to neighboring biomolecules and exhibit slower dynamics than that of bulk waters [87–90]. Being farther away from the surface of biomolecules, bulk waters experience weak or moderate interaction and exhibit unrestricted translational and rotational motion [86, 90].

The research concerning the hydration water at the surface of cellular membranes has two broad branches: (i) structure and dynamics of hydration waters, and (ii) the influence of solvent environment on the structure, dynamics and function of phospholipid membranes. The structural properties of model membranes and hydration waters were studied using neutron scattering and X-Ray scattering techniques [91]. NMR spectroscopy [92–95], time resolved fluorescence spectroscopy [96–98], neutron scattering technique [94, 99, 100], ultra-fast vibrational spectroscopy and infra-red (IR) absorption spectroscopy [101] were employed to investigate the structure and dynamics of hydration waters at the surface of a variety of biomolecules (e.g. peptides, reverse micelles, proteins, phospholipid bilayer etc.). Computer simulation techniques e.g., molecular dynamics simulation, Monte Carlo simulations were also employed to explore the structural and dynamical properties of the hydration waters at the surface of model membranes and reverse micelles [100, 102–108]. The hydrogen bonding pattern between water and lipid headgroups, orientational distribution and electrostatic potential of interfacial waters at the surface of lipid membranes were studied by several groups and are summarized in several review articles [109–111].

In addition to in-plane self diffusion and coherent dynamics (see Chp.3), lipid molecules (in the fluid phase of bilayers) also exhibit considerable vertical, out-of-plane fluctuations. As the water molecules at the surface of solvated membranes locally interact with

their neighboring lipids, the dynamics of water molecules and membrane molecules are to some degree correlated. Despite previous experimental and computational studies of water-membrane dynamics, little is known about the time and length scales of these correlations. In this project, by employing a 0.1 μs MD simulation of a DMPC lipid bilayer, we show that, the waters in a hydrated lipid bilayer can be classified into four dynamically connected water layers. We present a detailed analysis of the water dynamics within these four regions. We also show that, there exists a cooperative molecular motion between the hydration waters and the DMPC lipid molecules. The time and length scales of this correlated dynamics are also determined.

4.2 MD simulation

To investigate the dynamics of water molecules in a hydrated lipid membrane, we have used the 0.1 μs long all atom MD simulation of a fully solvated DMPC lipid bilayer (Fig. 4.5) described in Chapter 3 (Sec. 3.2).

4.3 Classification of water molecules in a hydrated DMPC bilayer

It is well known that the waters at the surface of phospholipid bilayers have very different dynamics depending on their proximity with the phospholipid headgroup atoms. The distribution of water along the perpendicular to the plane of the membrane (z-axis) is highly inhomogeneous. The water mass density $\rho(z)$ increases from zero at the middle of the membrane to its bulk value far away from the surface of the membrane. Intuitively one can classify the waters into four distinct but connected regions. Buried waters (region R-1) are situated inside the membrane, underneath the lipid headgroups. Hydration waters (region R-2) surround the hydrophilic lipid headgroups. Bulk waters (region R-4) are sit-

uated sufficiently far away from the surface of the membrane so that their properties are essentially indistinguishable from true bulk water. Finally, intermediate waters (region R-3) are situated between R-2 and R-4 waters. A precise definition of these four water regions is essential for proper description of the dynamics of water molecules as a result of their interaction with the lipid membrane.

4.3.1 Water regions for static plane membrane surface

If one assumes that the surface of the membrane is smooth, i.e., the lipid headgroups are all located in the same, horizontal plane (*xy*-plane) then one can define the four water regions based on the profile of $\rho(z)$, where z is the z-coordinate of the water O atom measured from the CM of the entire lipid bilayer (located at the middle of the membrane). $\rho(z)$ calculated from our MD simulation data is shown in Fig. 4.1, lower panel. In this situation it is practical to divide the 12 Å thick water layers on both sides of the membrane into 6 even sub-layers (L1,...,L6 in the lower panel of Fig. 4.1), with a width of 2 Å each. Then, R-1 would correspond to waters below the plane of the headgroups. R-2 would consist of L1-L2 (i.e., first-second hydration layers). Finally, R-3 and R-4 would be defined by L3-L4 and L5-L6, respectively. Unfortunately, this simple classification of water molecules is not appropriate. The main reason is that on the relevant ns and sub ns time scale the lipid headgroups undergo substantial vertical (z-axis) fluctuations. Thus the key assumption that they rest in a static, well defined horizontal plane is false (see Fig. 4.1, top panel). Thus, our inability to properly locate the polar lipid headgroups in the above scheme makes the proposed classification of waters meaningless. Indeed, as illustrated in the inset to Fig. 4.1, due to the uneven vertical displacement of the lipids (due to membrane surface fluctuations) most often the water layers L1,...,L6 can contain more than one type of water (i.e., buried, hydration, bulk and intermediate). It should be mentioned, however, that in spite of the z-axis fluctuations of the lipid molecules, the the long time average ($>$10 ns) of their headgroup's CM position yield a very well defined horizontal plane, i.e., the

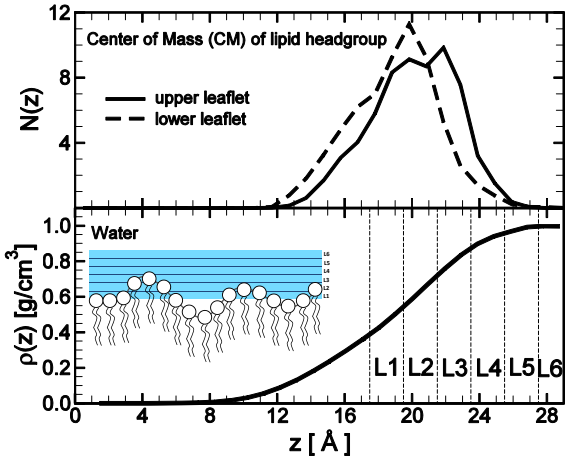

Figure 4.1: Lipid headgroup distribution (top) and water mass density variation (bottom) along the z-axis (with origin at the CM of the DMPC membrane and oriented normal to the plane of the membrane). Inset: schematics of the water layer arrangement at the surface of the DMPC bilayer.

membrane plane.

4.3.2 Out-of-plane fluctuations of lipid molecules

To gain more insight into the out-of-plane fluctuations of the lipids we have followed the time evolution $z_{CM}(t)$ of the CM of the lipid headgroups by using our MD simulation results. The obtained results are shown in Fig. 4.2. The circles represent the mean values ($\langle z \rangle \sim 19.5$ Å) and the error bars are standard deviations ($\sigma \sim 2.6$ Å).

we have also calculated $\Delta z_i = z_i(t) - \langle z_i \rangle$ for each DMPC lipid. The histograms of Δz_i for three representative lipids (L-54, L-39, L-124) are depicted in the top panel of Fig. 4.3. We have chosen these three examples because they show remarkably different dynamics as it can be seen in Fig. 4.3. L-124 has $\langle z \rangle$ = 19.6 Å and a small σ = 0.89 Å. For L-54, $\langle z \rangle$ = 17.3 Å and σ = 2.65 Å is large. For L-39 $\langle z \rangle$ = 19.6 Å and σ = 1.53 Å, respectively. Thus, during the 10 ns time interval, the CM of the headgroups of these three lipids occupy slightly different mean vertical positions and have noticeably different vertical fluctuations amplitudes characterized by different σ values. The time evolution of

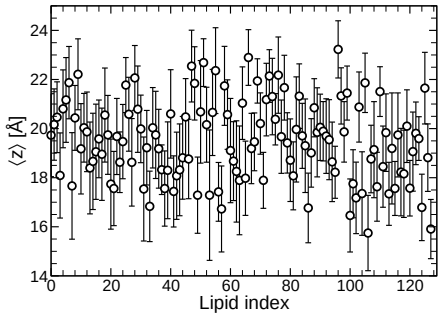

Figure 4.2: Mean z-coordinates (circles) of the 128 lipid headgroups determined from the 0.1μs MD simulation. Error bars represent standard deviation.

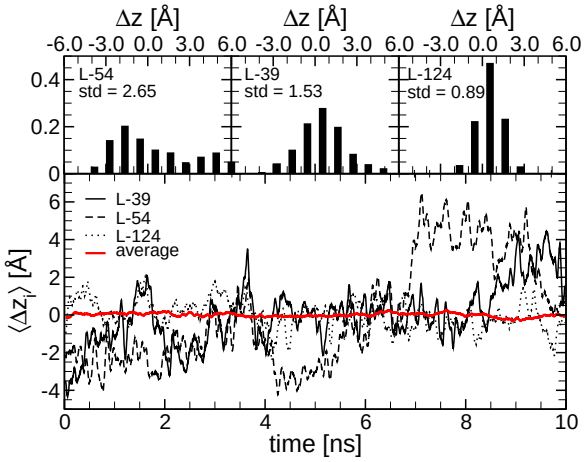

Figure 4.3: Distribution of Δz (top) and $\Delta z_i(t)$ (bottom) for three lipids L-39, L-54 and L-124. The red horizontal curve represents $\langle \Delta z(t) \rangle$ averaged over all the lipid molecules.

these vertical positions fluctuations are shown in Fig. 4.3, bottom panel. The red horizontal curve represents the mean z_{CM} position averaged over all the lipid molecules. This result clearly shows that in spite of the significant z-axis fluctuations of individual lipids, the common z_{CM} comprising all lipid headgroups has (almost) the same value at any instant of time. In other words, the notion of plane lipid membrane surface is well defined except for the proper classification of water molecules.

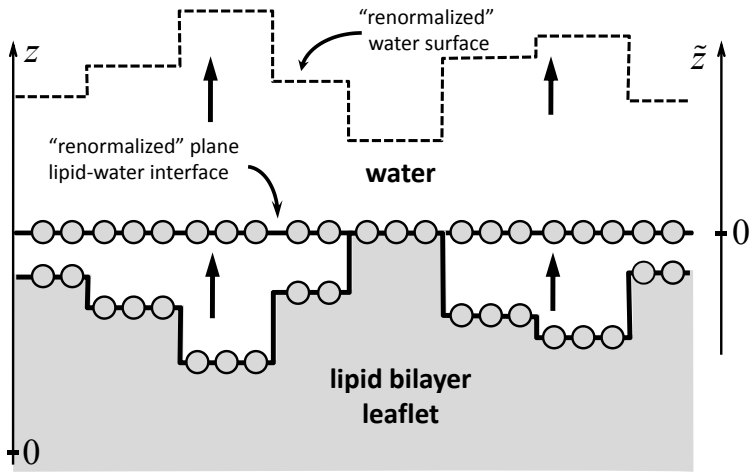

Figure 4.4: Schematic diagram showing the redefined lipid-water surface using the Voronoi tessellation algorithm.

4.3.3 Water regions for fluctuating membrane surfaces

A more realistic identification of the four water regions R-1,...,R-4, valid for lipid membranes with local fluctuations, can be achieved by employing a Voronoi tessellation approach [87, 90]. In the Voronoi tessellation method [87, 90], the plane of the lipid bilayer is redefined by treating the surface as an assembly of patches (Fig. 4.4). An approximate surface is formed by projecting the CMs of DMPC headgroups on a plane at $\tilde{z} = 0$, where the CMs are the centers of the Voronoi polygons. A schematic diagram of the 2D model based on Voronoi tessellation analytic method is shown in Fig. 4.4. Note that, the Voronoi tessellation of a set of points on a 2D surface can be divided into convex, space filling polygons (called Voronoi simplices) [112].

The local density distribution of waters $\rho(\tilde{z})$ at the phospholipid-water interface is calculated using the following steps. First, the lateral distance, $r^{wc} = \sqrt{(x^w - x^c)^2 + (y^w - y^c)^2}$, between the water oxygens (superscript w) and the CMs of each lipid headgroups (superscript c) is calculated. Then, each water molecule is assigned to the unique Voronoi simplex corresponding to the smallest r^{wc}. Then, the corresponding new effective z-coordinate, $\tilde{z}$, is determined as $\tilde{z} = z^w - z^c$. Next, the obtained $\tilde{z}$ values are binned with a binsize of $\delta\tilde{z}$

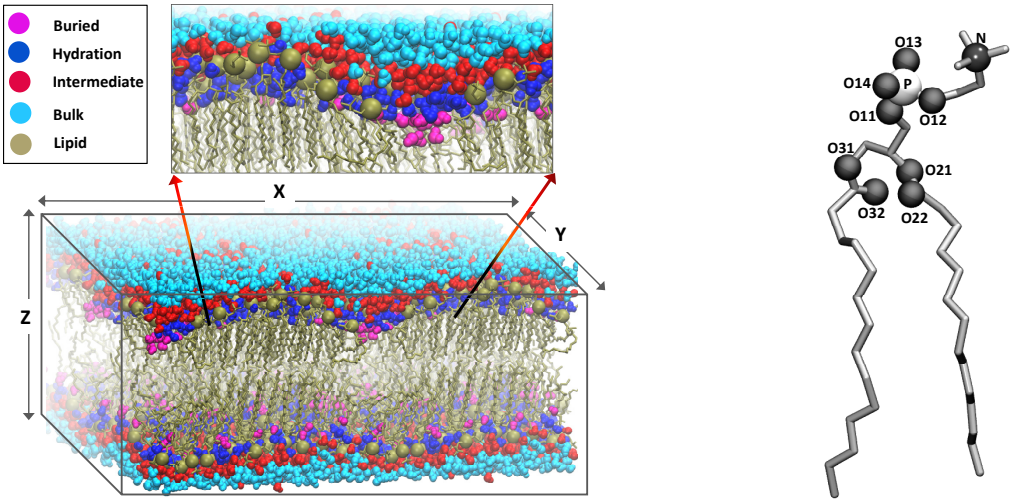

Figure 4.5: Left panel: the simulated hydrated DMPC lipid bilayer system. The four dynamically connected waters are color coded: magenta for buried-waters (R-1), blue for hydration-waters (R-2), red for intermediate waters (R-3) and cyan for bulk-waters (R-4). The waters are shown in VDW representation. Lipid molecules are shown in line representation. P atoms are shown as green VDW spheres. Right panel: DMPC molecule with the carboxylic oxygens (O13, O14, O22 and O32) and ether oxygens (O11, O12, O21 and O31). The phosphorus(P) and nitrogen (N) atoms are highlighted as VDW spheres. The lipid carbons are shown in licorice representation. These figures were created using VMD[1].

= 0.25 Å. The total number of water oxygens $N_n^w(\tilde{z})$ is counted in each bin n. Finally, the new effective local mass density distribution $\rho(\tilde{z})$ is evaluated using the formula

$$\rho(\tilde{z}) = m_w \frac{N_n^w(\tilde{z})}{APL \times N_L \times \delta\tilde{z}}. \tag{4.1}$$

Here m_w is the mass of one water molecule, the APL of the lipid bilayer system is 60.06 Å^2 and N_L is the number of unique Voronoi simplexes associated with the water molecules (N_n^w) in any given bin, n. The obtained mass density distribution $\rho(\tilde{z})$ is shown in Fig. 4.6. The waters in the bilayer system has been classified into four regions based on the $\rho(\tilde{z})$ profile. Waters with $\tilde{z} \leqslant$ -4.0 Å are R-1 buried waters. Hydration (R-2) waters are defined by the water molecules with $-4.0 \leqslant \tilde{z} < 1.0$ Å. The water molecules with $1.0 \leqslant \tilde{z} < 5.0$ Å are intermediate (R-3) waters. Finally, water molecules with $\tilde{z} \geqslant 5.0$ Å are identified as

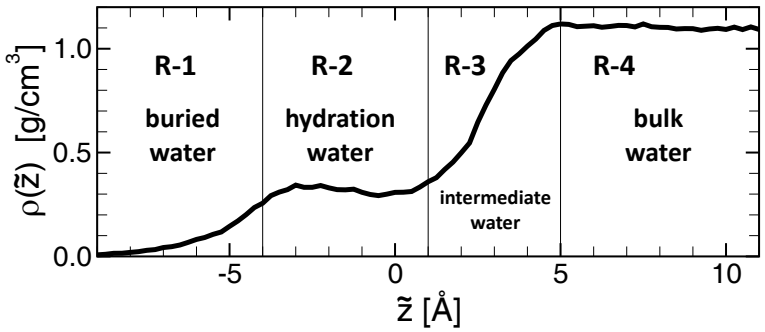

Figure 4.6: Water mass density $\rho(\tilde{z})$ as a function of $\tilde{z}$. The four regions R-1, ..., R-4 identified in the figure contain 3.8%, 16.8%, 30.9% and 48.5% of the total water, respectively.

bulk (R-4) waters. At $\tilde{z} = 5$Å $\rho(\tilde{z})$ reaches a saturation value ≈ 1.1 g/cm^3, which is slightly bigger than the usual bulk water density. This discrepancy is most likely due to the fact that the area calculated with the Voronoi method slightly underestimate the area of the system. The classification of water used by us is consistent with other similar methods used in the literature [87, 88, 90, 113]. The amount of water contained in the four distinct regions is quite uneven. The percentage of buried water is only 3.8. The percentage of hydration, intermediate and bulk waters are 16.8, 30.9 and 48.5, respectively. A snapshot of the hydrated bilayer is displayed in the left panel of Fig. 4.5.

4.4 Mean square displacement

To gain insight into the dynamics of in the four regions R-1,.....,R-4, we have investigated the time dependence of their lateral mean squared displacement (MSD)

$$\langle [\delta r(t)]^2 \rangle = \langle | \, (r(t) - r(0))^2 \, | \rangle. \tag{4.2}$$

Here $r(t)$ is the projection of the actual position vector of the considered atom in the xy-plane of the membrane at time t. Just like in the case of lipid molecules, we have also

calculated the corresponding logarithmic derivative of the MSD, $\alpha(t)$

$$\alpha(t) = \frac{\partial \ln[\langle[\delta r(t)]^2\rangle]}{\partial \ln(t)}. \tag{4.3}$$

One should recall that in the ballistic regime $\alpha(t)$ = 2, in the linear regime $\alpha(t)$ = 1 and in the sub-diffusive (super-diffusive) regime $\alpha(t) = \beta \approx$ const., with $\beta < 1$ ($\beta > 1$).

The obtained results are shown in Fig. 4.7. The time evolution of the lateral MSD is shown in the top panel, while the lower panel shows the time dependence of $\alpha(t)$ for all four water regions. The MSD for the R-1, R-2, R-3 and R-4 waters show the same ballistic regimes with $\langle[\delta r(t)]^2\rangle \sim t^2$ and $\alpha(t)$=2 for $t < 10$ fs. In addition to the ballistic region, the MSD of R-1 and R-2 waters exhibit three distinct dynamical regimes: (1) sub-diffusive, for 0.2 ps $<$ t $<$ 20 ps, with $\alpha(t)$ <1; (2) super-diffusive, for 0.1 ns $<$ t $<$ 1 ns, with 1$<\alpha(t)<$2; and (3) Fickian diffusion, for t $>$ 10 ns, with $\alpha(t)$ = 1. In the case of R-3 and R-4 waters, the Fickian diffusion regime is also present for t $>$ 20 ps. A weak super-diffusive regime can also be seen for R-3 waters. The anomalous (sub- and super-) diffusive domains are almost non-existent for bulk (R-4) waters. Not surprisingly the MSD for all the waters (Fig. 4.7, red curve) almost coincides with that for the bulk R-4 waters. This is due to the fact that the majority of the waters in the system are bulk waters.

The origin of the sub-diffusive regime in the MSD of the buried and hydration waters can be explained in terms of the interactions between water and lipid molecules. Water molecules are polar and they get attached to the phospholipid headgroups in their vicinity via hydrogen bonds. Consequently, the R-1 and R-2 waters closely follow the dynamics of headgroup atoms up to tens of picoseconds (average H-bond life time $\sim$ 0.05 ns, see Sec. 4.5), thus their motion is slowed down compared to bulk waters. The MSD of P atoms also exhibits the sub-diffusive dynamics in the time range 1 ps $< t <$ 10 ns with $\alpha(t) = \beta \approx 0.6$. Unlike lipid atoms (e.g., P), however, buried and hydration waters also show super-diffusive motion after $t > 0.1$ ns. The source of super-diffusive dynamics in

the sub-nanosecond time scale in case of buried and hydration waters will be discussed in Sec. 4.5.

The crossover to the linear diffusion regime for R-1 and R-2 waters begins around ~ 10 ns just like for the R-3 and R-4 waters. This implies that after a sufficiently long time all the waters execute linear diffusion characterized by a lateral (xy-plane) diffusion coefficient

$$D = \lim_{t\to\infty} \langle [\delta r(t)]^2 \rangle / 4t. \tag{4.4}$$

From the MD simulation data one obtains $D = 2.65 \times 10^{-5}$ cm^2/s $\cong D_{bulk}$. This finding agrees well with previously published results [88, 114, 115]. The diffusion coefficient D of bound waters obtained in previous simulations are 8 [88] to 10 [89] times smaller than the bulk water diffusion coefficient D_{bulk}. This discrepancy originates from the fact that, in previous studies, the diffusion coefficient for hydration waters are obtained from the MSD in the sub-diffusive regions ($t < 20$ ps) instead of the linear diffusion regime.

4.5 Hydrogen bond analysis

The static and dynamic properties of hydrogen bonding between water and phospholipids in hydrated bilayers has served as a key quantity in many experiments and simulations thereby describing the special features of hydration waters as compared to the free waters. In Sec. 4.4, it was shown that the sub-diffusive and the super-diffusive dynamics characteristic to buried (R-1) and hydration (R-2) waters are absent in the case of intermediate (R-3) and bulk (R-4) waters. The qualitatively different dynamical behavior of the buried and hydration waters is due to their direct contact and, therefore, ability to form hydrogen bonds with the polar lipid headgroups. In order to gain further insight into the distinct dynamical properties of the four different types of water regions in the hydrated DMPC system, we have studied the statistics and the dynamics of the hydrogen bonding between water-lipid

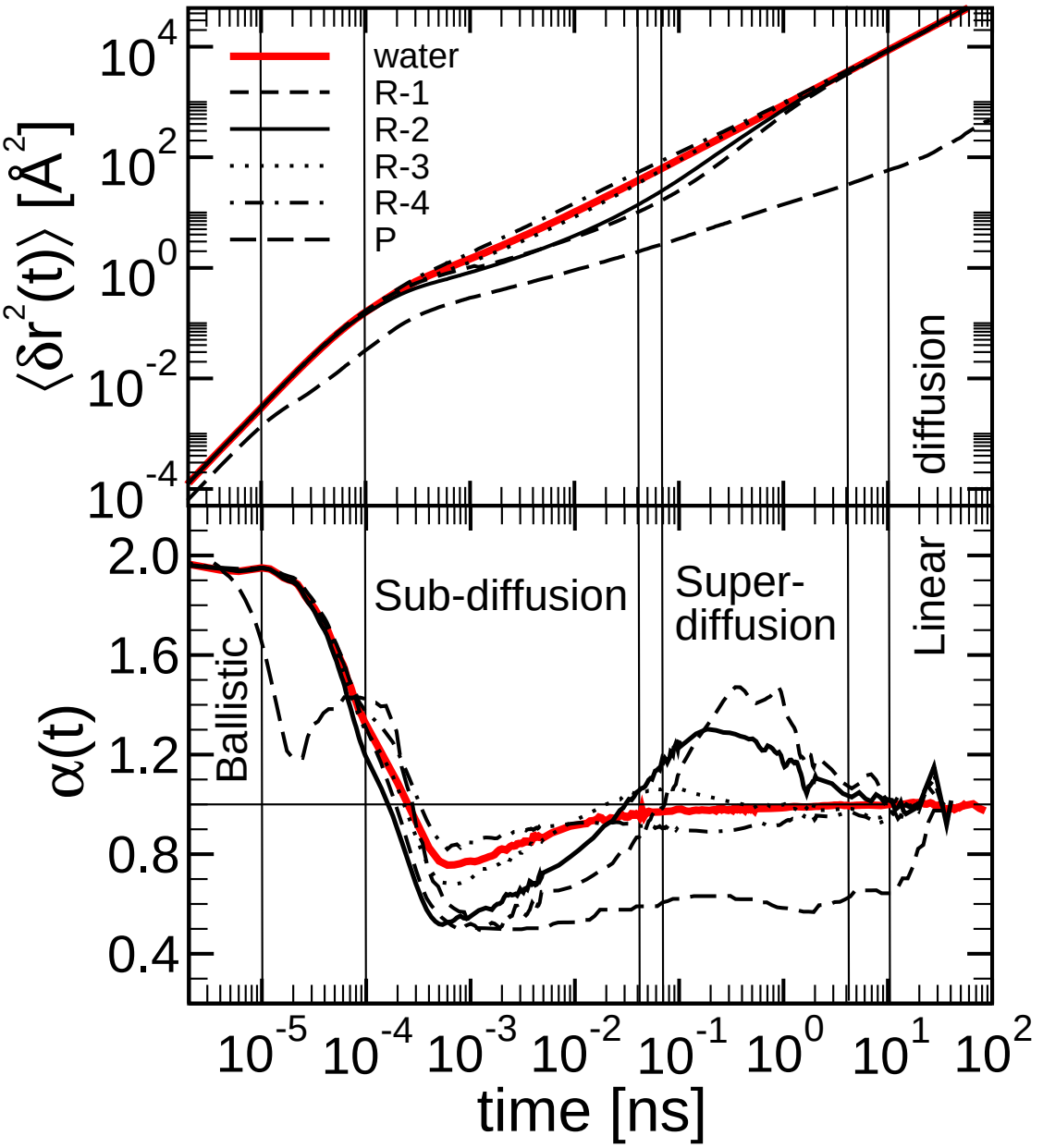

Figure 4.7: Lateral MSD (top) and corresponding logarithmic slope (bottom) of water molecules from regions R-1, R-2, R-3 and R-4 (identified as buried, hydration, intermediate and bulk waters, respectively). Same quantities for all the water molecules and the phosphorus (P) atoms in the DMPC headgroups are also shown.

and water-water molecules.

In a hydrogen (H-) bond an electropositive hydrogen atom is shared between two electronegative atoms, e.g., the oxygens in two water molecules. It is widely accepted that a H-bond is present when the oxygen-oxygen (O....O) distance is less than 3.25 Å, and an angle between O....O and the corresponding O-H bond is less than 35° [116–118]. Using this geometrical definition of a H-bond, we have calculated the number of H-bonds between eight lipid oxygen atoms (shown in the right panel of Fig. 4.5) and water molecules along the entire MD trajectory. The likeliness (relative probability) that a particular H-bond is formed has been estimated by dividing the number of MD trajectory frames with the H-bond present to the total number of frames. The results, expressed in percentage are shown in Fig. 4.8. There are four carboxylic oxygens (O13 and O14 in the headgroup and O22 and O32 in the lipid tail) and four ether oxygen atoms (O11, O12 and O21 and O31). As shown in Fig. 4.8, carboxylic oxygen atoms are more likely to form a hydrogen bond than the ether oxygen atoms, while the O21 and O31 in the lipid tail are the least likely to form H bonds. O11, O12, O13 and O14 in the headgroup will, on average, be in contact with more water molecules. O11 and O12 form H-bonds $\sim$30% of the time. O11 and O12 atoms are involved simultaneously in two H-bonds only 1% of the time compared to 61% in the case of O13 and O14 atoms. The difference in the probabilities is due to the different environment experienced by the individual oxygen atom. In case of the tail oxygen atoms (O22 and O32), we find that the probability of formation of one H bond is 50%. The probability of formation of two H bonds with O22 and O32 is almost negligible due to their inaccessibility by water molecules. Clearly, most lipid-water H-bonds involve the headgroup oxygens O13 and O14 which are the most accessible to the hydration water molecules. Some H bonds also exist between the waters and the O11, O12, O22 and O32 atoms. The buried and hydration waters interact with the lipid molecules via these H bonds. Consequently, their dynamics is strongly affected by the dynamics of the lipids.

To determine the time scale at which the dynamics of R-1 and R-2 waters is correlated

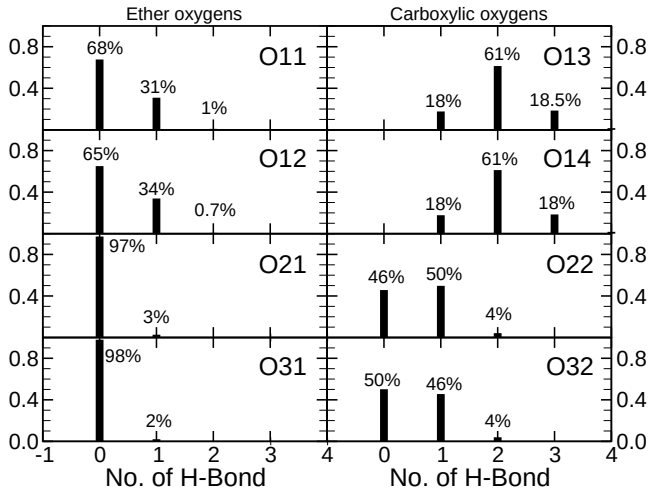

Figure 4.8: Probabilities of forming various numbers of hydrogen bonds (1, 2 and 3) between lipid oxygens and water molecules. The different lipid oxygen atoms are shown in Fig. 4.5.

with the phospholipid molecules, we have studied the hydrogen bond correlation function [118, 119]

$$\sigma(t) = \frac{\langle h(t)h(0)\rangle}{\langle h^2\rangle}, \tag{4.5}$$

where $h = h(0)$ is the number of H-bonds at t = 0, and $h(t)$ is the number of H-bonds that still persist at time t. Figure 4.9 shows $\sigma(t)$ for the H-bonds formed by lipids with water molecules in R-1, R-2, R-3 and R-4 regions. The $\sigma(t)$ function decays much slower for R-1 and R-2 waters indicating that these are more likely to form H-bonds with the phospholipid molecules.

Next, from the decay of the correlation function $\sigma(t)$, we have estimated the characteristic lifetime of the corresponding H-bonds. Note that, the $\sigma(t)$ curves in Fig. 4.9 cannot be fitted with a single or double exponential. Thus, characteristic lifetime τ can be defined through the equation: $\sigma(\tau)/\sigma(0) = 1/e$. The corresponding H-bond lifetimes are τ_1 = 0.1 ns, τ_2 = 0.06 ns, τ_3 = 0.03 ns and τ_4 = 0.02 ns, respectively. As expected, the H-bonds formed by buried and hydrations waters with the lipid molecules have a longer lifetime than those involving intermediate and bulk waters.

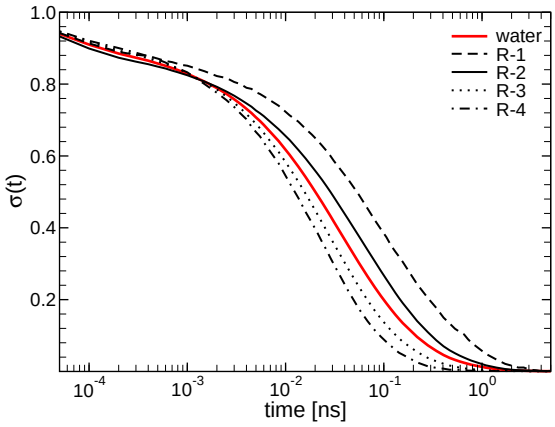

Figure 4.9: $\sigma(t)$ for H-bonds between PO_4 oxygens and waters from regions R-1, R-2, R-3 and R-4. The red curve corresponds to all waters, regardless of their localization.

The stronger H-bonding between lipids and R-1,R-2 waters implies that, on a time scale shorter than the mean lifetime of the H-bonds, the dynamics of the latter should be correlated with the motion of the lipid headgroups. Indeed, in Fig. 4.7, the MSD of the R-1, R-2 waters and that of the P atoms are rather similar for $t \lesssim 20$ ps. At the same time, the characteristic H-bond lifetimes $\tau_{1,2} \sim 0.1$ ns coincide with the crossover time to the superdiffusion regime in the MSD of R-1 and R-2 waters. For $t > \tau_1$, waters initially in the R-1 and/or R-2 regions diffuse out, along the z-axis, into the intermediate/bulk regions where their lateral diffusion (in the xy-plane) is enhanced. The latter is reflected in the super-diffusion behavior of the lateral MSD.

4.6 Time evolution of water mass density profile

As already mentioned, the four water regions R-1, ..., R-4 are dynamically connected, i.e., waters continuously diffuses from one region to another. To estimate the characteristic time scale of this dynamic process we have followed the relaxation of the mass density profile in each water region. This can be accomplished by following the time evolution of the density of the water molecules that at an initial time $t = 0$ belongs to one particular region. Thus, at

t = 0, $\rho_i(\tilde{z};t=0)$ coincides with the equilibrium $\rho(\tilde{z})$ in the considered region i=1,...4, and it is zero in the other three regions. With time, this non-equilibrium density profile relaxes towards the equilibrium one (up to a multiplicative constant). Clearly, the spreading of $\rho_i(\tilde{z};t)$ outside of region i signifies the water exchange between the different regions. Using our MD trajectory data, we have calculated $\rho_i(\tilde{z};t)$ for all four water regions at t = 1 ps, 10 ps, 0.1 ns, 0.5 ns and 1 ns. The results are shown in Fig. 4.10. Mass conservation dictates that an any time t, $\sum_{i=1}^{4}\rho_i(\tilde{z};t)=\rho(\tilde{z})$, the equilibrium mass density (red curve in Fig. 4.10). From the plots in Fig. 4.10 one can infer that the sought characteristic density relaxation time $\tau_R^w \sim 0.5$ ns. It takes about this amount of time to restore equilibrium following a density perturbation. Not surprisingly, τ_R^w has the same order of magnitude as $\tau_{1,2}$, the characteristic H-bond relaxation time for the bound and hydration waters. Indeed, any water exchange between regions including R-1 and R-2 may not occur on a time scale shorter than the mean lifetime of the corresponding H-bonds with lipid headgroups.

4.7 z-axis relaxation of phospholipids

It has been shown in Sec. 4.3.2 that DMPC lipid molecules exhibit noticeable vertical (i.e., z-axis) fluctuations. In order to quantitatively characterize these fluctuations we have calculated the time autocorrelation function $C(t)=\langle\Delta z(t)\Delta z(0)\rangle$ of the z-axis displacements $\Delta z(t)$ of the CM of the lipid headgroups. Using our MD trajectory data, $C(t)$ at a discrete time t_l is computed as

$$\begin{aligned} C(t_l) &= \langle\Delta z(t)\Delta z(0)\rangle \\ &= \frac{1}{N_{cm}}\sum_{i=1}^{N_{cm}}\left[\frac{1}{N_t-l}\sum_{k=1}^{N_t-l}\Delta z_i(t_l+t_k)\Delta z_i(t_k)\right], \end{aligned} \tag{4.6}$$

where N_t-l is the number of time origins, N_{cm} is the number of lipid molecules, and $\Delta z_i(t)$ is the z-axis displacement of the CM of the headgroup of lipid "i" at time t. The normalized

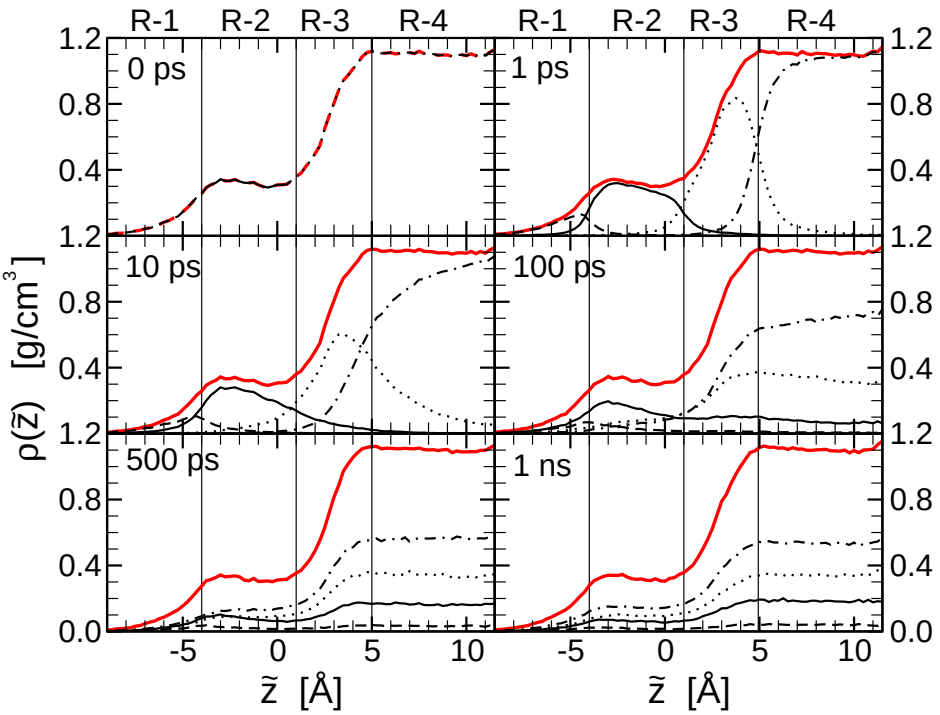

Figure 4.10: Water mass density profile $\rho_i(\tilde{z};t)$ at different times for the four dynamically connected water layers R-1 (dashed curve), R-2 (solid curve), R-3 (dotted curve) and R-4 (dot-dashed curve). Red solid curve represents the equilibrium $\rho(\tilde{z})$.

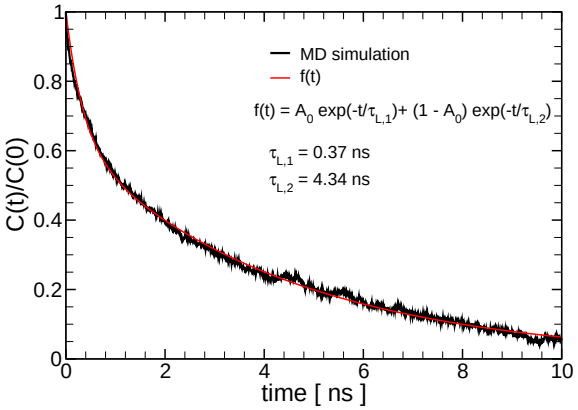

Figure 4.11: Time autocorrelation function C(t)=$\langle \Delta z(t) \Delta z(0) \rangle$ of the vertical (z-axis) displacements of the CM of lipid headgroups.

autocorrelation function $C(t)/C(0)$ is plotted in Figure 4.11. This function can be well fitted with a double exponential as shown in Fig. 4.11 (red curve). The two characteristic time constants are $\tau_{L,1} \approx 0.4$ ns and $\tau_{L,2} \approx 4.3$ ns. Clearly, $\tau_{L,1}$ has the same magnitude as the mean lifetime $\tau_{1,2}$ of the lipid-water H-bonds (see Sec. 4.5) and the water mass density relaxation time τ_R^w of the R-1 and R-2 waters (see Sec. 4.6). These finding provide clear evidence that the z-axis dynamics of lipids and of the bound (R-1) and hydration (R-2) waters are correlated on a sub ns time scale.

4.8 Incoherent scattering functions

Similarly to lipids (Chp.3), the anomalous diffusion of water molecules at the lipid-water interface should lead to characteristic features in the incoherent intermediate scattering function (IISF) and in the corresponding dynamics structure factor (DSF) measured in NS experiments. However, because the fraction of the bound (R-1) and hydration (R-2) waters is rather small (see Fig. 4.6) their contribution to the DSF may be very difficult to observe experimentally. Here we use our 0.1μs long MD simulation to investigate the IISF of waters in our hydrated DMPC system. The following analysis is rather similar to the one for the lipid molecules presented in Chp.3. IISF, $I_s(q,t)$, is given by

$$I_s(q,t) = \frac{1}{N_{WL}} \left\langle \sum_{m=1}^{N_{WL}} e^{i\vec{q}\cdot[\vec{r}_m(0)-\vec{r}_m(t)]} \right\rangle, \tag{4.7}$$

where the summation goes over all the water molecules N_{WL} within a given region (e.g., R-1, R-2, R-3 or R-4) of the phospholipid bilayer system. $\vec{r}_m(t)$ is the position vector of the m^{th} atom at a given time t, and q is the scattering wave vector in the xy-plane.

IISF corresponding to the four different water layers for q = 0.01, 0.05, 0.1, 0.5, 1.01 and 1.63 Å^{-1} are shown in Fig. 4.12. For small q values, e.g., q = 0.01 Å^{-1}, $I_s(q,t)$ for each of the four water layers are similar. Starting from 0.05 Å^{-1}, however, the difference between the $I_s(q,t)$ corresponding to the R-1, R-2, R-3 and R-4 waters increases gradually

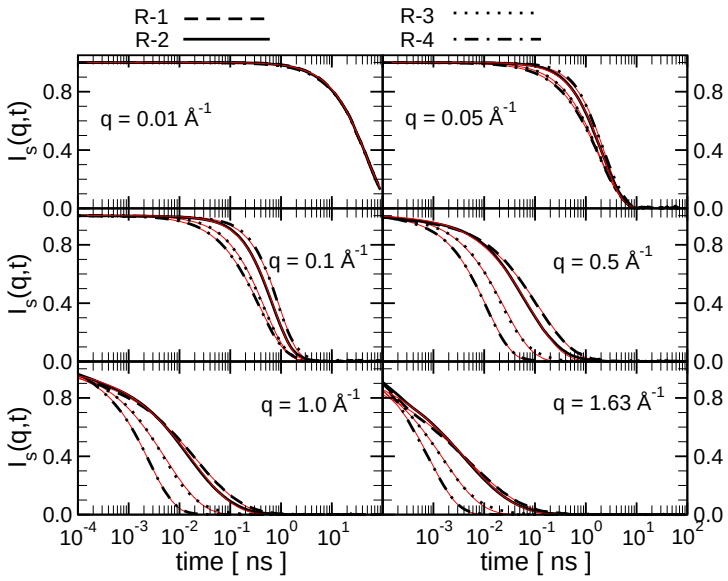

Figure 4.12: Incoherent scattering function $I_s(q,t)$ for water oxygen atoms located in the water regions R-1, R-2, R-3 and R-4 for q = 0.01, 0.05, 0.1, 0.5, 1.01 and 1.63 Å^{-1}.

as we move towards larger q values (smaller length scales). It is clear that, at bigger q values, the rate of decay of the incoherent scattering functions for R-1 and R-2 waters is slower than for the R-3 and R-4 waters. In general, $I_s(q,t)$ can be fitted either with a stretched or compressed exponential or with the corresponding Gaussian (i.e., second cumulant) approximation (with or without a non-Gaussian correction), expressed in terms of the MSD (see Chp.3), i.e.,

$$I_s(q,t) \approx \exp\left(-q^2 \frac{\langle[\delta r(t)]^2\rangle}{4}\right) \times \left[1 + \frac{1}{2}\left(\frac{q^2\langle[\delta r(t)]^2\rangle}{4}\right)^2 \gamma(t)\right], \tag{4.8}$$

with

$$\gamma(t) = \frac{\langle[\delta r(t)]^4\rangle}{2\langle[\delta r(t)]^2\rangle} - 1. \tag{4.9}$$

The non-Gaussian parameter $\gamma(t)$ for the different water regions is plotted in Fig. 4.13. For buried (R-1) and hydration (R-2) waters, $\gamma(t)$ has large positive values from 0.1 ps to 1 ns. At short (ballistic regime) and long (linear diffusion regime) times, $\gamma(t)$ is small for all the water layers due to the fact that in these two regimes the distributions of the atomic

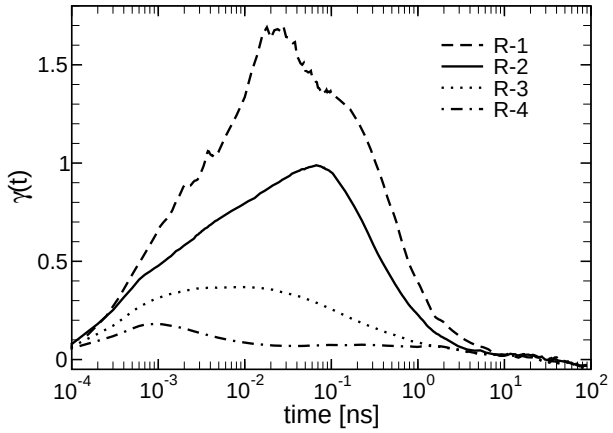

Figure 4.13: Time evolution of the non-gaussian (NG) parameter $\gamma(t)$ for oxygen atoms of the R-1, R-2, R-3 and R-4 waters.

displacements are Gaussian. $\gamma(t)$ is small for intermediate (R-3) waters for the entire time range and almost negligible for bulk waters.

$I_s(q,t)$ calculated from the MD trajectory of the R-1, R-2, R-3 and R-4 water oxygens can also be fitted with the KWW function, $A(q)\ \exp[-[t/\tau(q)]^{\beta(q)}]$. The q dependence of the exponent, $\beta(q)$ is shown in Fig. 4.14. Note that, the sub-(or super-) diffusive motion of waters affect the scattering if the probing q and t correspond to lengths and times characteristic to the sub-(or super-)diffusive regime of the water molecules. For R-1 and R-2 waters (Fig. 4.14, black dashed and continuous curves, respectively), $\beta(q) < 1$ for $q > 0.2$ Å^{-1} and $\beta(q) > 1$ for $q \leqslant 0.2$ Å^{-1}. This implies that, the water molecules in R-1 and R-2 regions show sub-diffusive motion for scattering vectors, $q > 0.2$ Å^{-1} and $I_s(q,t)$ can be approximated with a stretched exponential. Below q = 0.2 Å^{-1}, $\beta(q) > 1$ for R-1 and R-2 waters, and the corresponding IISFs can be fitted with a compressed exponential. For $q \to 0$, $\beta(q) \to 1$ for R-1 and R-2 waters, implying that at large lengths and times the R-1 and R-2 waters also undergo linear diffusive motion. $\beta(q) \cong 0.6$ for R-3 waters (Fig. 4.14, black dotted curve) until $q \geqslant 0.7$ Å^{-1} and then $\beta(q)$ increases to 1. Thus, R-3 waters exhibit sub-diffusion for large q values. For R-4 waters (black dot-dashed curve), $\beta(q) \geqslant 0.85$ for

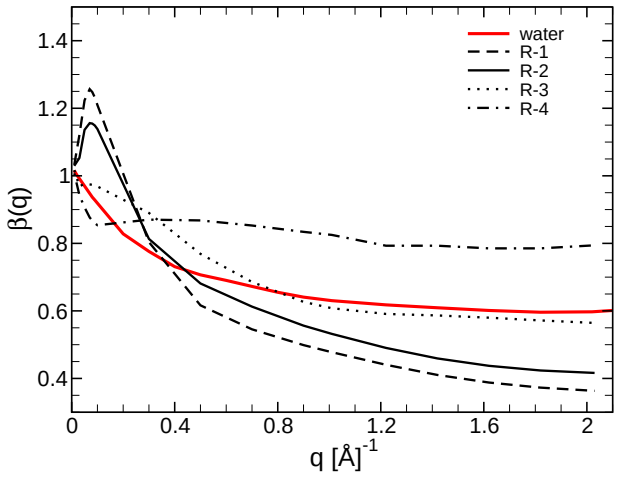

Figure 4.14: q dependence of the fitting parameter $\beta(q)$ used in the KWW approximation $A(q)\exp[-[t/\tau(q)]^{\beta(q)}]$ to the incoherent intermediate scattering function $I_s(q,t)$ for four different water layers, R-1, R-2, R-3 and R-4 and for whole water layer (labeled as water).

all q values, which means that the R-4 waters exhibit linear diffusive motion irrespective of the time and length scales at which the system is probed. $\beta(q)$ for all water oxygens (Fig. 4.14, red curve) is similar to that for the R-3 and R-4. This is due to the fact that the majority of waters are located in the R-3 and R-4 regions.

The peaks of $\alpha(t)$ (Fig. 4.7, bottom panel) for R-1 and R-2 waters appear around 0.1 ns, which correspond to $\langle[\delta r(t)]^2\rangle$ equal to 25 and 40 Å^2 for R-1 and R-2 regions. Using the Gaussian approximation, $I_s(q,t) = \exp\left(-q^2\frac{\langle[\delta r(t)]^2\rangle}{4}\right)$, one can estimate q at which super-diffusion occurs for R-1 and R-2 waters from the condition $I_s(q,t) = 1/e$. By replacing $\langle[\delta r(t)]^2\rangle$ with appropriate values in the Gaussian approximation, one obtains q = 0.4 and 0.3 Å^{-1} for R-1 and R-2 regions, respectively. These values are somewhat larger than the ones obtained above from $\beta(q)$. Also the $\beta(q)$ exponents for R-1 and R-2 are smaller (1.25 and 1.15, respectively) than the ones obtained for the corresponding $\alpha(t)$ values (1.5 and 1.3, respectively). Note that the first correction to the Gaussian approximation is related to the so called non-Gaussian (NG) parameter. Positive values of the NG parameter always makes the scattering function look less compressed. It turns out that for R-1 waters, the

non-Gaussian parameter is very large (Fig. 4.13) and it peaks around 0.02 ns. The NG parameter for R-2 is smaller and peaks around 0.1 ns.

4.9 Conclusions

The structural and dynamical properties of waters close to the membrane-water interface are different from that of bulk water. We have shown that a proper classification of waters as a function of their distance from the surface of the membrane needs to take into account the out-of-plane (z-axis fluctuations of the lipid molecules. By using the Voronoi tessellation method we have defined four dynamically connected water regions, i.e., buried (R-1), hydration (R-2), intermediate (R-3) and bulk (R-4) water regions. Due to their proximity to the polar lipid headgroups, R-1 and R-2 waters have qualitatively different dynamic properties from the R-3 and R-4 waters. These differences have been pointed out and quantified by investigating, through long-time all atom MD simulation, the time evolution of the lateral MSD of waters and the lifetime of the H-bonds between water and lipid molecules. We have also determined the contributions of the different waters to the incoherent intermediate scattering function and the corresponding dynamic structure factor measured in neutron scattering experiments. We have found that due to the small fraction of R-1 and R-2 waters the effects of their anomalous dynamics on the NS measurements are washed out by the contribution of the abundant ordinary R-4 bulk water.

References

[1] W. Humphrey, A. Dalke, and K. Schulten, *J. Mol. Graphics*, **14**, 33 (1996). VMD: Visual molecular dynamics.

[2] I. Kosztin, B. Barz, and L. Janosi, *J. Chem. Phys.*, **124**, 064106 (2006). Calculating potentials of mean force and diffusion coefficients from nonequilibrium processes without Jarzynski's equality.

[3] E. Flenner, J. Das, M. Rheinstädter, and I. Kosztin, *Phys. Rev. E*, **79**, 011907–1–011907–11 (2009). Subdiffusion and lateral diffusion coefficient of lipid atoms and molecules in phospholipid bilayers.

[4] M. Rheinstädter, J. Das, E. Flenner, B. Bruning, T. Seydel, and I. Kosztin, *Phys. Rev. Lett.*, **101**, 248106 (2008). Motional coherence in fluid phospholipid membranes.

[5] D. Fu, A. Libson, L. J. W. Miercke, C. Weitzman, P. Nollert, J. Krucinski, and R. M. Stroud, *Science*, **290**, 481–486 (2000). Structure of a glycerol conducting channel and the basis for its selectivity.

[6] M. Ø. Jensen, E. Tajkhorshid, and K. Schulten, *Structure*, **9**, 1083–1093 (2001). The mechanism of glycerol conduction in aquaglyceroporins.

[7] M. Ø. Jensen, S. Park, E. Tajkhorshid, and K. Schulten, *Proc. Nat. Acad. Sci. USA*, **99**, 6731–6736 (2002). Energetics of glycerol conduction through aquaglyceroporin GlpF.

[8] K. B. Heller, E. C. Lin, and T. H. Wilson, *J. Bacteriol.*, **144**, 274–278 (1980). Substrate specificity and transport properties of the glycerol facilitator of escherichia-coli.

[9] M. J. Borgnia and P. Agre, *Proc. Nat. Acad. Sci. USA*, **98**, 2888–2893 (2001). Reconstitution and functional comparison of purified GlpF and AqpZ, the glycerol and water channels from escherichiacoli.

[10] M. Borgnia, S. Nielsen, A. Engel, and P. Agre, *Ann. Rev. Biochem.*, **68**, 425–458 (1999). Cellular and molecular biology of the aquaporin water channels.

[11] E. Tajkhorshid, P. Nollert, M. Ø. Jensen, L. J. W. Miercke, J. O'Connell, R. M. Stroud, and K. Schulten, *Science*, **296**, 525–530 (2002). Control of the selectivity of the aquaporin water channel family by global orientational tuning.

[12] B. L. de Groot and H. Grubmüller, *Curr. Op. Struct. Biol.*, **15**(2), 176–183 (2005). The dynamics and energetics of water permeation and proton exclusion in aquaporins.

[13] A. R. Leach, *Molecular Modelling: Principles and Applications (2nd edition)*, Prentice Hall, Upper Saddle River, New Jersey, 2001.

[14] D. Frenkel and B. Smit, *Understanding Molecular Simulation From Algorithms to Applications*, Academic Press, California, 2002.

[15] M. P. Allen and D. J. Tildesley, *Computer simulation of liquids*, Oxford University Press, Oxford, New York, 1987.

[16] B. Roux, *Comput. Phys. Commun.*, **91**(1-3), 275–282 (1995). The calculation of the potential of mean force using computer-simulations.

[17] Torrie and Valleau, *J. Comput. Chem.*, **23**, 187–199 (1977). Nonphysical sampling distributions in monte carlo free-energy estimation: Umbrella sampling.

[18] B. Isralewitz, J. Baudry, J. Gullingsrud, D. Kosztin, and K. Schulten, *J. Mol. Graphics Modell.*, **19**(1), 13–25 (2001). Steered molecular dynamics investigations of protein function.

[19] M. W. Forney, L. Janosi, and I. Kosztin, *Physical Review E - Statistical, Nonlinear, and Soft Matter Physics*, **78**(5) (2008). Calculating free-energy profiles in biomolecular systems from fast nonequilibrium processes.

[20] S. Park and K. Schulten, *J. Chem. Phys.*, **120**(13), 5946–5961 (2004). Calculating potentials of mean force from steered molecular dynamics simulations.

[21] J. Phillips, R. Braun, W. Wang, J. Gumbart, E. Tajkhorshid, E. Villa, C. Chipot, R. Skeel, L. Kale, and K. Schulten, *J. Comput. Chem*, **26**, 1781 (2005). Scalable molecular dynamics with NAMD.

[22] A. MacKerell, D. Bashford, M. Bellott, R. Dunbrack, J. Evanseck, M. Field, S. Fischer, J. Gao, H. Guo, S. Ha, D. Joseph-McCarthy, L. Kuchnir, K. Kuczera, F. Lau, C. Mattos, S. Michnick, T. Ngo, D. Nguyen, Prodhom, W. Reiher, B. Roux, M. Schlenkrich, J. Smith, J. Stote, J. Straub, M. Watanabe, J. Wiorkiewicz-Kuczera, D. Yin, and M. Karplus, *J. Chem. Phys. B*, **102**, 3586–3616 (1998). All-atom empirical potential for molecular modeling and dynamics studies of proteins.

[23] S. Feller and J. MacKerell, *J. Phys. Chem. B*, **104**, 7510 (2000). An improved emperical potential energy function for molecular simulations of phospholipids.

[24] W. Jorgensen, J. Chandrasekhar, J. Madura, R. Impey, and M. Klein, *J. Chem. Phys.*, **79**, 926 (1983). Comparison of simple potential functions for simulating liquid water.

[25] T. Darden, D. York, and L. Pedersen, *Journal of Chemical Physics*, **98**, 10089–10092 (1993). Particle mesh ewald - an n.log(n) method for ewald sums in large systems.

[26] S. Feller, Y. Zhang, R. W. Pastor, and B. R. Brooks, *J. Chem. Phys.*, **103**, 4613–4621 (2000). Constant pressure molecular dynamics simulation: The langevin piston method.

[27] S. Miyamoto and P. A. Kollman, *Journal of Computational Chemistry*, Oct (1992). Settle - an analytical version of the shake and rattle algorithm for rigid water models.

[28] M. Ø. Jensen, E. Tajkhorshid, and K. Schulten, *Biophys. J.*, **85**(5), 2884–2899 (2003). Electrostatic tuning of permeation and selectivity in aquaporin water channels.

[29] R. Zwanzig, *Nonequilibrium statistical mechanics*, Oxford University Press, Oxford ; New York, 2001.

[30] C. Gardiner, *Handbook of Stochastic Methods: for Physics, Chemistry and the Natural Sciences (3rd edition)*, Springer-Verlag, New York, 2004.

[31] M. Ø. Jensen and O. G. Mouritsen, *Biophys. J.*, **90**(7), 2270–2284 (2006). Single-channel water permeabilities of Escherichia coli aquaporins AqpZ and GlpF.

[32] L. Deyu, P. Grayson, and K. Schulten, *Biophys. J.*, **85**, 2977–2987 (2003). Glycerol conductance and physical assymetry of the escherichia coli glycerol facilitator glpf.

[33] P. Vidossich, M. Cascella, and P. Carloni, *Proteins-Structure Function and Bioinformatics*, **55**(4), 924–931 (2004). Dynamics and energetics of water permeation through the aquaporin channel.

[34] M. W. Mahoney and W. L. Jorgensen, *J. Chem. Phys.*, **114**, 363–366 (2000). Diffusion constant of the tip5p model of liquid water.

[35] P. Pohl, S. M. Saparov, M. J. Borgnia, and P. Agre, *Proc. Nat. Acad. Sci. USA*, **98**(17), 9624–9629 (2001). Highly selective water channel activity measured by voltage clamp: Analysis of planar lipid bilayers reconstituted with purified aqpz.

[36] S. M. Saparov, S. P. Tsunoda, and P. Pohl, *Biology of the Cell*, **97**(7), 545–550 (2005). Proton exclusion by an aquaglyceroprotein: A voltage clamp study.

[37] M. J. Borgnia, D. Kozono, G. Calamita, P. C. Maloney, and P. Agre, *J. Mol. Biol.*, **291**(5), 1169–1179 (1999). Functional reconstitution and characterization of AqpZ, the E-coli water channel protein.

[38] T. Walz, B. L. Smith, M. L. Zeidel, A. Engel, and P. Agre, *J. Biol. Chem.*, **269**, 1583–1586 (1994). Biologically active two-dimensional crystals of aquaporin chip.

[39] M. L. Zeidel, S. Nielsen, B. L. Smith, S. V. Ambudkar, A. B. Maunsbach, and P. Agre, *Biochemistry*, **33**, 1606–1615 (1994). Ultrastructure, pharmacological inhibition, and transport selectivity of aquaporin channel-forming integral protein in proteoliposomes.

[40] I. Kosztin and K. Schulten, *Phys. Rev. Lett.*, **93**(23), 238102 (2004). Fluctuation-driven molecular transport through an asymmetric membrane channel.

[41] F. Zhu, E. Tajkhorshid, and K. Schulten, *Biophys. J.*, **83**, 154–160 (2002). Pressure induced water transport in membrane channels studied by molecular dynamics.

[42] B. Alberts, D. Bray, J. Lewis, M. Raff, K. Roberts, and J. D. Watson, *Molecular biology of the cell 2nd edition*, Garland Publishing Inc., New York and London, 1989.

[43] R. Lipowsky and E. Sackmann, Eds., *Structure and Dynamics of Membranes*, Vol. 1 of *Handbook of Biological Physics*, Elsevier, Amsterdam, 1995.

[44] S. König, E. Sackmann, D. Richter, R. Zorn, C. Carlile, and T. Bayerl, *J. Chem. Phys.*, **100**, 3307–3316 (1994). Molecular dynamics of water in oriented DPPC multilayers studied by quasielastic neutron scattering and deuterium-nuclear magnetic resonance relaxation.

[45] S. König, W. Pfeiffer, T. Bayerl, D. Richter, and E. Sackmann, *J. Phys. II France*, **2**, 1589 (1992). Molecular dynamics of lipid bilayers studied by incoherent quasi-elastic neutron scattering.

[46] S. König, T. Bayerl, G. Coddens, D. Richter, and E. Sackmann, *Biophys. J.*, **68**, 1871 (1995). Hydration dependence of chain dynamics and local diffusion in l-a-dipalmitoylphosphtidylcholine multilayers studied by incoherent quasi-elastic neutron scattering.

[47] W.Pfeiffer, T. Henkel, E. Sackmann, and W. Knorr, *Europhys. Lett.*, **8**, 201 (1989). Local dynamics of lipid bilayers studied by incoherent quasi-elastic neutron scattering.

[48] W. Pfeiffer, S. König, J. Legrand, T. Bayerl, D. Richter, and E. Sackmann, *Europhys. Lett.*, **23**, 457–462 (1993). Neutron spin echo study of membrane undulations in lipid multibilayers.

[49] T. Bayerl, *Curr. Opin. Colloid Interface Sci.*, **5**, 232–236 (2000). Collective membrane motions.

[50] E. Lindahl and O. Edholm, *Biophys. J.*, **79**, 426–433 (2000). Mesoscopic undulations and thickness fluctuations in lipid bilayers from molecular dynamics simulations.

[51] T. Salditt, *Curr. Opin. Colloid Interface Sci.*, **5**, 19–26 (2000). Structure and fluctuations of highly oriented phospholipid membranes.

[52] W. Pfeiffer, G. Sclossbauer, W. Knoll, B. Farago, A. Steyer, and E. Sackmann, *J. Phys. (France)*, **49**, 1077 (1988). Ultracold neutron scattering study of local lipid mobility in bilayer membranes.

[53] J. Tabony and B. Perly, *Biochim. Biophys. Acta*, **1063**, 67 (1990). Quasielastic neutron scattering measurements of fast local translational diffusion of lipid molecules in phospholipid bilayers.

[54] W. Vaz, R. Clegg, and D. Hallmann, *Biochemistry*, **24**, 781 (1985). Translational diffusion of lipids in liquid crystalline phase phosphatidylcholine multilayers. a comparison experiment with theory.

[55] H. Wennerstrom and G. Lindblom, *Quart. Rev. Biophys.*, **10**, 67 (1977). Bilogical and model membranes studied by nuclear magnetic resonance of spin one-half nuclei.

[56] A. Kuo and C. Wade, *Biochemistry*, **18**, 2300 (1979). Lipid lateral diffusion by pulsed nuclear magnetic resonance.

[57] Y. Shin, U. Ewert, D. Budil, and J. Freed, *Biophys. J.*, **59**, 950 (1991). Microscopic versus macroscopic diffusion in model membranes by electron spin resonance spectral-spatial imaging.

[58] E. Falck, T. Rog, M. Karttunen, and I. Vattulainen, *J. Am. Chem. Soc.*, **130**, 44–45 (2008). Lateral diffusion in lipid membranes through collective flows.

[59] J. Wohlert and O. Edholm, *J. Chem. Phys.*, **125**, 204703 (2006). Dynamics in atomistic simulations of phospholipid membranes: Nuclear magnetic resonance relaxation rates and lateral diffusion.

[60] M. Doxastakis, V. Garcia Sakai, S. Ohtake, J. Maranas, and J. de Pablo, *Biophysical Journal*, **92**, 147 (2007). A molecular view of melting in anhydrous phospholipidic membranes.

[61] E. Lindahl and O. Edholm, *J. Chem. Phys.*, **115**, 4938 (2001). Molecular dynamics simulation of nmr relaxation rates and slow dynamics in lipid bilayers.

[62] C. Anezo, H. de Vries, H.-D. Holtje, D. Tieleman, and S.-J. Marrink, *J. Phys. Chem. B*, **107**, 9424 (2004). Methodological issues in lipid bilayer simulations.

[63] M. Patra, M. Karttunen, M. Hyvonen, and I. Vattulainen, *J. Phys. Chem. B*, **108**, 4485 (2004). Lipid bilayers driven to a wrong lane in molecular dynamics simulations by subtle changes in longe-range electrostatic interactions.

[64] J. Klauda, B. Brooks, and R. Pastor, *J. Chem. Phys.*, **125**, 144710 (2006). Dynamical motions of lipids and a finite size effect in simulations of bilayers.

[65] C. Hofsäß, E. Lindahl, and O. Edholm, *Biophys. J.*, **84**, 2192 (2003). Molecular dynamics simulations of phospholipid bilayers with cholesterol.

[66] E. Falck, M. Patra, M. Karttunen, M. Hyvonen, and I. Vattulainen, *Biophys. J.*, **87**, 1076 (2004). Lessons of slicing membranes: Interplay of packing, free area, and lateral diffusion in phospholipid/cholesteral bilayers.

[67] P. F. F. Almeida and V. W. L. C., *Handbook of Biological Physics*, Elsevier Science, New York, 1995.

[68] G. Strobl, *The Physics of Polymers*, Springer-Verlag, Berlin, 2007.

[69] S. Chong and M. Fuchs, *Phys. Rev. Lett.*, **88**, 185702 (2002). Mode-coupling theory for structural and conformational dynamics of polymer melts.

[70] S. Chong, M. Aichele, H. Meyer, M. Fuchs, and J. Baschnagel, *Phys. Rev. E*, **76**, 051806 (2007). Structural and conformational dynamics of supercooled polymer melts: Insights from first-principles theory and simulations.

[71] M. C. Rheinstädter, T. Seydel, W. Häußler, and T. Salditt, *J. Vac. Sci. Technol. A*, **24**, 1191–1196 (2006). Exploring the collective dynamics of lipid membranes with inelastic neutron scattering.

[72] J. S. Hub, T. Salditt, M. C. Rheinstädter, and B. L. de Groot, *Biophysical J.*, **93**, 3156–3168 (2007). Short range order and collective dynamics of dmpc bilayers. acomparison between molecular dynamics simulations, x-ray, and neutron scattering experiments.

[73] M. Tarek, D. Tobias, S.-H. Chen, and M. Klein, *Phys. Rev. Lett.*, **87**, 238101 (4 pages) (2001). Short wavelength collective dynamics in phospholipid bilayers: A molecular dynamics study.

[74] S. Paula, A. Volkov, A. Van Hoek, T. Haines, and D. Deamer, *Biophys. J.*, **70**, 339–348 (1996). Permeation of protons, potassium ions, and small polar molecules through phospholipid bilayers as a function of membrane thickness.

[75] A. A. Gurtovenko, M. Patra, M. Karttunen, and I. Vattulainen, *Biophys J*, **86**, 3461 (2004). Cationic dmpc/dmtap lipid bilayers: Molecular dynamics study.

[76] U. Essmann, L. Perera, M. L. Berkowitz, T. Darden, H. Lee, and L. G. Pedersen, *J. Chem. Phys.*, **103**, 8577–8593 (1995). A smooth particle mesh Ewald method.

[77] M. Tarek, D. Tobias, S.-H. Chen, and M. Klein, *Phys. Rev. Lett.*, **87**, 238101 (4 pages) (2001). Short wavelength collective dynamics in phospholipid bilayers: A molecular dynamics study.

[78] J. Hansen and I. McDonald, *Theory of Simple Liquids*, Elsevier, 2006.

[79] M. C. Rheinstädter, C. Ollinger, G. Fragneto, F. Demmel, and T. Salditt, *Phys. Rev. Lett.*, **93**, 108107 (4 pages) (2004). Collective dynamics of lipid membranes studied by inelastic neutron scattering.

[80] M. C. Rheinstädter, W. Häussler, and T. Salditt, *Phys. Rev. Lett.*, **97**, 048103 (4 pages) (2006). Dispersion relation of lipid membrane shape fluctuations by neutron spin-echo spectrometry.

[81] S. Lovesey, *Theory of Neutron Scattering from Condensed Matter*, Clarendon Press, Oxford, 1984.

[82] J. A. Nelder and R. Mead, *Computer J.*, **7**, 308–313 (1965). A simplex method for function minimization.

[83] W. H. Press, S. A. Teukolsky, W. T. Vetterling, and B. P. Flannery, *Numerical recipes The art of scientific computing (3rd edition)*, Cambridge University Press, New York, 2007.

[84] P. DeGennes, *Physica (Amsterdam)*, **25**, 825–839 (1959). Liquid dynamics and inelastic scattering of neutrons.

[85] C. Bennemann, C. Donati, J. Baschnagel, and S. C. Glotzer, *Nature*, **399**, 246–249 (1999). Growing range of correlated motion in a polymer melt on cooling towards the glasstransition.

[86] J. Fitter, *Journal of Physical Chemistry B*, **103**(38), 8036–8050 (1999). Interactions of hydration water and biological membranes studied by neutron scattering.

[87] M. L. Berkowitz, D. Bostick, and S. A. Pandit, *Chem. Review*, **106**, 1527–1539 (2006). Aqueous solution next to phospholipid membrane surfaces: insights from simulations.

[88] K. Aman, E. Lindahl, O. Edholm, P. H. kansson, and P.-O. Westlund, *Biophys. Jour.*, **84**, 102–115 (2003). Structure and dynamics of interfacial water in an la phase lipid bilayer from molecular dynamics simulations.

[89] N. Markova, E. Sparr, L. Wads, and H. Wennerstrm, *Journal of Physical Chemistry B*, **104** (2000). A calorimetric study of phospholipid hydration. simultaneous monitoring of enthalpy and free energy.

[90] S. A. Pandit, D. Bostick, and M. L. Berkowitz, *Jour. Chem. Phys.*, **119**, 2199–2205 (2003). An algorithm to describe molecular scale rugged surfaces and its application to the study of a water/lipid interface.

[91] J. F. Nagle and S. Tristram-Nagle, *Biochimica et Biophysica Acta - Reviews on Biomembranes*, **1469**(3), 159–195 (2000). Structure of lipid bilayers.

[92] B. Halle, J. R. Helliwell, A. Kornyshev, and J. B. F. N. Engberts, *Philosophical Transactions of the Royal Society B: Biological Sciences*, **359**(1448), 1207–1224 (2004). Protein hydration dynamics in solution: A critical survey.

[93] G. Otting, *Progress in Nuclear Magnetic Resonance Spectroscopy*, **31**(2-3), 259–285 (1997). NMR studies of water bound to biological molecules.

[94] J. M. Zanotti, M. C. Bellissent-Funel, and J. Parello, *Biophysical Journal*, **76**(5), 2390–2411 (1999). Hydration-coupled dynamics in proteins studied by neutron scattering and nmr: The case of the typical ef-hand calcium-binding parvalbumin.

[95] P. O. Westlund, *Journal of Physical Chemistry B*, **104**(25), 6059–6064 (2000). Line shape analysis of NMR powder spectra of ^2H_2O in lipid bilayer systems.

[96] S. K. Pal, D. Sukul, D. Mandal, and K. Bhattacharyya, *Journal of Physical Chemistry B*, **104**(18), 4529–4531 (2000). Solvation dynamics of dcm in lipid.

[97] S. K. Pal and A. H. Zewail, *Chemical Reviews*, **104**(4), 2099–2123 (2004). Dynamics of water in biological recognition.

[98] J. Skora, P. Kapusta, V. Fidler, and M. Hof, *Langmuir*, **18**(3), 571–574 (2002). On what time scale does solvent relaxation in phospholipid bilayers happen?

[99] D. Russo, R. K. Murarka, G. Hura, E. Verschell, J. R. D. Copley, and T. Head-Gordon, *Journal of Physical Chemistry B*, **108**(51), 19885–19893 (2004). Evidence for anomalous hydration dynamics near a model hydrophobic peptide.

[100] M. R. Harpham, B. M. Ladanyi, N. E. Levinger, and K. W. Herwig, *Journal of Chemical Physics*, **121**(16), 7855–7868 (2004). Water motion in reverse micelles studied by quasielastic neutron scattering and molecular dynamics simulations.

[101] W. Zhao, D. E. Moilanen, E. E. Fenn, and M. D. Fayer, *Journal of the American Chemical Society*, **130**(42), 13927–13937 (2008). Water at the surfaces of aligned phospholipid multibilayer model membranes probed with ultrafast vibrational spectroscopy.

[102] J. Faeder and B. M. Ladanyi, *Journal of Physical Chemistry B*, **104**(5), 1033–1046 (2000). Molecular dynamics simulations of the interior of aqueous reverse micelles.

[103] J. Faeder and B. M. Ladanyi, *Journal of Physical Chemistry B*, **105**(45), 11148–11158 (2001). Solvation dynamics in aqueous reverse micelles: A computer simulation study.

[104] S. Y. Bhide and M. L. Berkowitz, *The Journal of chemical physics*, **123**(22), 224702 (2005). Structure and dynamics of water at the interface with phospholipid bilayers.

[105] S. Y. Bhide and M. L. Berkowitz, *Journal of Chemical Physics*, **125**(9), 094713–1–0947–7 (2006). The behavior of reorientational correlation functions of water at the water-lipid bilayer interface.

[106] S. Balasubramanian and B. Bagchi, *Journal of Physical Chemistry B*, **105**(50), 12529–12533 (2001). Slow solvation dynamics near an aqueous micellar surface.

[107] S. Balasubramanian and B. Bagchi, *Journal of Physical Chemistry B*, **106**(14), 3668–3672 (2002). Slow orientational dynamics of water molecules at a micellar surface.

[108] S. Balasubramanian, S. Pal, and B. Bagchi, *Current Science*, **82**(7), 845–854 (2002). Dynamics of water molecules at the surface of an aqueous micelle: Atomistic molecular dynamics simulation study of a complex system.

[109] L. R. Pratt and A. Pohorille, *Chemical Reviews*, **102**(8), 2671–2692 (2002). Hydrophobic effects and modeling of biophysical aqueous solution interfaces.

[110] S. J. Marrink, D. P. Tieleman, A. R. Van Buuren, and H. J. C. Berendsen, *Faraday Discussions*, **103**, 191–201 (1996). Membranes and water: An interesting relationship.

[111] F. Zhou and K. Schulten, *Journal of Physical Chemistry*, **99**(7), 2194–2207 (1995). Molecular dynamics study of a membrane - water interface.

[112] M. de Berg, M. v. K. O. Schwarzkopf, and M. Overmars, *Computational Geometry: Algorithms and Applications, 2nd Rev. Ed.*, Springer-Verlag, Berlin, 2000.

[113] P. Jedlovszky and M. Mezei, *Journal of Physical Chemistry B*, **105**(17), 3614–3623 (2001). Orientational order of the water molecules across a fully hydrated dmpc bilayer: A monte carlo simulation study.

[114] S. Chen, *Hydrogen-Bonded Liquids:Quasi-elastic and inelastic neutron scattering and molecular dynamics of water at supercooled temperature*, Kluwer Academic Publishers in cooperation with NATO Scientific Affairs Division, Boston, 1991.

[115] S. D. Napoli and Z. Gamba, *Journal of Chemical Physics*, **132**, 075101–1–075101–7 (2010). Correlated dynamics of water and amphiphilic molecules in thin newton black films.

[116] K. Raghavan, M. R. Reddy, and M. L. Berkowitz, *Langmuir*, **8**, 233–240 (1992). A molecular dynamics study of the structure and dynamics of water between dilauroylphosphatidylethanolamine bilayers.

[117] M. P.-G. andYuji Takaoka, H. Miyagawa, K. Kitamura, and A. Kusumi, *Biophys. J.*, **76**, 12281240 (1999). Charge pairing of headgroups in phosphatidylcholine membranes: A molecular dynamics simulation study.

[118] C. F. Lopez, . S. O. Nielsen, M. L. Klein, and P. B. Moore, *J. Phys. Chem. B*, **108**, 6603 (2004). Hydrogen bonding structure and dynamics of water at the dimyristoylphosphatidylcholine lipid bilayer surface from a molecular dynamics simulation.

[119] A. Luzar and D. Chandler, *Phys. Rev. Letters*, **76**, 928–931 (1996). Effect of environment on hydrogen bond dynamics in liquid water.

Vita

Jhuma Das was born on September 12, 1980 in Kolkata, India. She graduated from the Physics Department of Lady Brabourne College, Calcutta University, in Kolkata, India, in July 2001. She earned her Masters Degree in Physics from the University of Pune in July 2003. She joined Dr. Dhananjay Bhattacharyya's group in September 2003 as a project assistant and worked there for one and a half years. Then she joined Dr. Ioan Kosztin's group in August 2005 to pursue her doctoral studies and received her Ph.D. degree in Physics from the University of Missouri in August, 2010. She recently accepted a postdoctoral position at University of North Carolina-Chapel Hill with Dr. Max Berkowitz, starting September 2010.